Dynamics of Ices and Fluids on Mars and Kuiper Belt Objects

by

Christopher P. Mount

A Dissertation Presented in Partial Fulfillment
of the Requirements for the Degree
Doctor of Philosophy

Approved April 2019 by the
Graduate Supervisory Committee:

Philip R. Christensen, Chair
Steven J. Desch
James F. Bell, III
Amanda B. Clarke
Kelin X. Whipple

ARIZONA STATE UNIVERSITY

May 2019

ABSTRACT

The seasonal deposition of CO_2 on the polar caps is one of the most dynamic processes on Mars and is a dominant driver of the global climate. Remote sensing temperature and albedo data were used to estimate the subliming mass of CO_2 ice on south polar gullies near Sisyphi Cavi. Results showed that column mass abundances range from 400 - 1000 $kg·m^2$ in an area less than 60 km^2 in late winter. Complete sublimation of the seasonal caps may occur later than estimated by large-scale studies and is geographically dependent. Seasonal ice depth estimates suggested variations of up to 1.5 m in depth or 75% in porosity at any one time. Interannual variations in these data appeared to correlate with dust activity in the southern hemisphere. Correlation coefficients were used to investigate the relationship between frost-free surface properties and the evolution of the seasonal ice in this region. Ice on high thermal inertia units was found to disappear before any other ice, likely caused by inhibited deposition during fall. Seasonal ice springtime albedo appeared to be predominantly controlled by orientation, with north-facing slopes undergoing brightening initially in spring, then subliming before south-facing slopes. Overall, the state of seasonal ice is far more complex than globally and regionally averaged studies can identify.

The discovery of cryovolcanic features on Charon and the presence of ammonia hydrates on the surfaces of other medium-sized Kuiper Belt Objects suggests that cryovolcanism may be important to their evolution. A two-dimensional, center-point finite difference, thermal hydraulic model was developed to explore the behavior of cryovolcanic conduits on midsized KBOs. Conduits on a Charon-surrogate were shown to maintain flow through over 200 km of crust and mantle down to radii of $R = 0.20$ m. Radii higher than this became turbulent due to high viscous dissipation and low thermal conductivity. This model was adapted to explore the emplacement

of Kubrik Mons. Steady state flow was achieved with a conduit of radius $R = 0.02$ m for a source chamber at 2.3 km depth. Effusion rates computed from this estimated a 122 - 163 Myr upper limit formation timescale.

To my amazing wife, whose patience and encouragement saw me through.

ACKNOWLEDGMENTS

TABLE OF CONTENTS

LIST OF TABLES

LIST OF FIGURES

Chapter 1

BACKGROUND

Ice inventories on planetary bodies can grant insight into the formation of our solar system and the potential for life therein. Terrestrial and icy bodies offer a plethora of ice varieties to study that have wide implications to these ends. Of particular interest is our nearest terrestrial neighbor, Mars, as well as what are thought to be the most primitive (i.e., oldest) bodies in our solar system: the Kuiper Belt Objects (KBOs). Due to the nature of ices on these bodies, steady-state or static investigations are often insufficient to fully characterize ice systems. It is therefore of utmost importance that the dynamics of these systems be studied in greater detail.

Mars' surface temperatures vary seasonally, allowing CO_2 and H_2O ices to condense and sublime onto the surface near the poles, forming seasonal polar caps. KBOs have a rich diversity of sizes, semi-major axes, and surface temperatures that allow for a wide range of ice species on their surfaces. Water is chief among these species, with potential for internal liquid water on many of these bodies. With the presence of freezing depressants, liquid water could persist at temperatures lower than freezing and may even extrude on to the surface of some KBOs.

These dynamic processes will be the focus of the work, herein.

1.1 Martian Polar Caps

1.1.1 Seasonal CO_2 Cycle

The seasonal advance and retreat of the polar caps on Mars has been well documented since the 18th century (Herschel, 1784). During each poles respective winter, solar illumination ceases as Polar Night begins. During this time, surface temperatures fall to the freezing point of CO_2 - about 150 K (James *et al.*, 1992) at average Martian atmospheric pressure. This causes the primarily CO_2 atmosphere ($\approx$95% by volume) to deposit onto the surface as ice (Leighton and Murray, 1966; Neugebauer *et al.*, 1971). Sublimation of this ice commences the following spring when sunlight returns to the pole. The vapor is then transported across the equator as condensation begins on the opposite pole. Approximately 25% of the atmosphere undergoes this process annually (Tillman *et al.*, 1993; Kelly *et al.*, 2006). Because the global climate and atmospheric circulation depend on the CO_2 cycle, active CO_2 processes must be examined to understand the climate history of Mars.

The northern seasonal cap grows during northern fall, from $L_s \approx 180°$ to $270°$ (Kieffer and Titus, 2001; Piqueux *et al.*, 2015). The cap edge advances to $\approx 50°$N latitude, reaching maximum extent just after the autumnal equinox ($L_s = 270°$). The southern seasonal cap is deposited from $L_s \approx 330°$ to $90°$, which is southern fall (Kieffer *et al.*, 2000; Piqueux *et al.*, 2015). The southern cap is larger than the north, extending to approximately 45°S. This is because southern winter is longer and the southern hemisphere is higher in elevation, which reduces surface pressure and allows for more condensation during fall (Pollack *et al.*, 1990; James *et al.*, 1992).

Deposition of seasonal ice is thought to occur in two modes: direct surface de-

position and atmospheric deposition and fallout. Direct deposition is caused by radiative cooling of the surface, resulting in the formation of dense, coarse-grained "slab" ice (Kieffer *et al.*, 2000). Atmospheric deposition occurs when CO_2 nucleates on water ice or dust particles above the surface and precipitates out of the atmosphere (Hayne *et al.*, 2012, 2014; Titus *et al.*, 2001). This CO_2 snow produces porous, fine-grained surface ice deposits. Grain size derived from spectra suggest that the primary depositional mode on the caps is likely slab (Kieffer *et al.*, 2000; Kieffer and Titus, 2001; Titus *et al.*, 2001), though snow could account for up to 20% of seasonal deposits by mass, especially in the north (Hayne *et al.*, 2014).

Slab ice tends to have low albedo in the visible wavelengths owing to the long path lengths (coarse-grains) produced by direct deposition (Kieffer *et al.*, 2000). Conversely, snow has high albedo (Warren *et al.*, 1990) due to the short path lengths (fine-grains) (Kieffer *et al.*, 2000). The contamination from water ice and dust have dramatic effects on the albedo in the visible (Warren *et al.*, 1990), because the absorption coefficients for CO_2 ice are low (Hansen, 2005). Only 1% dust contamination, 10% H_2O contamination, or a 100 μm monolayer of water frost covering a deposit is enough to spectrally obscure CO_2 (Hansen, 1999; Kieffer *et al.*, 2000; Warren *et al.*, 1990).

Recession of the northern seasonal cap is essentially zonally symmetric, receding from $L_s \approx 270°$ to $90°$ (summer solstice) (James *et al.*, 1992; Kieffer and Titus, 2001; Calvin *et al.*, 2015; Piqueux *et al.*, 2015). The southern seasonal cap recesses during $L_s \approx 90 - 315°$. The recession of the south cap is typically non-symmetric, with the seasonal ice from 60 - 210°E longitude receding rapidly and the seasonal ice between 30 and 240°E receding slowly (James *et al.*, 1992; Kieffer *et al.*, 2000; Calvin *et al.*, 2017; Piqueux *et al.*, 2015). Interannual variability is typically limited, though regional and

3

local variations in the cap edge occur (Benson and James, 2005; Calvin *et al.*, 2015, 2017; Piqueux *et al.*, 2015).

The northern cap is unique in that it is contaminated with water ice throughout the entirety of the cycle (Brown *et al.*, 2012). Due to the high percentage of water (up to , the retreat of the northern cap is marked by a water ice annulus that follows the cap edge (Wagstaff *et al.*, 2008) likely caused by cold trapping of subliming water vapor back onto the retreating seasonal cap. H_2O grain sizes in these deposits grow during the northern recession (Brown *et al.*, 2012).

This behavior is in stark contrast to the southern cap. There is almost no water ice present on the southern cap until after $L_s \approx 200°$, and this water ice is short-lived (Brown *et al.*, 2010; Langevin *et al.*, 2007). Unlike H_2O grain size in the north, CO_2 ice grain size decreases over spring (Brown *et al.*, 2010). During retreat the southern cap develops two large-scale albedo anomalies: the Cryptic region and the Bright region between $L_s \approx 200$ and $240°$ (Kieffer *et al.*, 2000). The Cryptic region is characterized by low albedo and low temperature, suggesting translucent slab CO_2 or a dust-doped CO_2. The presence of dust fans and the absence of CO_2 spectral signatures (Brown *et al.*, 2010; Langevin *et al.*, 2007) suggest a moderate percentage of dust contamination. The Bright region appears to be large-grained CO_2 ice, but it is unclear what sets it apart from other ice on the cap. Colaprete *et al.* (2005) showed that a standing wave in the atmosphere is generated from the Hellas basin topography that could create two micro-climates on the south pole. The micro-climate associated with the Bright region tends to be cloudier and might promote more snowfall, while that associated with the Cryptic region is warmer, prohibiting snowfall and increasing radiative losses to space (Colaprete *et al.*, 2005). However, this would lead to dramatic albedo contrasts in these regions from the beginning of sublimation, so why these

anomalies do not appear until mid-spring is still unclear. The answer may lie in processes that modify the properties of ice during sublimation and/or the terrain the ice is deposited on.

The evolution of ice during sublimation is dependent on the depositional state. Snow is believed to undergo densification due to self-compaction and settling (Aharonson *et al.*, 2004). Snow and porous slab deposits may anneal into high density slab over spring due to vapor diffusion processes (Eluszkiewicz, 1991, 1993; Eluszkiewicz *et al.*, 2005). This process occurs when ice grains diffuse, evaporate, and re-condense across grain boundaries to form slabs containing quasi-spherical pores. This process facilitates grain-growth and pore annihilation, reducing the albedo and increasing the density of the ice (Eluszkiewicz *et al.*, 2005). Solid-state greenhouse effects may occur that fracture slab deposits (Kieffer *et al.*, 2006; Kieffer, 2007; Portyankina *et al.*, 2010, 2012), which both increases the albedo and reduces the density of the ice. Slab with high dust content may be self-cleaning during spring (Kieffer *et al.*, 2006; Kieffer, 2007), drastically altering the albedo and transparency of the ice. The precise temporal evolution of the state of seasonal deposits remains still largely unknown.

Dust storms appear to have little effect on the seasonal southern cap, because they tend to initiate late in the southern cap retreat (Piqueux *et al.*, 2015). However, local and regional variations in the retreat of the cap may occur due to modification of atmospheric opacity and thermal downwelling radiation by the presence of dust in the atmosphere (Bonev *et al.*, 2002, 2008).

1.1.2 Column Mass Abundance

Local variations in the physical states of seasonal CO_2 ice grains (e.g., fine/coarse grained, porosity) may significantly impact the polar energy balance (Pollack *et al.*, 1990, 1993), and therefore the recession rates. This is because the state and compositional-mix of the ice determines the surface emissivity and albedo, which control the radiated and absorbed fluxes, respectively. These fluxes contribute to the cycling of CO_2, along with the latent heat of fusion.

The energy input from the latent heat of fusion depends on the mass of condensed CO_2. The distribution of mass yields insight into surface-atmosphere interactions that help drive the global climate. The mass of CO_2 on the surface places constraints on the depth and/or density of seasonal deposits and has important implications for depositional mechanisms, microphysical states, and time evolution of seasonal deposits. The mass per unit area of seasonal ice is sometimes referred to as column density, column abundance, or thickness. I adopt the convention of Mount and Titus (2015) and call this Column Mass Abundance (CMA) to keep a clear distinction from bulk density and the seasonal depth of the ice cap.

CMA has been derived in a variety of ways: energy balance calculations (Kieffer *et al.*, 2000; Kieffer and Titus, 2001), neutron spectroscopy (Feldman *et al.*, 2003; Aharonson *et al.*, 2004; Prettyman *et al.*, 2009; Litvak *et al.*, 2007), gamma ray spectroscopy (Feldman *et al.*, 2003; Kelly *et al.*, 2006), and variations in the gravity field as measured by an orbiting spacecraft (Smith *et al.*, 2001b). These studies have derived a range of estimates, either regional or cap-wide, of between 300 $kg\cdot m^{-2}$ and 1250 $kg\cdot m^{-2}$, depending on latitude. The north cap tends to the lower end of this range, while the south cap tends to the higher.

Despite the difference in albedo between the Cryptic and Bright regions, there appears to be no notable difference in their CMA at any time during springtime retreat (Kieffer *et al.*, 2000; Prettyman *et al.*, 2009). This further obfuscates the processes involved on the southern cap and why the cryptic and anti-cryptic regions occur where and when they do.

1.1.3 Thermal Inertia

Thermal inertia is defined as $I = \sqrt{k\rho c}$, where k is the thermal conductivity, ρ is the density, and c is the specific heat capacity. A material has a high thermal inertia when it can absorb large amounts of energy with only a minor increase in temperature. The thermal conductivity is the primary variable in this because the factor ρc varies by only a factor of 2 - 4 for most geologic materials. The polar regions tend to have very high thermal inertias in the range of 300 to 5000 TIU (Thermal Inertia Units - $J{\cdot}m^{-2}{\cdot}K^{-1}{\cdot}s^{1/2}$) (Putzig and Mellon, 2007) because there is a high percentage of water ice in the subsurface on both poles that increases the effective conductivity (Feldman *et al.*, 2003; Prettyman *et al.*, 2004).

Typically, the effects of regolith thermal inertia are neglected from polar energy balance calculations, with the argument that the surface would likely have radiated any heat during the polar night before deposition occurs (Paige and Ingersoll, 1985) and that heat conduction is relatively small compared to the radiative terms. However, Haberle *et al.* (2008) showed that seasonal Viking pressure curves could be matched accurately when with general circulation model (GCM) predictions when utilizing a two layer soil model indurated with ice at variable depth. This implies that conduction may be sufficient to inhibit fall deposition of CO_2 frost. The soil model is a good

7

representation of the north cap, which is known to have a high percentage of water ice in the near-surface regolith (Feldman *et al.*, 2003). It is unclear how applicable it is to the south cap with the Haberle *et al.* (2008) two-layer model overestimating the mass condensed on the south pole. Haberle *et al.* (2008) suggest that better characterization of spatial and temporal variations could reconcile this discrepancy.

Piqueux *et al.* (2016) showed that temperature variations on low-latitude, low-thermal-inertia units during the night cool sufficiently to reach the frost point of CO_2. This results in a diurnal cycle where frost is deposited in layers a few hundred microns thick (assuming 0% porosity). This could potentially be thicker granted any substantial porosity, which is common in hoarfrosts. Diurnal CO_2 frosts are thought to sublime rapidly, just after local sunrise. Calvin *et al.* (2017) reported seasonal re-condensation events at high-latitude during southern polar cap recession. With temperatures near the frost point, low thermal inertia units could perform a role similar to that at low-latitudes on the seasonal caps with longer stability timescales.

1.2 Kuiper Belt Objects

1.2.1 Medium Sized KBOs

KBOs can be classified into three distinct size ranges: small (< 500 km radius), medium (500 - 1000 km radius), and large (> 1000 km radius). Small KBOs are characterized by complete loss of surface volatiles such as CH_4, N_2, and CO, while large KBOs (e.g., Pluto, Eres) have surface volatile ice detections of these species. Due to their large size and high magnitude, the large KBOs are fairly well studied (McKinnon *et al.*, 2008). Medium-sized KBOs are generally too small to have re-

tained surface volatiles, though tend to have strong water ice absorption suggesting a compositional change with size (Brown *et al.*, 2012).

Crystalline water ice is present on all sizes of KBOs (Grundy *et al.*, 1999), identified by its unique 1.65 μm spectral feature (Jewitt and Luu, 2004). This is strange, because at the surface temperatures for most KBOs (30 - 70 K) only amorphous water is stable (Jenniskens *et al.*, 1998). Surface temperatures would need to be upward of 150 K to have stable crystalline water ice. Additionally, crystalline ice is disassociated into amorphous ice by galactic cosmic rays (Mastrapa and Brown, 2006) and solar ultraviolet photons (Leto and Baratta, 2003) on relatively short geologic timescales. (Cook *et al.*, 2007) estimated that these processes together would annihilate crystalline water ice from the upper 350 μm of a an icy body in about 0.03 Myr.

Identification of a spectral feature at 2.21 μm has been reported for Charon (Dumas *et al.*, 2001; Cook *et al.*, 2007), Quaoar (Jewitt and Luu, 2004), and Orcus (Barucci *et al.*, 2008). This feature has been definitively identified as ammonia hydrate on Charon (Grundy *et al.*, 2016; Dalle Ore *et al.*, 2018). However, similar to crystalline water ice, ammonia hydrates should be disassociated on timescales of 1 Myr (Cook *et al.*, 2007). Multiple hypotheses have been presented to alleviate this and the water ice discrepancy.

Porter *et al.* (2010) developed a thermal model that showed micrometeorites (i.e., dust) deposit sufficient kinetic energy upon impact to anneal water ice to its crystalline form. They weighed annealing timescales against disassociation timescales from solar ultraviolet and galactic cosmic rays and still found micrometeorite impacts should be sufficient to sustain crystalline water ice on the surface for every KBO modeled. This process, however, cannot account for ammonia hydrates on the surface.

Cruikshank *et al.* (2015) and Dalle Ore *et al.* (2018) proposed that diffusion of ammonia from subsurface layers undergoing hydration reactions is the most likely scenario. However, it is not clear if this process meets the dissociation timescales for this species.

Delivery of warm, ammonia-water liquid in cryovolcanic resurfacing events would create both crystalline water ice and ammonia hydrates on the surface (Cook *et al.*, 2007) provided there is a method to transport the ammonia-water cryomagma to the surface. With the observations of New Horizons at the Pluto system, it now appears as though cryovolcanism is less likely a renewal agent. It is more likely a combination of diffusion and impact gardening responsible for crystalline water and ammonia hydrates (Holler *et al.*, 2017; Dalle Ore *et al.*, 2018).

1.2.2   New Horizons

The New Horizons spacecraft made its flyby of the Pluto system in 2015, giving scientists their first detailed examination of KBOs (Stern *et al.*, 2015). Upon arrival, New Horizons revealed Charon to be geologically complex.

Charon's surface is divided into two distinct morphological hemispheres (Stern *et al.*, 2015). The northern hemisphere is heavily cratered, with estimated ages of over 4 Ga (Moore *et al.*, 2016). This hemisphere is characterized by intense relief, with extensional tectonic features of up to 10 km (Moore *et al.*, 2016). The southern hemisphere, Vulcan Planum, is also heavily cratered, with similar age estimates of 4 Ga - though errors in these crater counts are high (Vulcan Planum could be as young as 300 Myr) (Desch and Neveu, 2017). This hemisphere has lower relief than its northern counterpart, though it does have extensional tectonic features. Other

morphological units include pancake shaped units, and lobate depressions suggestive of cryovolcanism (Moore *et al.*, 2016). The southern plains also contain Kubrik Mons a 3 - 4 km conical mountain that resides in a "moat," likely a remnant cryovolcano (Desch and Neveu, 2017). Charon's most notable feature is Serenity Chasma, a 50 km extensional graben 5 km deep that trends along the equator (Stern *et al.*, 2015; Moore *et al.*, 2016). The pervasive extensional features suggest a global areal strain of 1%, entirely consistent with the freezing of a sub-surface ocean (Beyer *et al.*, 2017).

Investigation of surface composition using the Ralph instrument (Reuter *et al.*, 2008) on board New Horizons showed that ammonia hydrates and crystalline water ice were distributed approximately uniformly across Charon (Dalle Ore *et al.*, 2018). Higher concentrations of ammonia hydrates are found in bright rays of craters (Grundy *et al.*, 2016), Serenity Chasma, bright ejecta, and some in-filled craters (Dalle Ore *et al.*, 2018). There is no enhancement in the southern plains, nor around Kubrik Mons. These observations suggest that cryovolcanism likely is not the replenishment method for ammonia hydrates and crystalline water ice (Holler *et al.*, 2017; Dalle Ore *et al.*, 2018). Despite this, the surface shows an exorbitant amount of cryovolcanic features indicating that resurfacing by cryolavas occurred at some point in the past.

1.2.3 Cryovolcanism

Cryovolcanism is the eruption of liquid or vapor phases (with or without entrained solids) of water or other volatiles that would be frozen solid at the normal temperature of an icy satellite's surface (Geissler, 2015). There is evidence for this activity on may outer solar system bodies (e.g., Titan (Lopes *et al.*, 2007), Enceladus

(Hansen *et al.*, 2006), Triton (Kargel, 1994), etc.), however these bodies have had, or are still undergoing, extreme tidal heating that helps drive cryovolcanism and keep water liquid. On KBOs, tidal heating is absent. Temperatures in the Kuiper Belt are well below the freezing temperature for water. Therefore, for liquid cryomagmas to exist an "anti-freeze" must be present that depresses the freezing temperature of water. Ammonia suppresses the freezing point of water to 176 K (Stevenson, 1982; Hogenboom *et al.*, 1997), and as stated above, there is clear spectral evidence for its presence on midsized KBOs and confirmation of its presence on Charon. However, liquid water is denser than water ice and introduction of ammonia makes it denser (Croft *et al.*, 1988). This means high density subsurface cryomagmas are generally negatively buoyant. Despite this, there are still conceptual models that describe how to deliver it to the surface.

Crawford and Stevenson (1988) suggested that cracks on Europa self-propagate. This requires that a crack be initiated in the ice shell above the liquid that is then partially filled. Exsolved gasses create a pinched-off buoyant zone that rises to the surface while entraining liquid. Eruptions of this kind would be exude an eruptive foam.

Clathrate hydrates - cage-like structures of water ice that house one or more species of gas or liquid - were shown to be stable at temperatures indicative of the outer solar system (Lunine and Stevenson, 1985). The introduction of these guest species increase the density of ice. In high enough concentrations, the density of clathrate hydrates can exceed that of liquid water or an ammonia-water mixture and make the liquid positively buoyant. The disassociation of clathrate hydrates could also introduce volatile gas species that have been shown to aid in explosive cryovolcanism (Neveu *et al.*, 2015).

12

Fagents (2003) suggested that over-pressurization of a subsurface reservoir could promote ascent of negatively buoyant cryomagmas to the surface. This is due to water's unique property where-in the density increases as freezing occurs, compressing the remaining unfrozen fluid and pressurizing it. They showed that even relatively small conduits could ascend fluid a vast distance provided the viscosity was low enough. The viscosity of near-peritectic ammonia-water liquids is 2.5 Pa·s with the absence of crystalline solids (Kargel *et al.*, 1991). This viscosity should allow for meters-scale conduit ascent through hundreds of kilometers of ice (Fagents, 2003).

1.3 Motivation

Current research emphasis on the polar energy balance of Mars has been limited to cap-wide studies and regional scale studies. However, local scale polar energy balance studies are lacking and therefore CMA and CROCUS dates on small (kilometers) spatial scales have not been thoroughly examined. While seasonal studies of brightness variations of polar ice during sublimation have been done on these scales, no attempts have been made to relate these variations quantitatively to frost-free surface properties.

What are the local variations in CMA on the polar caps of Mars? How do these variations change while ice sublimes over spring? Do frost-free surface properties affect the way seasonal ice sublimes? What implications does this have for the microphysical state of the ice? In Chapter 2, energy balance methods are used to probe the CMA on the Southern Polar Cap. Chapter 3 discusses correlations between the frost-free surface and seasonal ice on the South Pole.

Many studies have investigated the plausibility of ammonia-water cryovolcanism

in the Kuiper Belt and Outer Solar System. These studies have done excellent analytical analyses of these systems, but no robust fluid dynamic or thermophysical models exist.

Is liquid ammonia-water cryovolcanism feasible on medium-sized KBOs? What is the behavior of the cryomagma in conduits as it ascends and cools? A thermal hydraulic numerical model is developed and discussed in Chapter 4.

Chapter 5 summarizes the findings herein and discusses future work to further understanding of these dynamic ice systems.

Chapter 2

SPRINGTIME MASS ACCUMULATION ON SOUTH POLAR GULLIES NEAR SISYPHI CAVI USING THEMIS AND HIRISE

The polar caps of Mars undergo seasonal exchange with the atmosphere, incorporating 25% of the mass annually (James *et al.*, 1992; Kelly *et al.*, 2006). Understanding the current seasonal exchange is integral in understanding the past climate of Mars. Seasonally condensed material is primarily CO_2 ice, however there is evidence of water ice condensation in late spring on the South Polar cap (Brown *et al.*, 2010). The amount of mass per unit area - or Column Mass Abundance (CMA) - condensed on the surface is determined by the polar energy balance, i.e, the difference between the solar energy absorbed and infrared radiation emitted. Previous studies have focused on large scale surveys (Kieffer *et al.*, 2000; Kieffer and Titus, 2001; Titus *et al.*, 2001; Feldman *et al.*, 2003; Prettyman *et al.*, 2009; Kelly *et al.*, 2006; Litvak *et al.*, 2004, 2007; Piqueux *et al.*, 2015), using a wide variety of instrumentation.

Mars Global Surveyor (MGS) Thermal Emission Spectrometer (TES) (Christensen *et al.*, 2001; Kieffer *et al.*, 2000; Kieffer and Titus, 2001; Titus *et al.*, 2001; Mount and Titus, 2015), Mars Reconnaissance Orbiter (MRO) Mars Climate Sounder (MCS) (Mccleese *et al.*, 2007; Piqueux *et al.*, 2015), MGS Mars Orbiter Laser Altimeter (MOLA) (Aharonson *et al.*, 2004; Smith *et al.*, 2001a,b), Mars Odyssey (MO) Gamma Ray Spectrometer (GRS) (Boynton *et al.*, 2004; Kelly *et al.*, 2006), MO High Energy Neutron Detector (HEND) (Litvak *et al.*, 2004, 2007), and MO Neutron Spectrometer (NS) (Prettyman *et al.*, 2009) data have been used for comprehensive studies of the CMA on the South Polar Seasonal Cap (SPSC) of Mars. Local-to-regional scale col-

umn mass abundance studies are lacking, but could prove insightful to the behavior of seasonally deposited ice. Of particular interest is the depositional mode, whether direct or atmospheric, and the pattern of sublimation.

Energy balance calculations, the difference between the absorbed incoming solar radiation and the outgoing emitted thermal radiation to space, estimated from TES observations suggested cap sublimation budgets of up to 1250 kg·m^{-2} (Kieffer *et al.*, 2000; Paige and Ingersoll, 1985) (i.e, the amount of mass per unit area available to be sumlimed). However, the Mars Odyssey THermal EMission Imaging System (THEMIS) has considerably better spatial resolution and collects infrared radiance at comparable wavelengths (Christensen *et al.*, 2004). This instrument can be used to estimate CMA on the polar caps with the same methodology, with only minor modifications. Mount and Titus (2015) showed that regional-scale bulk densities were often lower than global-time averages. This disparity could be explained by regional-scale variations in the CMA that are being smoothed-out on the global scale, but no studies of this kind have been done. This study will attempt to resolve local and regional scale discrepancies by using THEMIS observations coupled to high resolution albedo data.

2.1   Data

Data for this study were taken from High Resolution Imaging Science Experiment (HiRISE) (McEwen *et al.*, 2007) RED band Reduced Data Records (RDR) and THEMIS RDRs. While HiRISE has unprecedented spatial resolution, the reason these data were used in this study was because the repeat coverage of the Region of Interest (ROI) was exceptional. The ROI is located at 68°S, 1.3°E in a polar pit
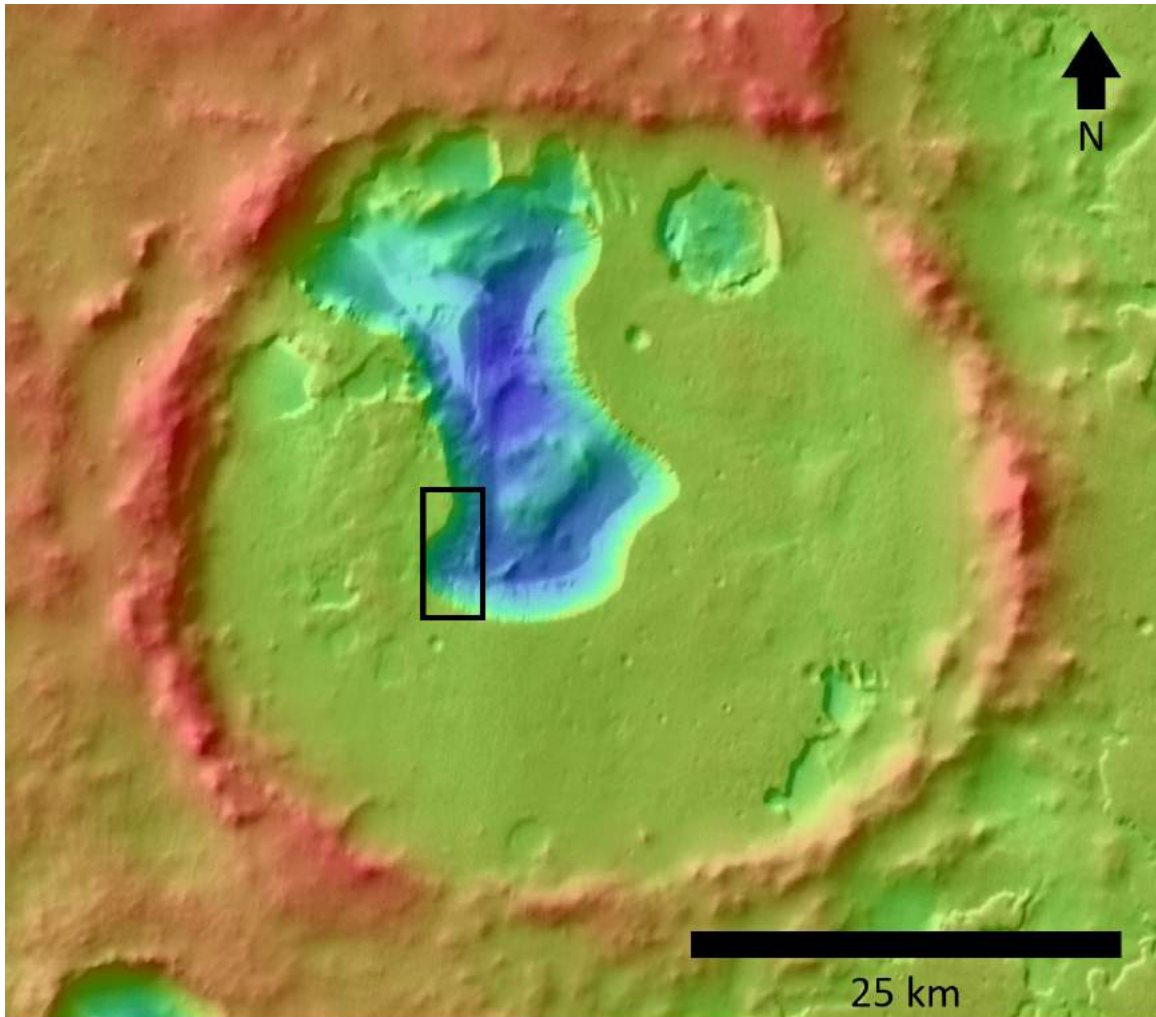
Figure 1. Region of Interest

THEMIS daytime infrared over MOLA elevation at 68°S, 1.3°E. The rectangle encompasses the Region of Interest.

inside an 50 km impact crater, just north of Sisyphi Cavi (Figure 1). The image set contained five Mars Years (MY) of coverage, with images that spanned 128° L_s from 160 to 288°. The THEMIS data likewise have good temporal coverage, covering just over two MYs and spanning 140° L_s from 150 to 290°. One High Resolution Stereo Camera (HRSC) DTM was used to estimate slopes and slope azimuths.

Time of observation for the HiRISE images were fairly consistent at about 4:00 pm local solar time (LST). THEMIS RDRs in MY 26 morning observations were taken at around 6:30 am LST. Morning observations shifted in time to around 6:30 am LST in MY 32 due to the change in orbit of Mars Odyssey. This continued in MY 33 where morning images were taken at about 8:00 am LST. Evening observations in MY 32 were taken at approximately 5:30 pm LST, while MY 33 observations were taken at nearly 7:00 pm LST. These have little bearing on the computed effective temperature because the errors associated with diurnal amplitude are much lower than the instrument error (see §2.4).

This ROI was studied in detail by Raack *et al.* (2015) with a comparable data set. While their study was in-depth, they focused on the gully formation and evolution over the MYs covered in the HiRISE data set, with only discussion of ices in relation to the gully system. I will add to their work by complimenting it with more focus on the ice evolution in the pit.

Processing was done using the Integrated Software for Images and Spectrometers (ISIS). The HiRISE and THEMIS RDRs were projected to a polar stereographic projection, spatially convolving all pixels through nearest neighbor interpolation. I degraded the HiRISE images to THEMIS resolution (100 m/pix (Christensen *et al.*, 2004)) so the pixel convolution was 1:1, as well as to save on hard disk space and processing time. All images were masked to the frame with the smallest spatial extent, which was determined manually through footprint overlay in QMOS. These were then exported to fits images for further computations in MATLAB.

HiRISE images are shown in Figure 2. The sublimation pattern in the ROI makes it a prime candidate for small-scale investigations. The differences in the surface ice as it evolves over spring appear isolated to geomorphic units and appear to have

Table 1. List of Data Used in this Study

The HiRISE data spans five consecutive MYs, while THEMIS spans approximately two.

ImageID	Bands	LST	L_s	MY
HiRISE				
ESP_011396_1115	RED	16.3	183	29
ESP_011607_1115	RED	16.3	193	29
ESP_011752_1115	RED	16.2	199	29
ESP_011963_1115	RED	16.2	209	29
ESP_012319_1115	RED	16.0	226	29
ESP_012332_1115	RED	15.7	227	29
ESP_012741_1115	RED	15.8	247	29
ESP_013097_1115	RED	15.4	265	29
ESP_013585_1115	RED	15.2	288	29
ESP_020956_1115	RED	16.0	218	30
ESP_021589_1115	RED	15.7	249	30
ESP_021668_1115	RED	15.4	253	30
ESP_022156_1115	RED	15.2	277	30
ESP_028657_1115	RED	16.1	167	31
ESP_028802_1115	RED	16.0	173	31
ESP_029013_1115	RED	16.1	183	31
ESP_029079_1115	RED	16.2	186	31
ESP_029369_1115	RED	16.0	199	31
ESP_029580_1115	RED	16.1	209	31
ESP_029725_1115	RED	15.9	215	31
ESP_029936_1115	RED	15.9	226	31
ESP_030002_1115	RED	16.0	229	31
ESP_030147_1115	RED	15.8	236	31
ESP_030503_1115	RED	15.5	254	31
ESP_030701_1115	RED	15.7	263	31
ESP_037452_1115	RED	16.1	166	32
ESP_037729_1115	RED	16.3	178	32
ESP_038283_1115	RED	16.4	203	32
ESP_038428_1115	RED	16.2	210	32
ESP_038903_1115	RED	16.0	233	32
ESP_039114_1115	RED	15.8	243	32
ESP_039615_1115	RED	15.3	268	32
ESP_046116_1115	RED	15.8	160	33
ESP_046472_1115	RED	15.8	175	33
ESP_046538_1115	RED	16.6	178	33
ESP_047461_1115	RED	15.9	220	33
ESP_047593_1115	RED	16.1	227	33
THEMIS				
I05924010	4, 9, 10	6.00	169	26
I06673007	4, 9, 10	5.89	205	26
I56796005	1 - 10	7.24	207	32
I57326002	1 - 10	17.6	234	32
I57445006	1 - 10	6.66	241	32
I57663006	1 - 10	17.4	252	32
I57782010	1 - 10	6.44	258	32
I57975007	1 - 10	17.2	268	32
I58094006	1 - 10	6.20	274	32
I58287004	1 - 10	17.0	284	32
I58406005	1 - 10	6.02	290	32
I63902003	1 - 10	18.8	150	33
I63971002	4, 9, 10	7.82	153	33
I64707005	1 - 10	7.94	186	33
I64944005	1 - 10	7.98	198	33
I65112009	1 - 10	18.9	206	33
I65181009	1 - 10	7.93	209	33
I65798009	1 - 10	18.5	241	33
I65867006	1 - 10	7.49	245	33
I66459002	1 - 10	17.9	276	33
HRSC				
H2357_0000	-	-	324	27

geographic dependence. Gully fans tend to have brighter material, while blocky units are darker. South-facing slopes maintain bright material until late spring. In all frames there is a general brightening in the southeastern sector of the ROI that is likely due to slope effects. An attempt to correct for these effects is made when estimating the absolute albedo (see §2.2).

2.2 Methods

The amount of mass accumulated per unit area is computed with the sublimation budget method of Kieffer and Titus (2001). This is done by integrating the net diurnal incoming and outgoing flux.

$$\Delta M = \frac{1}{L_f} \int_{L_s}^{C} (1 - A)\frac{F_\odot}{r_{AU}^2}\langle \cos i \rangle - \sigma_B \langle T_{eff}^4 \rangle \mathrm{d}t \qquad (2.1)$$

where L_s is the solar longitude, C is the L_s at which Cap Recession Observations indicate CO_2 has Ultimately Sublimed (the CROCUS date) (Kieffer *et al.*, 2000), A is the albedo, $F_\odot$ is the solar flux, r_{au} is the semi-major axis in AU, $\langle \cos i \rangle$ is the diurnally averaged local incidence angle, σ_B is the Stefan-Boltzmann constant, and $\langle T_{eff}^4 \rangle$ is the diurnally averaged effective temperature. The flux balance assumes no lateral heat transport, and that any excess energy in the column is put into the latent heat of fusion (Paige and Ingersoll, 1985).

2.2.1 Albedo

HiRISE data were used to calculate seasonal albedos. The absolute error on the HiRISE albedos is $\approx \pm 30\%$ (McEwen *et al.*, 2007), due to the lack of a calibration
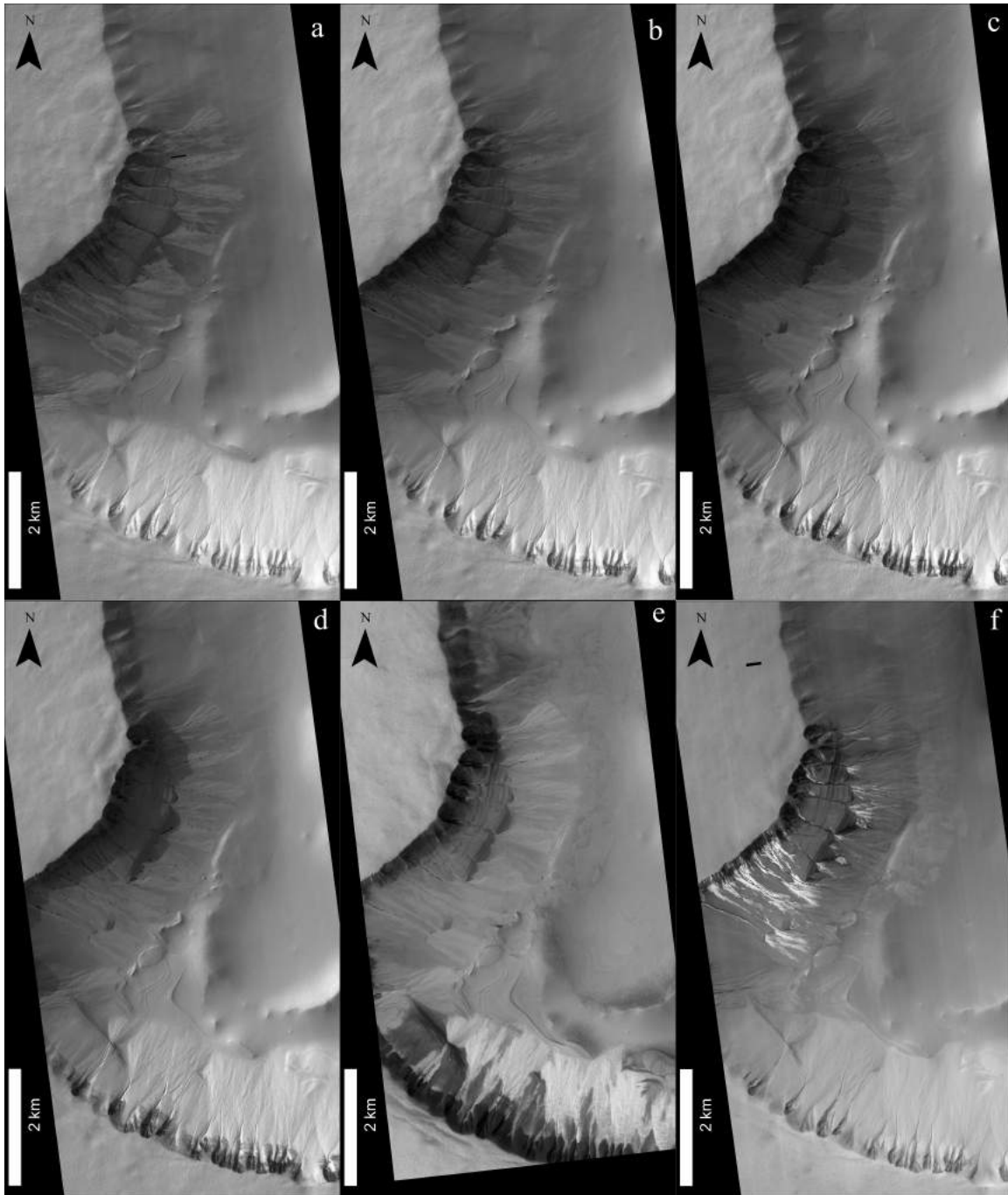
Figure 2. HiRISE Relative Brightness Images of the ROI in MY 29

$L_s \approx 183$ (a), 193 (b), 199 (c), 209 (d), 226 (e), and 247° (f). Surface material darkens along the boulder-laden scarps over time. North-facing slopes tend to be brighter than other slopes, and gully fans tend to be brighter. By late spring, north-facing slopes become darker than other slopes and there is a stark contrast ice on the scarp and on the fans. At the end of spring, bright material is apparent in the south facing scarp gullies.

target on this instrument. Despite this relatively large error, HiRISE provided exceptional temporal coverage of the ROI, covering multiple MYs at high L_s density. Analysis of these errors were shown to be negligible when propagated through the energy balance calculations. In an attempt to reproduce the methodology of Kieffer and Titus (2001), a Lambertian photometric function was used. However, slope effects were apparent within the images. Thus, I modified the incidence angle from HiRISE using geometry from the HRSC DTM. This simple adjustment was computed by

$$i_{corr} = i - \tan^{-1}\left[\cos\left(\phi - \phi_\odot\right)\tan\theta\right] \tag{2.2}$$

where ϕ is the azimuth of the surface normal, $\phi_\odot$ is the sub-solar ground azimuth, and θ is the slope in degrees. This can lead to negative incidence angles where the slope is greater than the local incidence angle and the surface normal azimuth is out of phase with the sub-solar ground azimuth. In this case, the incidence angle is left unmodified, reducing back to a Lambertian photometric function. While crude, it is beyond the scope of this work to account for the complex lighting conditions for shaded diffuse reflectors.

The albedo is then calculated from HiRISE I/F radiance, $R_{I/F}$, by

$$A = \frac{R_{I/F}}{\cos i_{corr}} \tag{2.3}$$

Due to the sparsity of data, the albedo is assumed to evolve linearly between consecutive frames. Consequently, the albedo is linearly interpolated from frame-to-frame every day. The flux is then computed assuming the albedo is constant over the day.

2.2.2 Diurnally Averaged Incidence Angle

The diurnally averaged incidence angle was calculated by integrating the time-varying incidence angle from trough-to-trough. The hourly incidence angle can be estimated by spherical geometry arguments

$$i = \cos^{-1}\left(\sin L_s \sin \Omega + \cos L_s \cos w \cos \Omega\right) \tag{2.4}$$

where Ω is the latitude, and w is the hour angle. The hour angle is computed from

$$w = 180° \cos\left[\frac{\pi}{2}\left(\frac{H}{12} + \frac{\Lambda}{180} - 1\right)\right] \tag{2.5}$$

where H is the local solar time (LST) and Λ is the longitude. The LST is approximated by dividing the L_s by least-squares fitting a sine curve to the average monthly L_s per day scaled to 668 days. This returns the LST, and therefore, the hour angle in terms of L_s, which is far more convenient to work in.

$$H = \frac{L_s}{A \sin\left[2\pi(BL_s + C)\right] + D} \tag{2.6}$$

Here, A, B, C, and D are free parameters that are swept to find the best fit. After solving for all unknowns the cosine of i is evaluated and set to 0 where the sun is below the horizon. This is then integrated from trough-to-trough each day. The outcome is input into the flux balance.

2.2.3 Effective Diurnal Temperature

Diurnal effective temperatures are computed with the methodology detailed in Kieffer and Titus (2001). This method has been utilized in other studies when deriving flux balance on the 10s of kilometers scale (Titus *et al.*, 2001; Mount and Titus, 2015), but never at 100 m scale of THEMIS.

The technique assumes a sinusoidal diurnal temperature curve with an amplitude equal to a morning and evening temperature taken from the TES thermal bolometer.

$$T_H = T_0 - \xi \cos\left(\frac{\pi H}{12}\right) \tag{2.7}$$

where

$$T_0 = \frac{T_{pm} + T_{am}}{2} \tag{2.8}$$

and

$$\xi = \frac{T_{pm} - T_{am}}{2} \tag{2.9}$$

Here, I use temperature from THEMIS calculated by performing a chi-squared minimization blackbody fit to the radiance from all 10 bands. While not a complete sample of the spectrum, it has the benefit of accounting for the emissivity while only having a small sub-sample of the thermal infrared spectrum. Because the technique assumes vertical homogeneity and total surface and atmospheric losses radiated space, it is important to use all bands, rather than just surface or atmospheric bands. This is also why no atmospheric correction were made. Temperatures are computed pixel-by-pixel for both day and night observations.

The night and day temperatures are linearly interpolated over the sublimation season to compensate for data sparsity. The temperatures are then input into the analytical solution for T_H^4 integrated over the day (time-averaged).

$$\langle T_{eff}^4 \rangle = T_0^4 + 3T_0^2\xi^2 + \frac{3}{8}\xi^4 \tag{2.10}$$

2.2.4   CROCUS Date

The CROCUS dates were defined to be when the band 9 (12.6 μm) temperature, which is a proxy for surface kinetic temperature (Christensen *et al.*, 2004), exceeds

the CO_2 sublimation temperature and the surface albedo is less than or equal to the frost-free albedo.

To account for atmospheric effects and sub-pixel mixing, the required sublimation temperature in band 9 is assumed to be 165 K. This value is consistent with the thermal inflection method of Kieffer *et al.* (2000), Kieffer and Titus (2001), Titus *et al.* (2001), and Mount and Titus (2015). The exact temperature is not crucial, because it only sets the lower limit of the CROCUS date, with the albedo having the upper limit (and more sensitive) control. The sublimation temperature was modulated from 150 to 175 K to confirm this assertion, with little-to-no effect on the CROCUS dates. This is because the temperature constraint would only have an effect if the albedo constraint (see below) would occur around the same L_s as the date of temperature increase. However, THEMIS band 9 temperatures exceed the frost point of CO_2 much earlier in spring than surface albedos compare with the frost free surface albedo.

The frost-free albedo is assumed to be the late-summer, slope-corrected albedo estimated from latest L_s, post-solstice HiRISE image. Due to the high uncertainty in these albedos, I conservatively assume the albedo is 30% higher (equivalent to the absolute error) than that observed. This puts an upper limit on the CROCUS date.

2.2.5 Ice Depth

Ice depths would reveal a great deal about the seasonal ice, because density, and therefore porosity, may be derived from it. The best method for estimating depth of ice at these scales is through measurement of seasonal changes in length of boulder shadows (Cull *et al.*, 2010; Mount and Titus, 2015). However, due to a dearth of boulders on the scarp faces, fans, and pit floor, estimates could only be made on the

top of pit, south of the southern scarp edge. These depth estimates were made using the technique of Cull *et al.* (2010) and the crown-moat correction of Mount and Titus (2015).

A set of 30 boulders were measured to acquire a very simple estimate for the regional depth. The technique is sensitive to the number of frames used and to the depth measured in consecutive frames. Therefore only the MY 29 subset of images were used. These are illustrated in Figure 10.

2.3 Results

Figure 3 details the combined 5 MY interpolated albedo over springtime sublimation. Initial albedos in the ROI are relatively low. The regionally averaged albedo is approximately 0.19 at $L_s \approx 160°$. This is nearly the same as the frost-free albedo of 0.17. The local albedo is fairly consistent (at around 0.20), with the south facing scarp having slighly lower albedos than the regional average (about 0.15). The lowest albedos found in early spring are located on the north-facing gully scarp in the southern sector of the ROI, with a minimum of about 0.1. Artifacts are apparent from the incidence angle correction due to small scale variations of slopes in this area.

Generally, the ice albedo increases as spring progresses. Higher-than-average albedos are found atop the escarpment and select areas in the southern portion of the ROI during early-mid spring.

Regional albedos oscillate between 0.3 and 0.37 from $L_s \approx 194$ - $228°$ throughout mid-spring (Figure 4). The albedo peaks at this time. The ice on the south facing
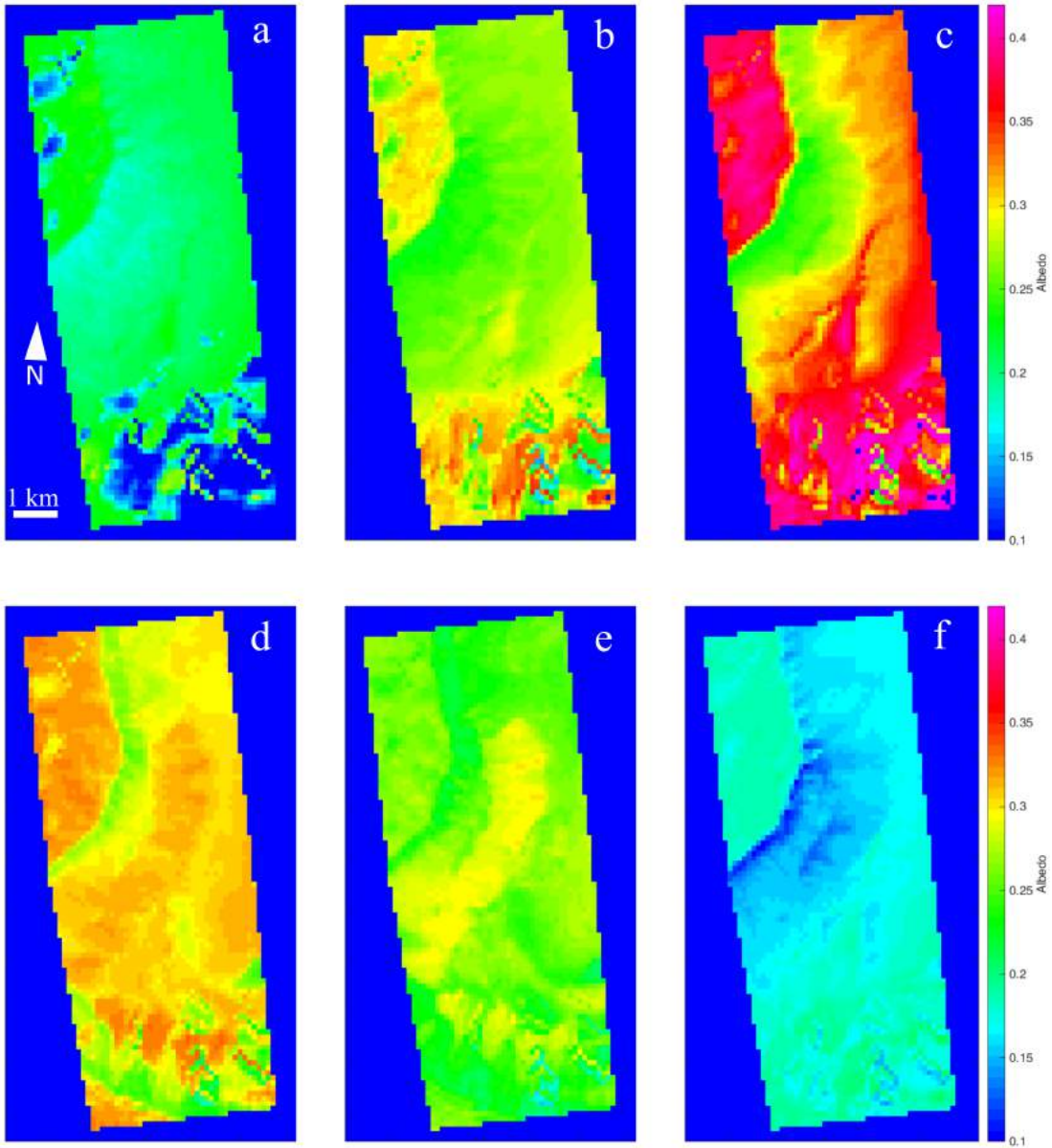
Figure 3. Local HiRISE Albedo at the ROI

$L_s \approx 159$ (a), 189 (b), 203 (c), 227 (d), 232 (e), and 288° (f). Regionally, albedos increase into mid-spring, then decrease toward late spring. The largest variations in albedo occur where there is the most illumination.
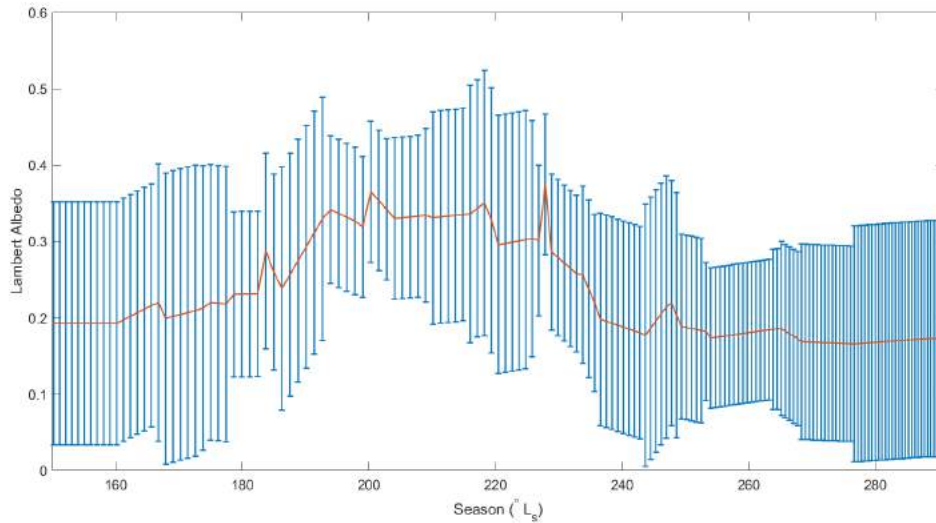
Figure 4. Regional HiRISE Albedo at the ROI

Lambert Albedo derived from regionally averaged HiRISE I/F radiance and incidence angle. Late winter albedo is relatively low for CO_2 ice indicating slab or dust. The albedo increases into mid-spring up to 0.37. Albedo reduces as spring progresses until the ROI is defrosted. Errors are computed assuming a conservative ±30% absolute error on the albedo value, which is propagated through the linear interpolation.

gullies remains a relatively constant albedo during this period, while the rest of the surface in the ROI brightens.

After $L_s \approx 228°$ there is a sharp decrease in albedo. The gully fan material continues to lag behind other units in the ROI. By $L_s \approx 237°$ the regional albedo has decreased to nearly the frost-free albedo.

Early spring bolometric temperatures are noisy due to the low cap temperatures, with a regional average around 147 ± 4 K, consistent with the CO_2 frost point. The north facing scarp warms relatively quickly, as does the regional temperature. The local temperatures rise, more-or-less uniformly except on the north-facing scarp and south-facing scarp, where temperatures are higher-than-average and lower-than-

28

Figure 5. Local THEMIS Temperature at the ROI

$L_s \approx 159$ (a), 189 (b), 203 (c), 227 (d), 232 (e), and 288° (f). The temperature increases over spring uniformily except on the large escarpments. The south-facing remaining colder than the regional average and the north facing becoming warmer.
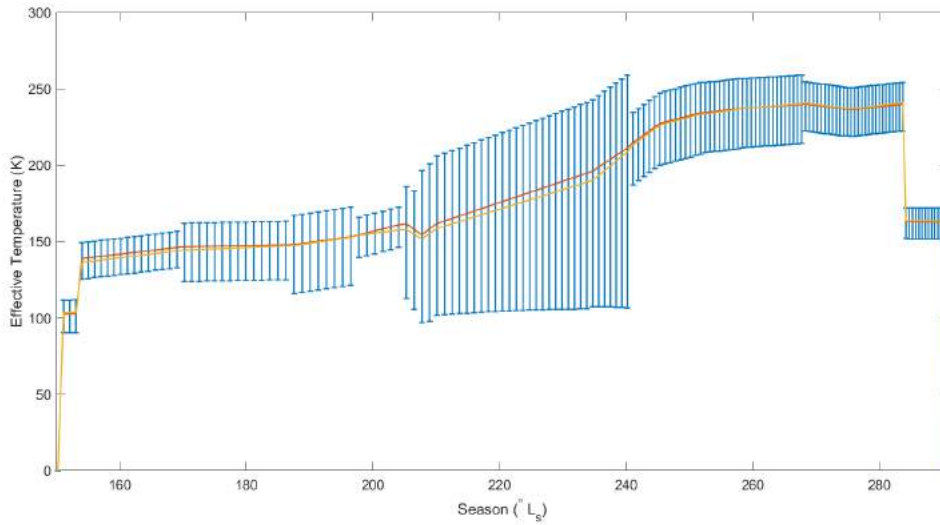
Figure 6. Regional THEMIS Temperature at the ROI

Diurnally averaged temperature derived from blackbody fit of regionally averaged THEMIS spectral radiance (red). Temperatures exceed 165 K after $L_s \approx 200°$. Regionally averaged THEMIS band 9 brightness temperatures (yellow) are shown for reference. Errors are propagated from the fit through the diurnal calculation. The high error in mid-to-late spring is from poor blackbody fits at these times.

average, respectively. The regional temperature reaches the sublimation temperature (defined at 165 K in this study) at around $L_S \approx 200°$ and increases until $L_s \approx 250$. At this time the temperature plateaus at about 240 ± 10 K (Figure 6).

THEMIS Band 9 brightness temperatures have the same general trends as the bolometric temperatures, though are on average a few Kelvin cooler. Because band 9 views in an atmospheric transparency band, there is little contribution to the temperature from the atmosphere. Thus we should expect it to be cooler than the 10 band fit temperature and more indicative of where surface ice is. This temperature difference is most apparent in mid spring when temperatures start to rise, but frost is still present on the south-facing scarp. There have been no atmospheric corrections
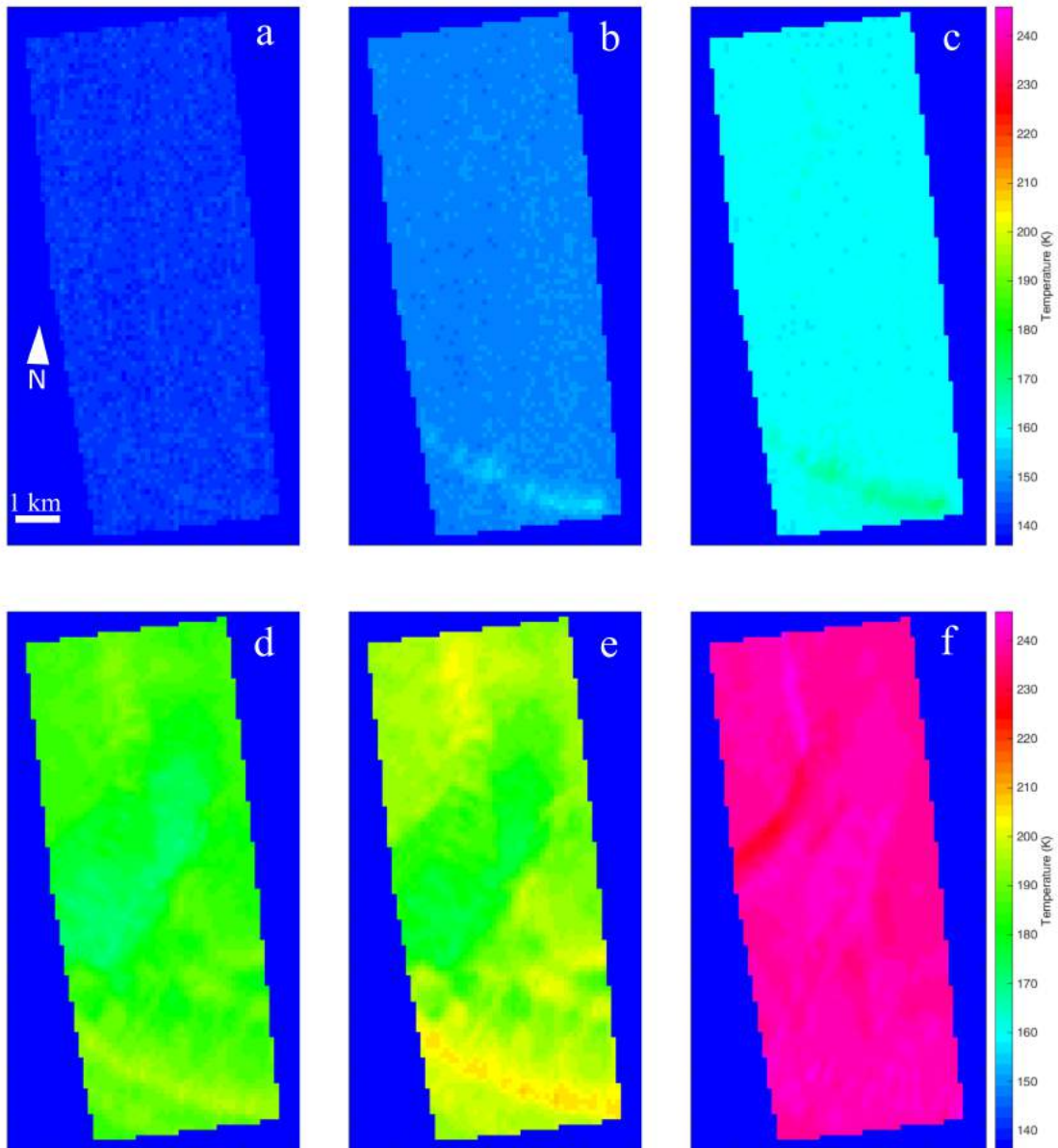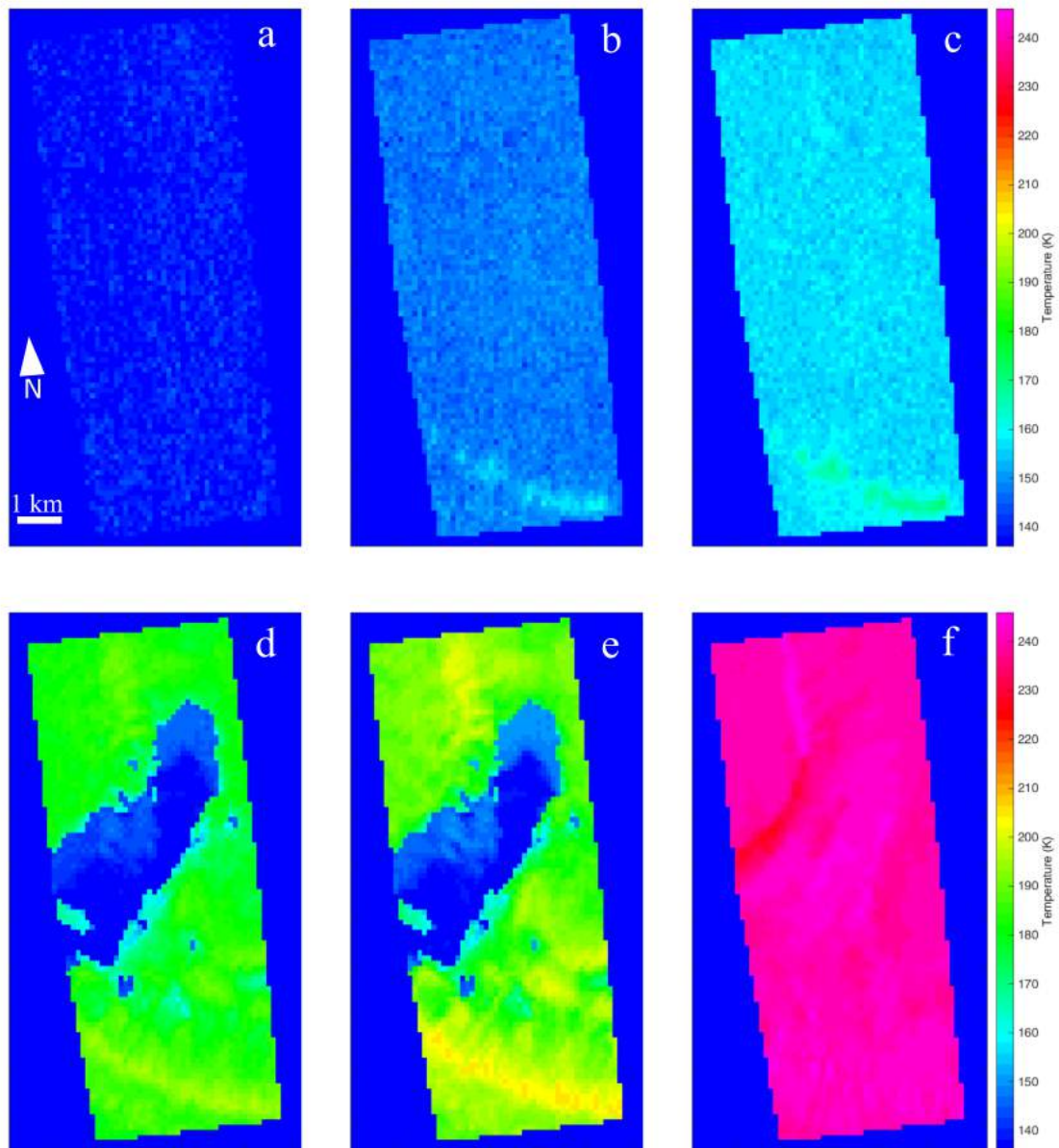
Figure 7. Local THEMIS band 9 Temperature at the ROI

$L_s \approx 159$ (a), 189 (b), 203 (c), 227 (d), 232 (e), and 288° (f). These follow the same trend as the best fit temperature, but are slightly noisier and a few Kelvin cooler. The south-facing scarp is much colder in band 9.

made to this data and thus the band 9 temperature may be above the frost point of CO_2 and ice still be present.

CROCUS dates on the north-facing scarp at the southern edge of the ROI and east-facing scarp in the northern sector predate the other portions of the ROI in every Mars Year. The fan material on the south-facing scarp in the center of the ROI has CROCUS dates that always lag behind the rest of the ice. MY 29, 30, and 32 have generally later CROCUS dates than other years, as well as the 5 year composite. MY 29 and 30 have particularly late CROCUS dates, some ice remaining until after $L_s \approx 250°$. These years still maintain the same geographic dependencies though, i.e. the north-facing scarp sublimates first, and the south facing scarp sublimates last. These results are consistent with zonally averaged retreat maps (Calvin *et al.*, 2017; Piqueux *et al.*, 2015; Kieffer *et al.*, 2000). In particular, the retreat maps of Calvin *et al.* (2017) in MY 29 indicate a time lag of 5 - 10° compared to other years precisely at this location. MY 33 has CROCUS dates that are far earlier than other years, however this year has a large gap in data in mid spring, where transitional albedos and temperatures would be critical. This CROCUS date is therefore highly speculative, and does not likely occur this early.

Figure 9 displays the CMA over springtime sublimation. The highest CMAs are located on the south-facing slope at around 900 kg·m^{-2}. Here, the gullies themselves have localized CMAs of up to 1000 kg·m^{-2}. The north-facing slope and the east-facing scarp in the northern sector of the ROI have the lowest CMAs having as little as 400 kg·m^{-2}. The pit floor has a relatively high CMA, while the plains at the top of the scarps have CMAs of approximately 600 kg·m^{-2}. These reduce over spring, as expected, following the same trends as the temperature and albedo.
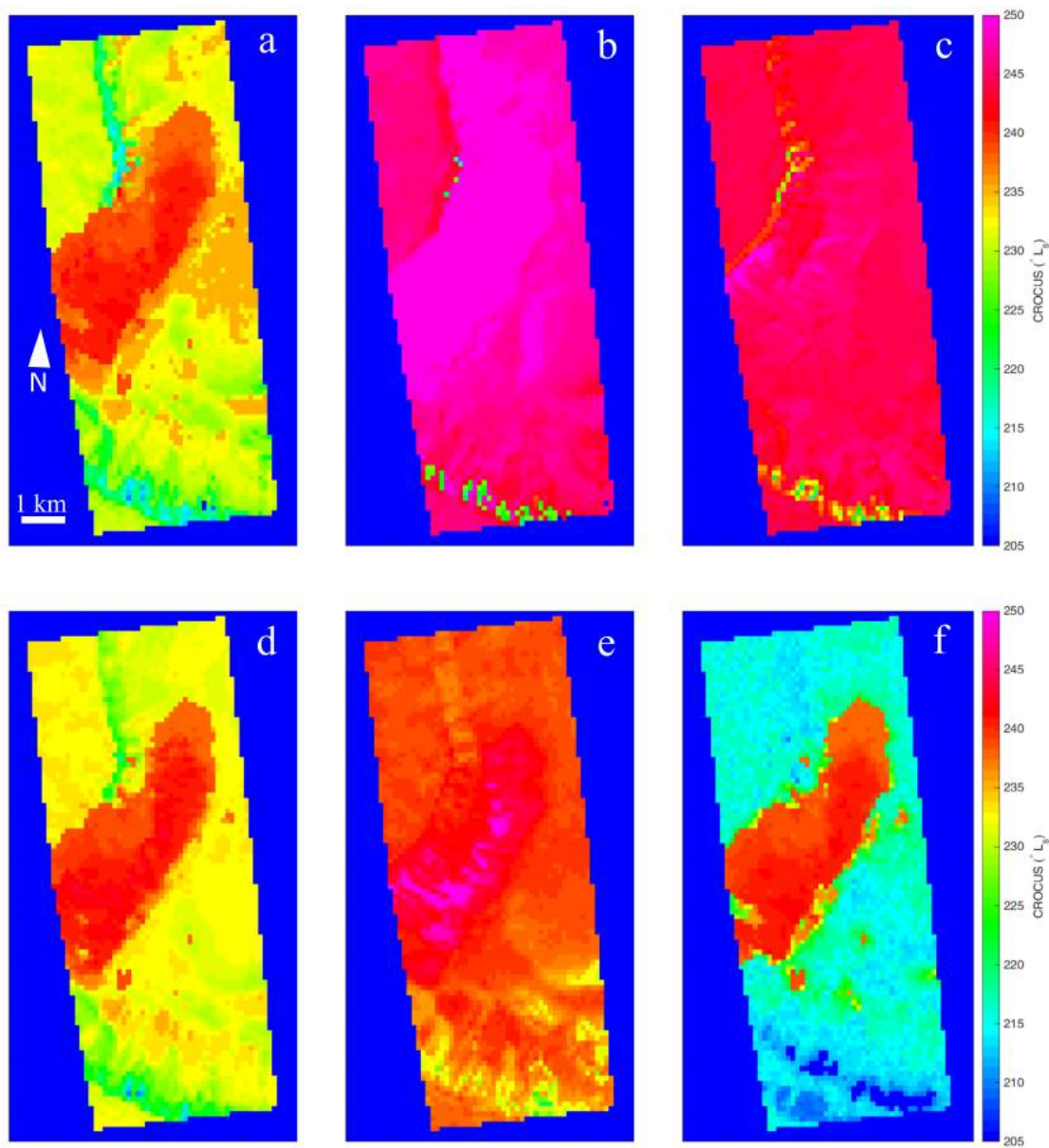
Figure 8. Local CROCUS Dates at the ROI

a). Five-year composite CROCUS. b). MY 29. c). MY 30. d). MY 31. e). MY 32. f). MY 33. CROCUS dates on the north-facing scarp at the southern edge of the ROI and east-facing scarp in the northern sector predate the other portions of the ROI in every MY. The fan material on the south-facing scarp in the center of the ROI has CROCUS dates that always lag behind the rest of the ice. MY 29, 30, and 32 have generally later CROCUS dates than other years, as well as the 5 year composite. MY 33 has CROCUS dates that are far earlier than other years.

33
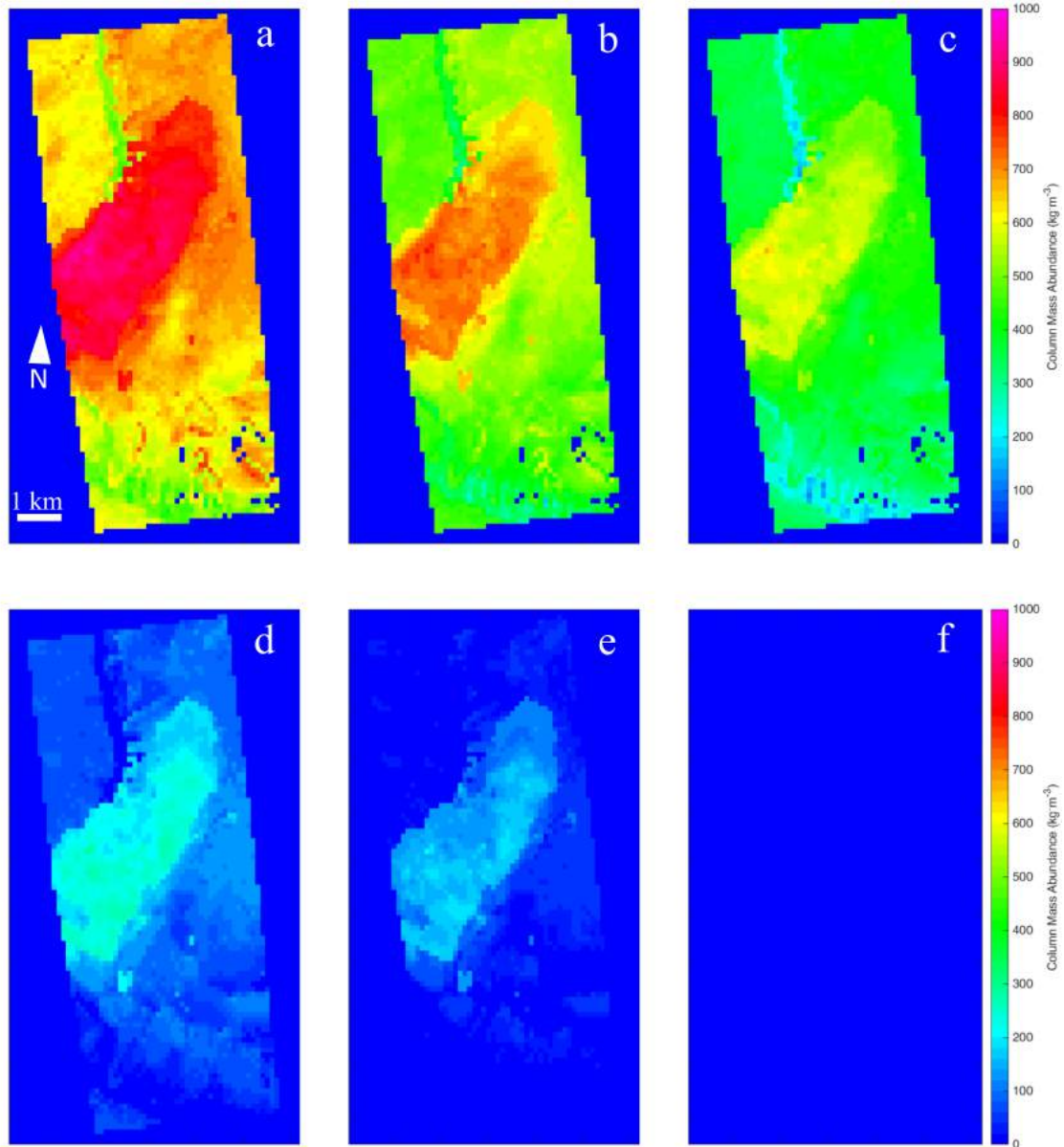
Figure 9. Local CMA at the ROI

$L_s \approx 159$ (a), 189 (b), 203 (c), 227 (d), 232 (e), and 288° (f). The south-facing gullies have high CMA, while the north-facing and "blocky" scarps have the lowest. This is likely due to a combination of thermal properties and illumination conditions (e.g. shade).
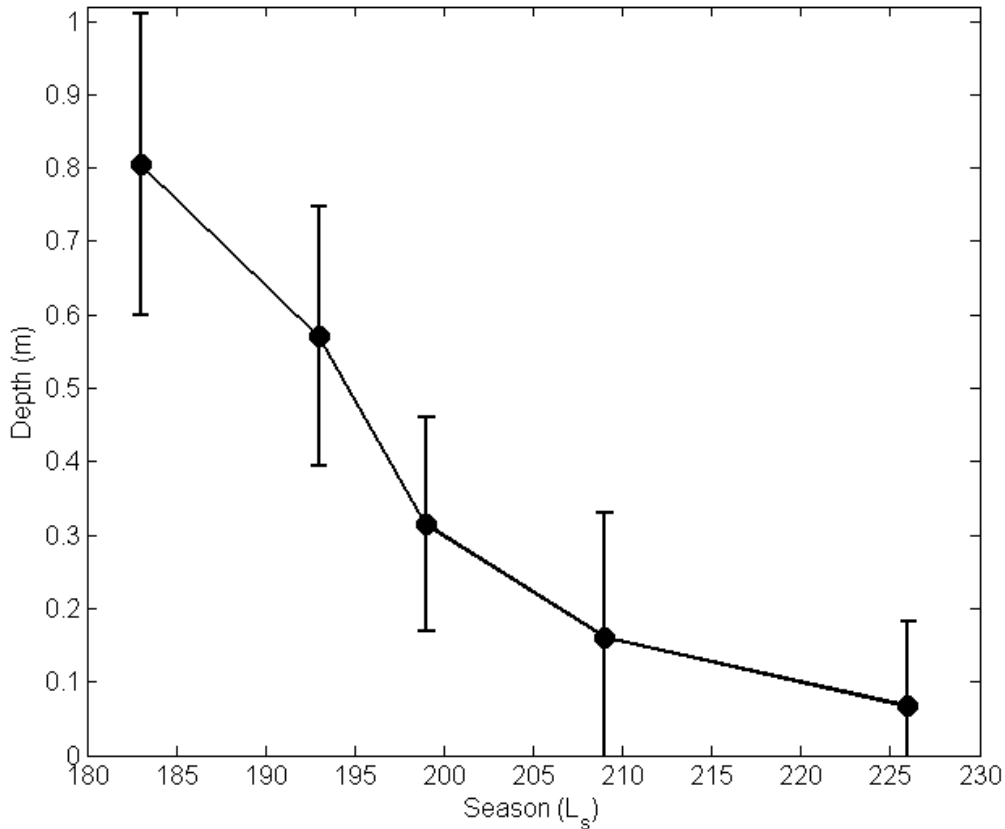
Figure 10. Ice depths for 30 rocks at the ROI in MY 29

Boulders were sampled south of the north-facing scarp in this ROI. The maximum depth at the beginning of spring is reasonable at this latitude. The depth at $L_s \approx$ 226° has error bars that could represent a zero depth, though the albedo variations at this time indicate the continued presence of surface ice. However, the depth is just at the limit of the resolution of the technique.

Depths of ice are at their maximum of 0.8 in early spring. Considering the max-imum depth of the southern seasonal cap to be around 0.9 m at 85°S latitude, 0.8 m at -68°S is quite high and may be closer to the lower end of the error bar. The depth decreases over spring, consistent with the sublimation of ice. Ice persists until about $L_s \approx 226°$, though the regional CMA would suggest that this is not the case. This

is likely due to the restricted measurement area and time and the error bars are still consistent with a depth of zero.

2.4 Discussion

2.4.1 Local Scale Variations

The evolution of the albedo in springtime is probably controlled by illumination factors because north-facing slopes begin spring bright, but are the first to decrease in albedo to the frost-free albedo value. The south-facing scarp is shaded for most of the day, which would explain why the albedo is more seasonally consistent than other areas in the ROI. When shaded, the ice would receive less incident radiation during sublimation. Fracturing occurs when ice is illuminated faster than it can radiate the energy away. Fractures cause an increase in albedo by reducing the effective grain-size. Self-compaction, settling, and annealing are all thought to occur in seasonal ice as well, but these reduce the albedo by increasing the affective grain-size. These competing affects can cause complex temporal variations in the ice. If the extent of fracturing is reduced (e.g., by having a shaded surface) the interactions between these processes are muted, therefore one would expect more consistently behaved albedo over springtime sublimation.

Lack of incident radiation would also explain the high CMA and late CROCUS date, because there are more losses to space than energy absorbed leading to relatively long-lived deposits and therefore high CMAs. However, there is a small contiguous extent of the gully fan unit to the northeast that receives more illumination than the rest of the unit. This extent of gully fans does have a slightly earlier CROCUS date

and lower CMA than the other south-facing gully fans, though the albedo is nearly the same as the shaded fans throughout spring. The gully fan unit appears to be finer-grained than other surrounding units, though it is beyond the limit of the HiRISE resolution to resolve the precise grain-size. Nonetheless, relative to the layered units on the north and south-facing slopes, which have easily resolvable '"blocks"', no such features exist on the gully fans. Therefore, the albedo could have secondary effects from the gully fan thermal inertia, but it is unclear. How thermal inertia could affect ice albedo is discussed in Chapter 3.

The temperatures are likewise affected by the facing of the slopes. The top of the north-facing scarp is the first to warm up during spring, but other north-facing slopes do not display the same level of temperature increase. Considering that the north-facing gully fans do not indicate a similar increase in temperature until late spring, the thermal properties of the surface must be the explanation. "Blocky" materials, such as the boulders at the top of both scarps, exhibit the highest temperature increases. It appears then that high thermal inertia units have muted CMA values, though no quantitative relationship is established here.

The CROCUS dates in MY 32 are of great interest, because the gullies themselves exhibit the latest CROCUS dates. Negative topography, like gullies and pits, should have higher average temperatures, because they operate like a thermal cavity. There have been observations of late-spring depressions maintaining frost after the surrounding topography has sublimated (Kossacki and Markiewicz, 2002; Hansen *et al.*, 2013), but nothing conclusive. It is still unclear why these depressions would persist.

The variations in the CMA are marked. The range of values covers the full range
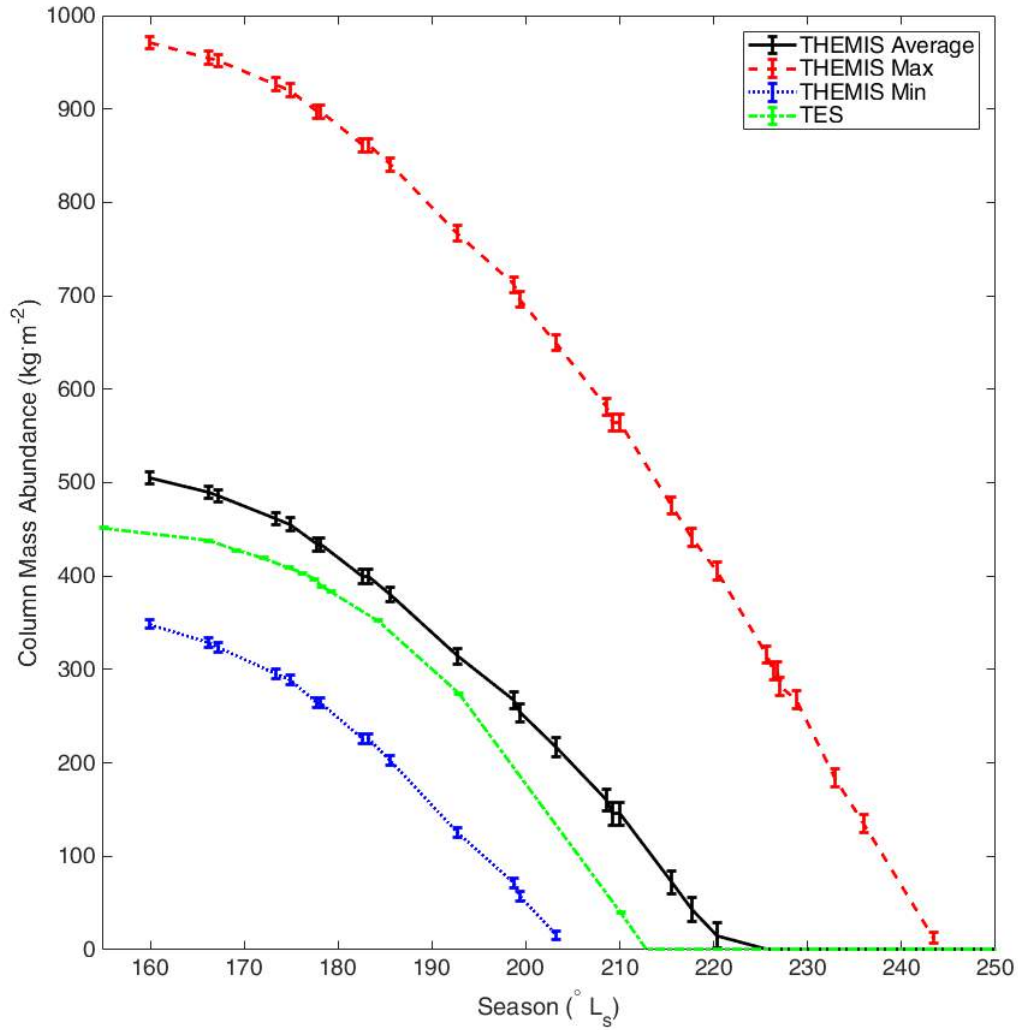
Figure 11. Regional THEMIS/HiRISE and TES CMA

Regional values are generally similar between TES and THEMIS, lending credence to the method. THEMIS/HiRISE estimates higher CMAs than TES are likely due to the high localized maximum on the south-facing scarp.

of estimates made for both the north and south poles of Mars (Kieffer *et al.*, 2000; Haberle *et al.*, 2004; Aharonson *et al.*, 2004; Prettyman *et al.*, 2009) all within 60 km^2.

2.4.2 Regional Scale and Interannual Variations

Time of day of observations were not taken at the maximum and minimum bolo-metric temperatures in the diurnal curve as predicted by KRC. TES and THEMIS do not observe at the same time of day, so there is some error in the effective diurnal bolometric temperature that has not been accounted for and could account for the difference in CMAs derived from each instrument. I ran KRC at the ROI for L_s = 150, 210, and 255° to estimate the errors in the diurnal curves during early, mid, and late spring. Figure 13 illustrates the assumed diurnal temperature curves of TES and THEMIS to those predicted by KRC. The diurnal temperature variation in early spring is much less than 1%, so the poor resemblance of TES and THEMIS to the KRC models has little bearing on the errors of the diurnally averaged temperature. In mid and late spring the diurnal variation in temperature is much larger and while TES remains a poor fit to the models, THEMIS times of observation closely resem-ble the true amplitude of the diurnal curve as predicted by KRC, especially in late spring. Nonetheless, the error in the effective diurnal temperature used to compute the CMA (integrated T^4) is less than 0.05 K even in the worst case (early spring). This is much less than the ≈ 25 K combined error from the instrument observations and blackbody fit (Figure 6). Therefore, the time of day cannot account for the difference in the CMA between TES and THEMIS observations.

The difference between TES and THEMIS could then be attributed to either spatial resolution and sub-pixel mixing, or a phyiscal difference between ices in the

39
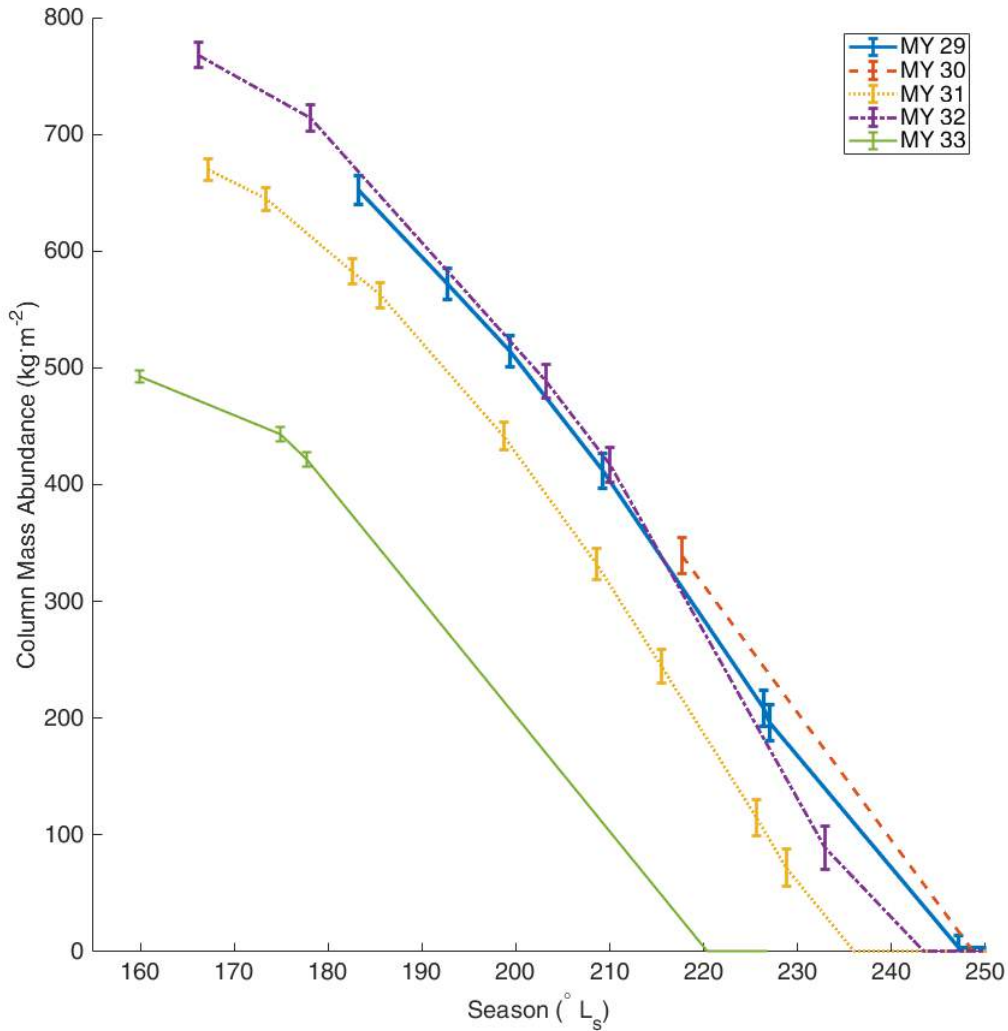
Figure 12. Regional THEMIS/HiRISE CMA for Individual Mars Years

The variable CROCUS dates have profound impacts on the seasonal CMA in each year, except in MY 29 and 32. MY 29 and 32 appear to be most similar, though their CROCUS dates differ markedly. MY 29 and 31 have different CMAs throughout the entirety of spring, though their sublimation patterns are nearly identical.

40

years observations were collected. TES operated from MY 24 -27, while THEMIS data at the ROI are taken primarily from MYs 32 and 33 and HiRISE data, from MYs 29 - 33. MYs 24 - 26 were, generally, less dust-storm-active than MYs 29 - 31 during the depositional season in the south on the regional scale (Battalio and Wang, 2019). However, there were no global scale dust storms after MY 25, which had a global scale dust storm beginning in mid spring (Battalio and Wang, 2019).

For the interannual differences, the temperatures are derived from THEMIS data in MY 26, 32, and 33, regardless of year because the THEMIS data set lacked good temporal resolution to conduct this study otherwise. This means the variations in CMA are from the derived albedo in HiRISE frames from the five different Mars years only, not from variations annually in the THEMIS data. Therefore, any differences in CMA are solely from albedo variations. There were no global scale dust storms between MY 29 and 33, however, the southern hemisphere did experience slightly higher dust storm activity during the southern winter, when seasonal ice would be deposited (Battalio and Wang, 2019). Dust masks the seasonal ice spectrum when above about the 1%dust level (Hansen, 1999) in CO_2 ice. For slab ice (large path length), this dust contamination would *brighten* the ice, thereby reducing the net absorption of incident radiation and reducing the CMA. Therefore, it is very plausible that the interannual variations observed are due to heightened dust content of the ice caused by a more active dust season. There is also a possibility that dust or water ice aerosols during the polar night caused more atmospheric deposition to occur. These fine-grained atmospheric deposits could lead to an increase in albedo, if a higher proportion of the ice in MY 29 were granular CO_2. Ultimately, the marked difference in the MY 29 is likely due to *regional-scale* dust activity in the southern hemisphere in that year. It is possible that there is merely more dust in the atmosphere
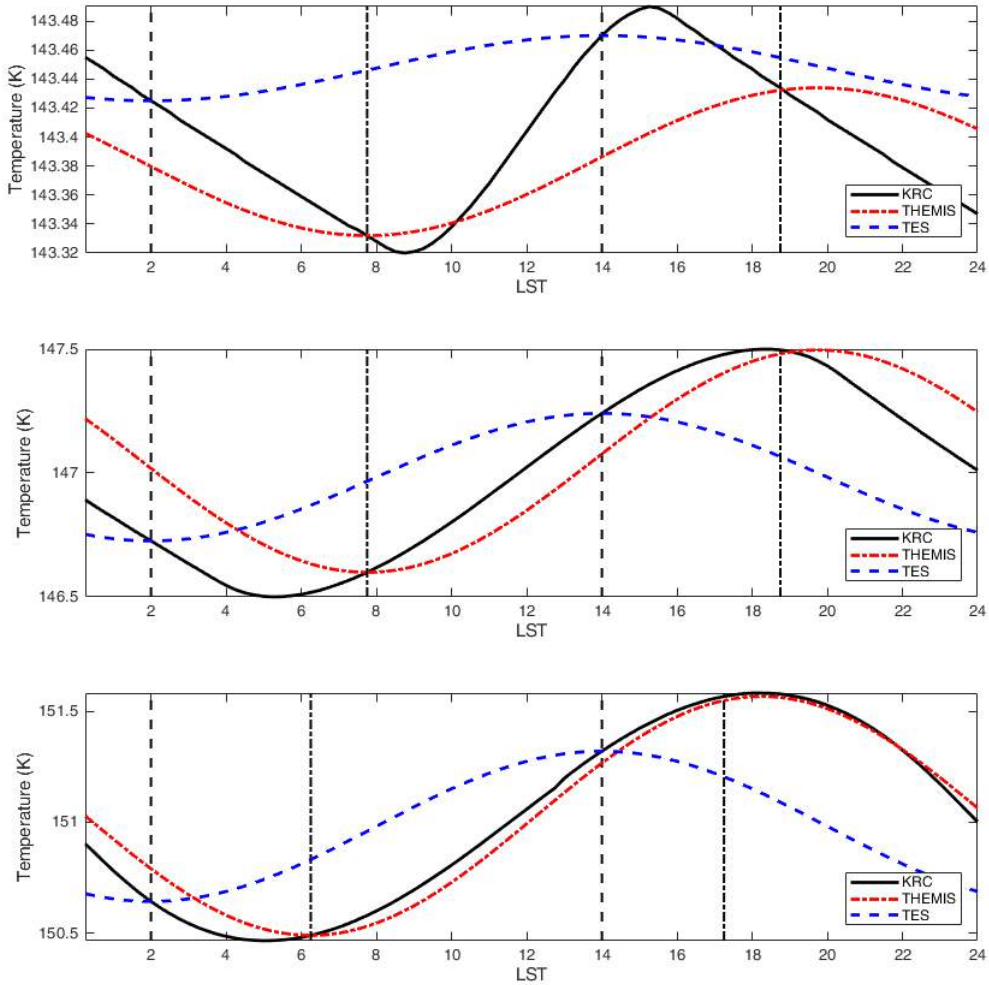
Figure 13. Diurnal Temperature Curves Derived from KRC

Temperature vs. Local Solar Time for $L_s = 150°$ (top), 210° (middle), and 255° (bottom). The vertical lines indicate the time of day in which TES (dashed) and THEMIS (dot-dashed) observations were approximately taken at each L_s. Here, the amplitude is computed using the KRC values at the LST of the instrument observations.

causing a higher-than-average albedo in the MY 29 HiRISE data, but no hazes are apparent and there appear to be no radical spatial variations in albedo that would be associated with the strong forward scattering of aerosols at high polar incidence angles (Appéré *et al.*, 2011) in the data.

There are currently no studies that cover the dust record in MY 32 and 33. What causes MY 33, in particular, to be so different from the other 4 MYs is unknown. Despite the drastic difference in CMA between years, spatial variations in the sublimation pattern are nearly identical in HiRISE images in MY 29 and MY 31, suggesting that surface properties might be far more important for the sublimation pattern of the ice than the actual content (if its dust laden, high density, porous etc.). Figure 14 shows the same small scale features near the center of the ROI at the same season. The sublimation patters are almost indistinguishable. If dust is contributing to the sublimation of seasonal ice, there is little evidence of it here.

2.4.3 Density

Density is obtained by dividing the five Mars Year composite CMA by the depth estimated in MY 29. Derived densities for this depth curve, assuming it as a regional average, are presented in Figure 15. The early spring densities suggest a porosity of $\approx 70\%$. This is likely due to the high degree of error in the depth measurement, but even at the lower limit the initial porosity is $\approx 60\%$. The low albedo in early spring, as well as the clear visibility of the underlying surface morphology suggest this ice is deposited directly (Mount and Titus, 2015; Hecht, 2008). If this is slab, then it is highly porous. The ice densifies over time, reaching nearly $1000\,\mathrm{kg\,m^{-3}}$ at $L_s \approx 209°$.
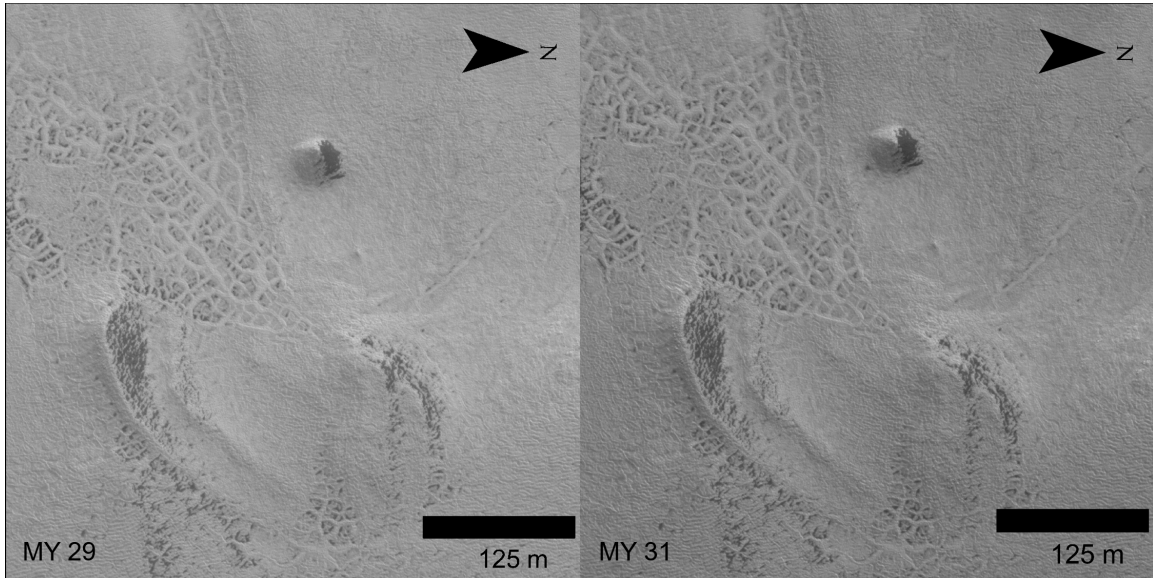
Figure 14. Interannual Comparison of Small-scale Sublimation Patterns

Small scale features in HiRISE images from MY 29 (left) and MY 31 (right) at $L_s \approx 226°$. The predicted CROCUS dates, and column densities for these years are markedly different, yet the spatial variations in the sublimation pattern that occur are nearly identical, even down to the 10s of meters scale.

This corresponds to a porosity of $\approx$ 40%, though the large degree of uncertainty in late spring means nothing conclusive can be drawn from this analysis. Still, this deposit is consistent with the annealing-fracturing process of porous slab and snow suggested by Mount and Titus (2015).

The error on the depths in this ROI inspire little confidence (Figure 10). I can put limits on the depth by assuming a regionally constant density, then dividing it through the CMA. This is shown in Figure 16 assuming a pristine slab at 1600 kg·m^{-3} for the upper density limit and a porous slab at 416 kg·m^{-3} for the lower limit. The shape of the depth curves constrained from CMA and assumed constant density is concave, unlike the boulder shadow estimated depth curve, which is convex. The THEMIS/HiRISE indicate that ice depths in the region could fall anywhere between
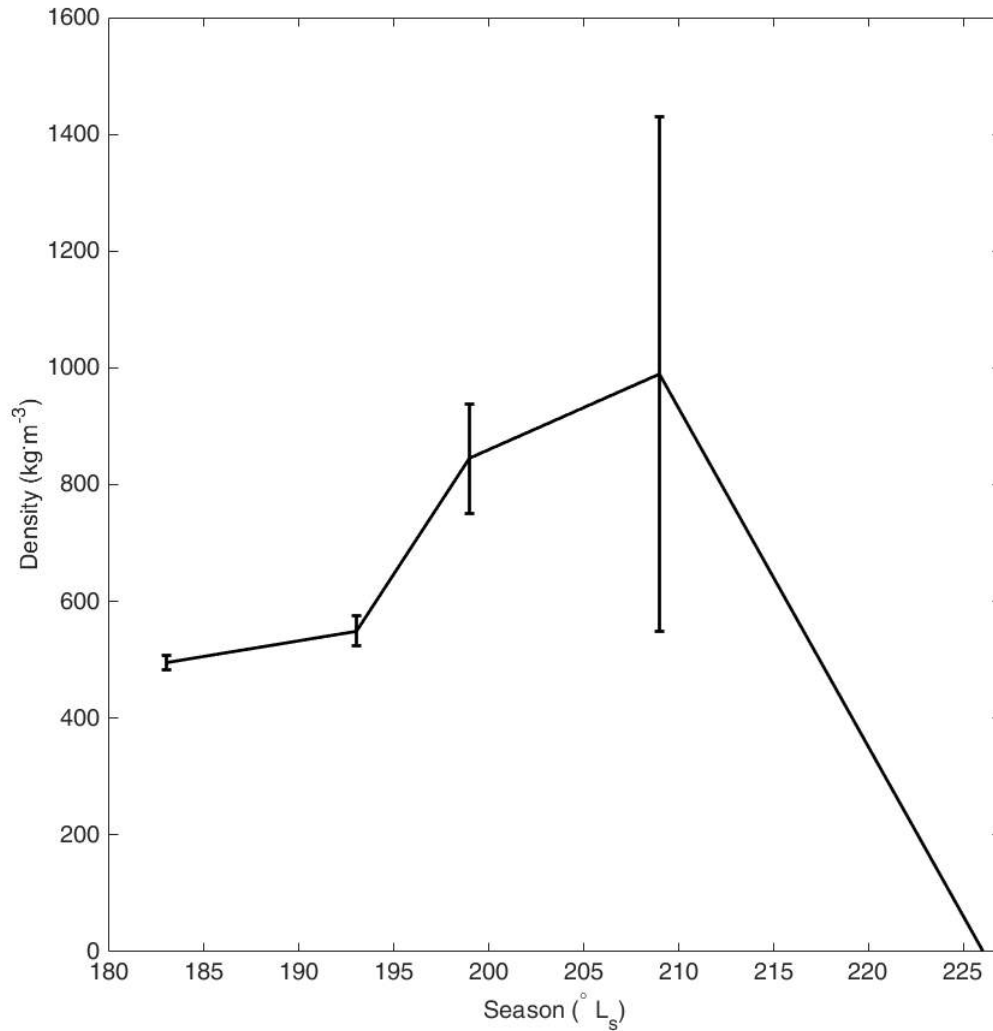
Figure 15. Estimated Regional Bulk Density

Estimated from the 5 year regional average CMA divided by the ice depth measured in MY 29. The densities are low despite the ice morphology and albedo suggesting slab ice in the ROI. Evolution of the density is consistent with the fracturing-annealing process for porous slab described in Mount and Titus (2015).
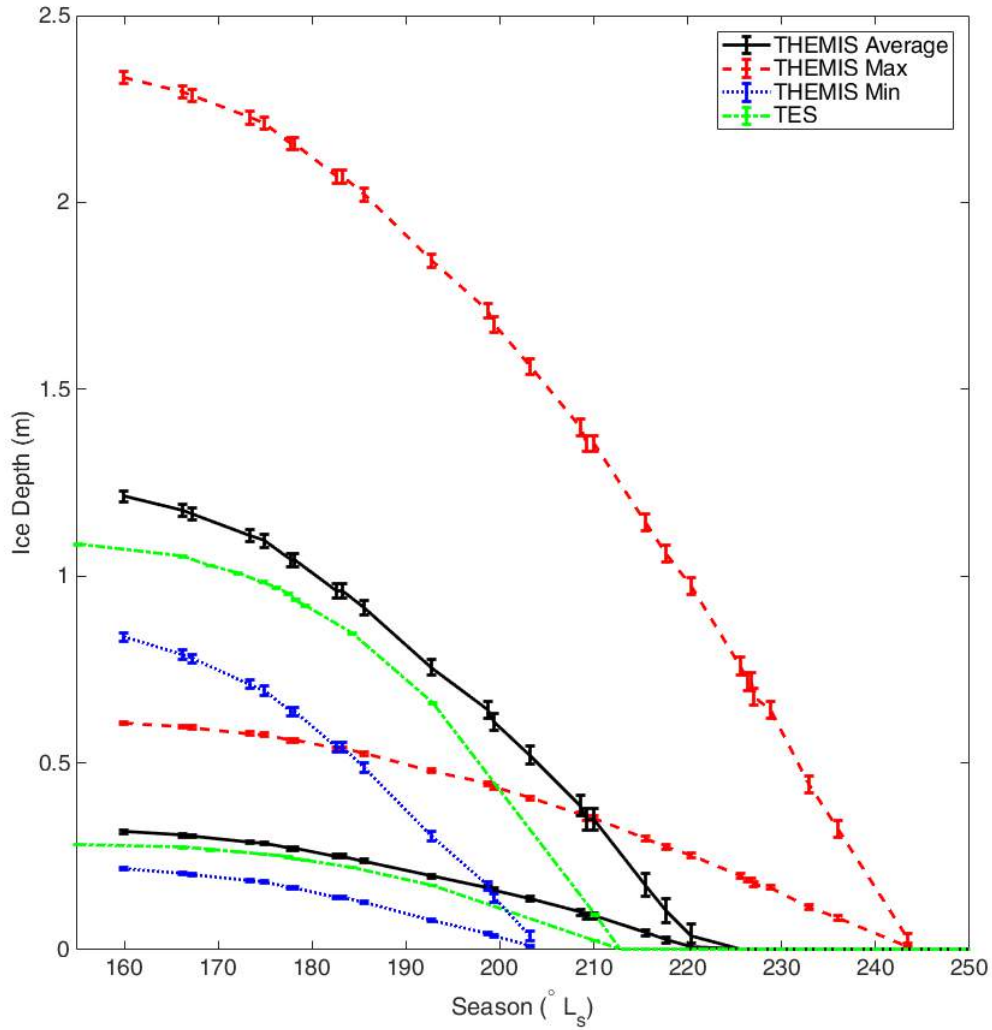
Figure 16. Depth of Ice Assuming Constant Regional Density

The lower curves are assuming a constant density of pure slab at 1600 kg·m^{-3}. The upper curves are assuming the density of a slab with a 74% porosity (416 kg·m^{-3}). These extrema bracket the regional ice depth.

0.2 and 2.5 m. While the upper end of this is unrealistic, the values do bracket the boulder shadow estimated ice depths from MY 29 (Figure 10). Though, from these curves, we see the local ice depth can vary quite dramatically with CROCUS date. The maximum CMA from THEMIS is a good estimate for the material located on the south-facing gully, while the min is indicative of the early-CROCUS, scarps. Clearly, local values are important as this estimate suggests that differences in depth over the sublimation season can be on the order of 2 - 10 times depending on the precise location.

2.5   Conclusion

Local CMAs can vary from $400 - 1000$ kg·m^{-2}, with the extrema occurring simultaneously in early spring. These variations may be explained by ice depth variations of up to 2 m, porosity variations of 75%, or a combination of these. These local variations appear to be geographically correlated, where south-facing scarps maintain seasonal ice longer into spring than north-facing slopes. Thermal inertia of the frost-free surface appears to have a secondary effect, with high thermal inertias reducing CMA and forcing CROCUS dates to be earlier than lower thermal inertia units. These results suggest that the state of ice is far more complex than globally averaged and regionally averaged studies can identify. It is clear a full understanding of surface property and ice evolution is necessary in order to decipher spring time sublimation behavior, because it is not entirely clear what forces albedo and temperature changes over time. Interannual CROCUS date disparity appears to be correlate with southern hemisphere dust activity, but interannual observations of the ROI do not indicate radically different sublimation patterns despite variable CMA, CROCUS, and albedo.

This ROI was sufficiently complex to warrant further highly detailed investigations at other seasonal polar cap regions with comparable data volume. In fact, it may be the only viable way to fully characterize the seasonal polar caps.

Chapter 3

SURFACE CONTROLLED SUBLIMATION PATTERNS IN SOUTH POLAR

GULLIES

3.1 Introduction

The seasonal retreat of the polar caps has been well documented in both the visible (James *et al.*, 2000, 2001; Calvin *et al.*, 2015, 2017), near infrared (Brown *et al.*, 2010, 2014; Bibring *et al.*, 2005; Appéré *et al.*, 2011), and thermal infrared (Kieffer *et al.*, 2000; Kieffer and Titus, 2001; Titus *et al.*, 2001; Piqueux *et al.*, 2015). The sublimation patterns of seasonally deposited ice during retreat have been extensively and thoroughly studied on both the north and south cap. Kieffer *et al.* (2000) identified large-scale regions of low and high albedo on the South Polar Seasonal Cap (SPSC), deemed the Cryptic and Anti-cryptic (or Bright) regions, respectively. These regions appear in mid-spring around $L_s \approx 220°$. They remain at the CO_2 frost temperature and have no discernible difference in mass accumulation. To this day, it is uncertain as to the cause of these regions.

High resolution imagery has revealed a plethora of intriguing brightness features such as dust fans (Kieffer *et al.*, 2006; Hansen *et al.*, 2010; Thomas *et al.*, 2010), dark spots (Kieffer *et al.*, 2006; Piqueux and Christensen, 2008; Thomas *et al.*, 2010), polygonal cracks (Portyankina *et al.*, 2012), long lived bright depressions (Cull *et al.*, 2010; Mount and Titus, 2015; Kossacki and Markiewicz, 2002), and other geographically dependent albedo variations. Despite having these excellent observations and characterization of properties of the ice, it is still unclear what processes cause surface

frosts to evolve over sublimation in the manners observed. Water ice is known to contaminate seasonal deposits (Langevin *et al.*, 2007; Brown *et al.*, 2010) and can dramatically increase the albedo of CO_2, even in relatively small (<10%) abundances (Warren *et al.*, 1990) or if a few monolayers of water ice on the order of 10 μm in grain size overlies CO_2 deposits. Dust contamination can also modify the visible albedo of seasonal ice. With a mass fraction only 1%, dust can completely mask the spectrum of CO_2 ice (Hansen, 1999; Warren *et al.*, 1990).

It is thought that grain-growth occurs through annealing (Eluszkiewicz, 1993; Eluszkiewicz *et al.*, 2005) and ice self-cleans dust grains when illuminated (Kieffer *et al.*, 2000, 2006). However, ice can exhibit remarkable differences in brightness at small spatial scales where ice-grain sizes and insolation should be relatively uniform. If these effects are responsible for the observed sublimation patterns, what forces seasonal ice to undergo these processes differentially? Are these solely responsible for ice evolution? The answers may lie in the thermal and geometrical properties of the regolith beneath the seasonal ice.

Thermal inertia is the measure of the degree to which materials change temperature with increasing energy input. Piqueux *et al.* (2016) showed low-thermal inertia units at low latitudes undergo diurnal CO_2 frost deposition. Perhaps the affects of thermal inertia are also important for seasonally deposited material (Haberle *et al.*, 2004, 2008). Analysis of springtime sublimation patterns of seasonal ice may provide insight into the relation between surface and depositional processes as well as the way those surfaces affect the temporal evolution of the deposits.

Here, we implement a simple correlation analysis on the frost-free surface properties to the springtime evolution of ice in south polar gullies.

3.2 Data

The Region of Interest (ROI) is a gully system located at 68°S, 1.3°E inside a polar pit in a ≈ 50 km crater. High Resolution Imaging Science Experiment (HiRISE) images of the region are detailed in Chapter 2.1 (see Table 1) and are used for computing the seasonal albedo of the surface.

Thermal Emission Imaging System (THEMIS) provided thermal data on the frost-free surface, which was converted to thermal inertia using the method of Fergason *et al.* (2006). The RDR used for this product was taken at $L_s \approx 350°$ (late summer), ensuring warm temperatures and little chance for the presence of surface frost. These data is shown in Figure 17. following the convention of Putzig and Mellon (2007) the SI units for thermal inertia ($J \cdot m^{-2} \cdot K^{-1} \cdot s^{-1/2}$) are labeled as Thermal Inertia Unit (TIU). Thermal inertias are highest along the scarp edges, exceeding 500 TIU. These thermal inertias are because there are boulders in the mouths of the gullies, which likely increase the thermal inertia of the surface (A). Thermal inertias are moderately high in the north of the ROI on the east-facing scarp and in the south on the north facing slope (B). There is one anomalous high thermal inertia unit ($\approx 400 - 500$ TIU) on the north-facing slope (C). Figure 19 highlights A and C in late spring at high resolution.

At polar temperatures THEMIS signal-to-noise is relatively low (Christensen *et al.*, 2004). A one dimensional thermal model called KRC (Kieffer, 2013) was run for the range of thermal inertias observed in the THEMIS thermal inertia data product used here, in order to ascertain the errors associated with data product. This returned surface temperatures as a function of thermal inertia. A polynomial fit was done to the data. Using the fit and assuming a 4 K instrument error, the temperature
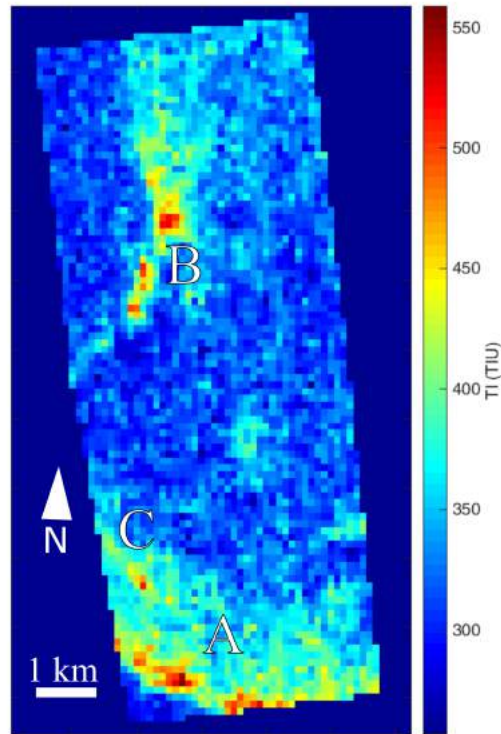
Figure 17. THEMIS Derived Thermal Inertia

Thermal Inertia map derived from the method of Fergason *et al.* (2006) on THEMIS data product I26304014. Image is taken at $L_s \approx 250°$ ensuring no ice is present. A) North facing gullies with moderately high thermal inertia. The top of the scarp has very high thermal inertia due to the presence of boulders. B) East facing scarp. Gully mouths have high inertias also due to boulders. C) Anomalous high inertia unit. This rock layer appears to be "blockier" than surrounding units.
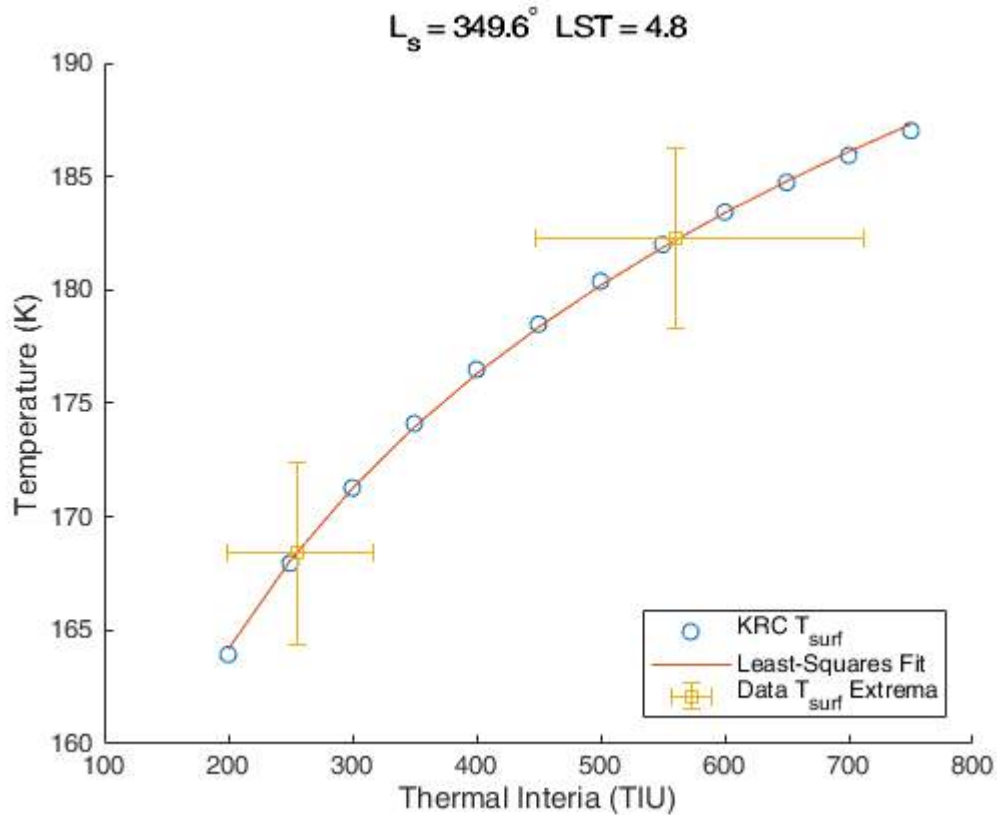
Figure 18. KRC-derived Thermal Inertia vs. Temperature

Polynomial fit was to 6th order merely to interpolate between KRC derived data. The extrema were used to approximate errors associated with the THEMIS instrument temperature error. Errors are $\approx 20 - 25\%$ assuming a 4 K temperature error.

associated with the maximum and minimum thermal inertia from the data product allowed for error bars to be plotted for the thermal inertia. The error on the thermal inertia of the extrema is between ≈ 20 and 25% (Figure 18).

For surface geometry, slope and aspect were computed from an High Resolution Stereo Camera (HRSC) Digital Terrain Model (DTM) using the Integrated Software for Imagers and Spectrometers (ISIS). The cosine of the aspect was used to address
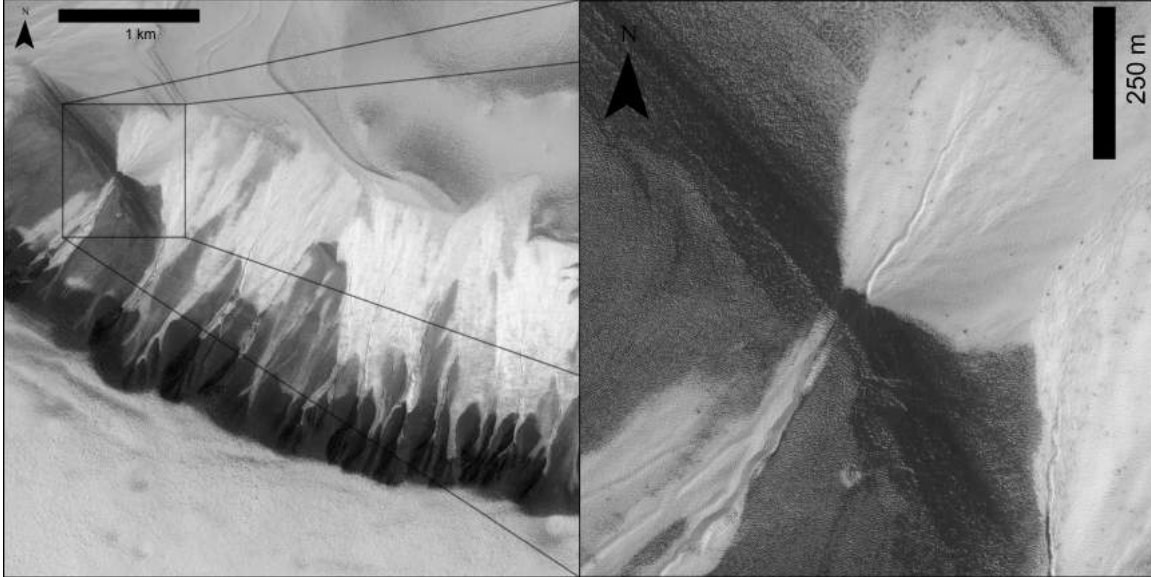
Figure 19. High Resolution Imagery of High Thermal Inertia Features

HiRISE images taken at $L_s \approx 226°$ in Mars Year 29. (Left) Zone A from Figure 17. Gullies appear brighter and smoother than the rest of the slope and the dark scarp has identifiable boulders and bedrock. (Right) Zone C from Figure 17. In late spring this high albedo feature is much darker than its surrounding material. It is also much coarser, the layering appearing to be made up of blocks, whereas the gully fans and slope material are hummocky with smoother texture.

the issue of its cyclical nature (i.e, $0° = 360°$). This defines north aspect at 1 and south aspect at -1, but has the disadvantage of non-unique values for east and west. For illumination purposes, north and south are more important due to the sun crossing the northern sky in the southern hemisphere during spring.

Another data product was generated from the slope and cosine of the aspect, which I call a the aspect magnitude. This is defined as

$$\Theta = \theta \cos \phi \tag{3.1}$$

where θ is the slope in degrees and ϕ is the aspect. As the name suggests, this gives an indication of how strongly a slope faces a direction, with steeper slopes having
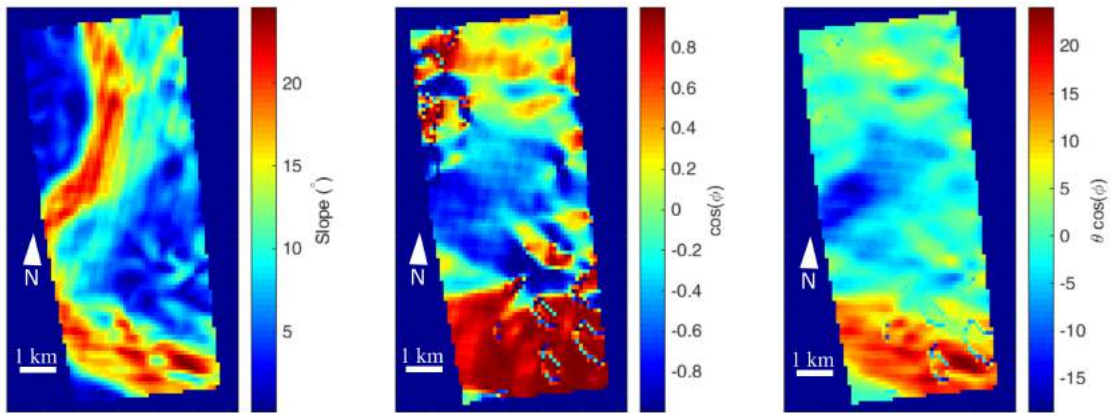
Figure 20. Surface Geometry Data Products

(Left) Slope. The highest slopes occur on the scarps surround the pit. The bottom of the pit is relatively flat, as are the plains at the top of the scarp. (Middle) Cosine of the aspect. The scarp at the south of the image is primarily north-facing. The center of the ROI is mostly south facing. Discontinuities occur where changes in slope are dramatic. (Right) Aspect Magnitude. Composite of the slope and aspect maps.

higher magnitudes, positive values having more northerly aspects, and negative values having more southerly aspects. These data are presented in Figure 20.

All data products were map projected to a polar stereographic projection and the pixels were spatially convolved using nearest neighbor interpolation. The resolutions of the HiRISE and HRSC data products were degraded to THEMIS resolution (100 m/pix) so as to have 1:1 pixel ratios between all products.

3.3 Methods

Values from the data products are plotted against the slope-corrected albedo in corresponding pixels in each HiRISE frame. These data are then explored for correlative trends, sub-populations, and variations from the mean.

Correlation coefficients are computed over time for each sample and p-values are assessed for significance of the correlation, if any. The correlation coefficient is defined as

$$\rho(A, x) = \frac{1}{N-1} \sum_{i=1}^{N} \left(\frac{A_i - \langle A \rangle}{\sigma_A} \right) \left(\frac{x_i - \langle x \rangle}{\sigma_x} \right) \tag{3.2}$$

where A is the albedo, x is the thermal inertia, slope, aspect, or aspect magnitude, and σ is the standard deviation. The p-values are computed by MATLAB. This is done by generating a test statistic and performing a sophisticated t-test to determine the probability of the data being uncorrelated (see MATLAB documentation for corrcoef function).

The thermal inertia and the aspect magnitude were inspected and found to be weakly correlated (Figure 21). A linear least-squares fit was done to these data and residuals were subtracted, resulting in uncorrelated independent variables.

3.4 Results

The scatter plots for albedo and thermal inertia for each HiRISE frame are detailed in Figure 22. The coloration indicates the aspect magnitude. The higher the aspect magnitude (north facing, high slope) the redder the points are, and the lower the aspect magnitude the bluer. There appear to be three different populations useful for describing the data, defined at $L_s \approx 160°$. These populations were not statistically
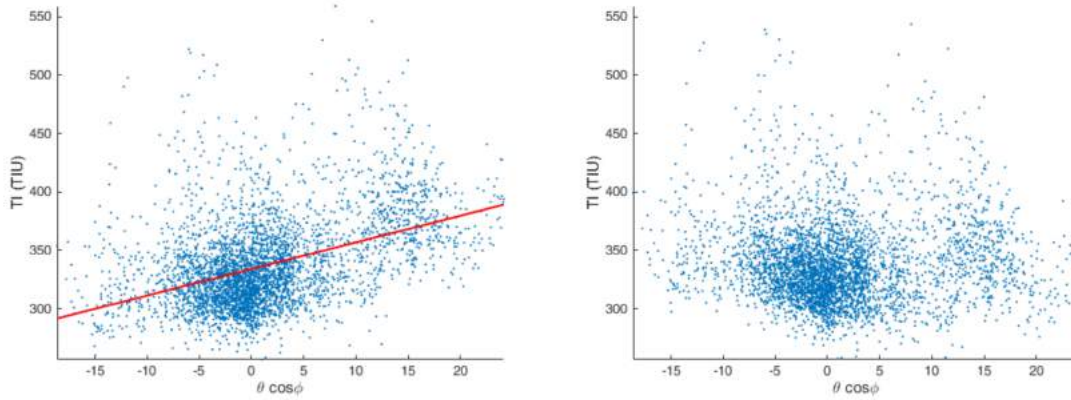
Figure 21. Thermal Inertia and Aspect Magnitude Correlation Correction

(Left) Linear best fit line is shown, indicating a correlation between the data that could skew results. (Right) Residuals are taken and removed from thermal inertia. The axis are inverted and aspect magnitude is corrected the same way independently.

verified, but are merely qualitatively useful for describing the changes in the data over time. Population 1 is a set of low-to-moderate thermal inertia material between 300 and 400 TIU with albedos less than 0.20. This population has high aspect magnitudes ($> 15°$). Population 2 is a set of low aspect magnitudes ($\approx -10 to -15°$) that span the full range of thermal inertias (250 - 550 TIU) and have albedo values of approximately the mean of 0.20. Population 3 is composed of low-to-moderate thermal inertia between 300 and 400 TIU with higher-than-average albedos of ≈ 0.25. The aspect magnitudes of this population range from moderate to high ($10 - 15°$).

The average albedo increases slightly from $L_s \approx 160 - 178°$ from 0.20 to 0.21. Population 1 changes little, with some points shifting to higher albedo while others remain low albedo as the regional albedo increases. Populations 2 and 3 remain relatively unchanged, though do increase with the mean albedo. From $L_s \approx 178 - 193°$ the mean albedo oscillates between 0.2 and 0.35, but ultimately increases. Population 1 point density reduces over this time as albedos increase. Population 2 begins to

diverge from the average, but maintains its flat slope. Population 3 albedo values begin to take on a wider range of values than in late winter up to 0.35.

Between $L_s \approx 193$ and $210°$ Population 1 vanishes as it merges with Populations 2 and 3. Population 2 experiences a minimal increase in albedo and develops a very slight negative slope, but the high aspect magnitude points in Populations 1 and 3 increase in albedo dramatically, thereby increasing the average albedo. By $L_s \approx 199°$ it is apparent that low-to-moderate thermal inertia surfaces generally have higher albedos. This trend continues until $L_s \approx 233°$.

After $L_s \approx 210°$ average albedo begins to decline until $L_s \approx 243°$, with the exception of an albedo spike at $L_s \approx 277°$. Population 1 reappears at $L_s \approx 215°$ a the point density increases as Population 3 begins to deteriorate. All Population 3 high aspect magnitude points have completely merged with Population 1 by $L_s \approx 233°$. Population 2 maintains its slight negative trend until $L_s \approx 226°$ after which this population slowly re-converges on the average albedo until $L_s \approx 243°$. After this time, the average albedo remains stagnant and all Populations converge.

From $L_s \approx 232 - 243°$ the low-to-moderate thermal inertia units that have low-to-moderate aspect magnitudes are the only above-average albedos. Low-to-moderate aspect magnitudes with high thermal inertias generally have lower-than-average albedo.

There are three populations in the albedo vs. slope scatter plot, as well (Figure 23). Again, three separate populations are defined in late winter that will be used for describing trends as sublimation occurs. Population 1 is an envelope of low thermal inertia material between slopes of 0 and 10°. Population 2 is a group of low thermal inertia points that span the full range of slopes with an albedo of approximately the

58

Figure 22. Albedo vs. Thermal Inertia over Spring

Coloration is aspect magnitude for reference, with reds being higher and blues lower. The dashed line is the mean for that L_s.

average, but with a slight negative trend. Population 3 is a set of moderate thermal inertia between slopes of 10 - 20°.

Population 1 merges with Population 2 by $L_s \approx 199°$, which maintains its slight negative trend about the average during this time. Population 3 shifts to higher-that-average albedos. Population 1 never re-emerges and the strength of the negative trend of Population 2 reduces for the rest of spring, eventually flattening out and converging on the average by $L_s \approx 243°$. The same is true of Population 3, becoming indistinguishable from Population 2 by $L_s \approx 220°$.

The envelope created by Population 1 is likely an artifact tied to the aspect, because Population 2 values in the same slope range and thermal inertia do not follow this trend. Population 3 is likely a thermal inertia related group as all the points in this set are of moderate-to-high thermal inertia. Thus, it is important to combine this slope data with the aspect to form the aspect magnitude in order to gain a clear understanding of the relationships presented.

The albedo vs. aspect scatter plots are peculiar and shown in Figure 24. There are two populations here, but Population 1 spans all aspects, is centered on the average albedo, and is nearly perfectly flat. Population 2 is a set of points at aspects between 0.8 and 1.0 (exactly north-facing). This would produce false correlation coefficients because the weighting that Population 2 places on a more-or-less uncorrelated fit. The trends throughout spring are essentially the same as initial, with variations in the deviation from the mean. The information provided by these plots appears to be incomplete. Combining this data with the slope to produce the aspect magnitude reveals a more complete picture.

There are only two populations in the albedo vs. aspect magnitude scatter plots (Figure 25). Again, I define these populations in early spring. They will be used for
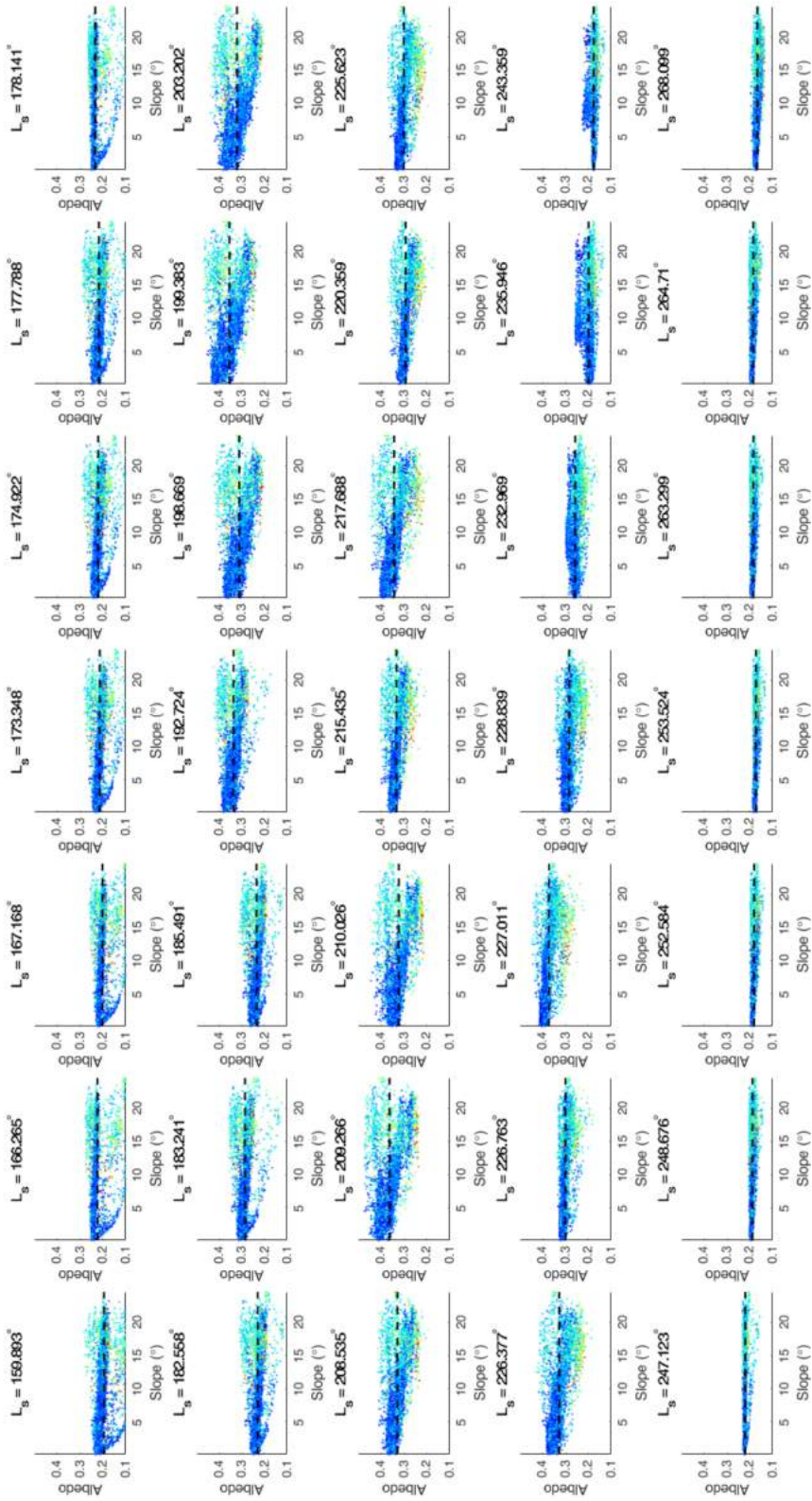
Figure 23. Albedo *vs.* Slope over Spring

Coloration is thermal inertia for reference, with reds being higher and blues lower. The dashed line is the mean for that L_s.
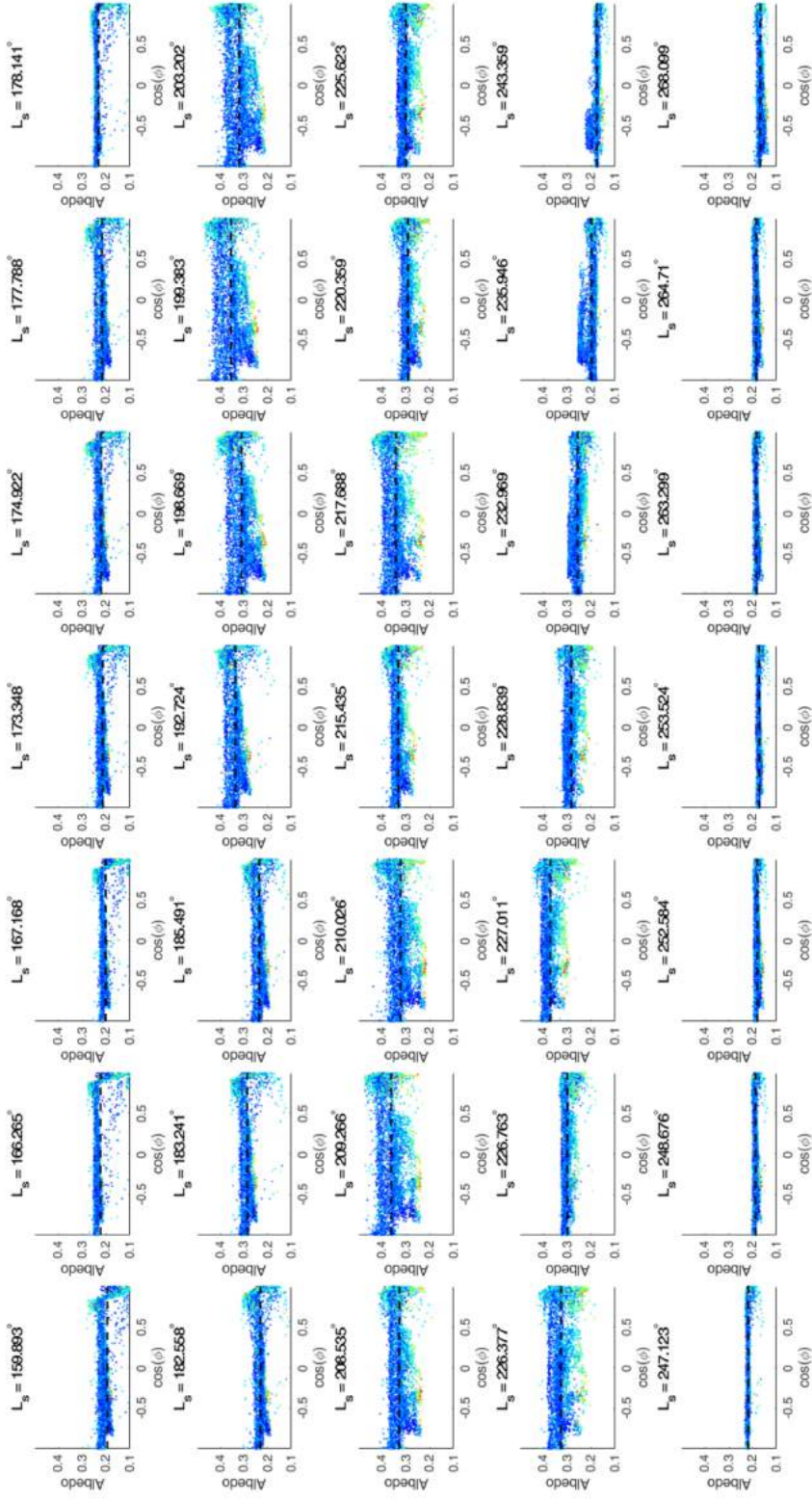
Figure 24. Albedo vs. Aspect over Spring

Coloration is thermal inertia for reference, with reds being higher and blues lower. The dashed line is the mean for that L_s.

62

describing temporal trends. Population 1 is the set of values above aspect magnitude 0 that are below the average albedo and have moderately high thermal inertias. Population 2 is the group of points that spans all aspect magnitudes centered on the average albedo with a slight positive trend.

The albedo of Population 1 increases from $L_s \approx 160-199°$, with lower aspect magnitude points in this group lagging behind their north-trending counterparts. Population 2 remains mostly unchanged during this time, only increasing very slightly with increase in average albedo.

By $L_s \approx 199°$, the positive trend is very strong, with Population 1 and 2 merging to form a continuous, indiscernible group of points. Low aspect magnitude (south-facing) slopes tend to have higher thermal inertias and remain at significantly lower albedo than other points in both populations. The data maintain this shape until $L_s \approx 210°$, with the exception of an anomalous convergence of points toward the mean at $L_s \approx 178°$.

After $L_s \approx 210°$ Population 1 albedos begin to fall reaching approximately mean values by $L_s \approx 236°$. Population 2 likewise converges toward the mean during this time. At $L_s \approx 236°$ the Populations 1 and 2 have merged except for low thermal inertia units between aspect magnitude of 0 and -15°. All trends vanish after $L_s \approx 247°$.

Correlation coefficients and associated p-values are depicted in Figure 26 as a function of time. P-values for both thermal inertia and aspect magnitude are exceedingly small. This indicates that the correlations are indeed significant. Only where the correlation coefficients approach 0, do p-values exceed 10^{-4}, which is consistent with an uncorrelated sample. That is, the p-value must be large for an uncorrelated sample by definition.
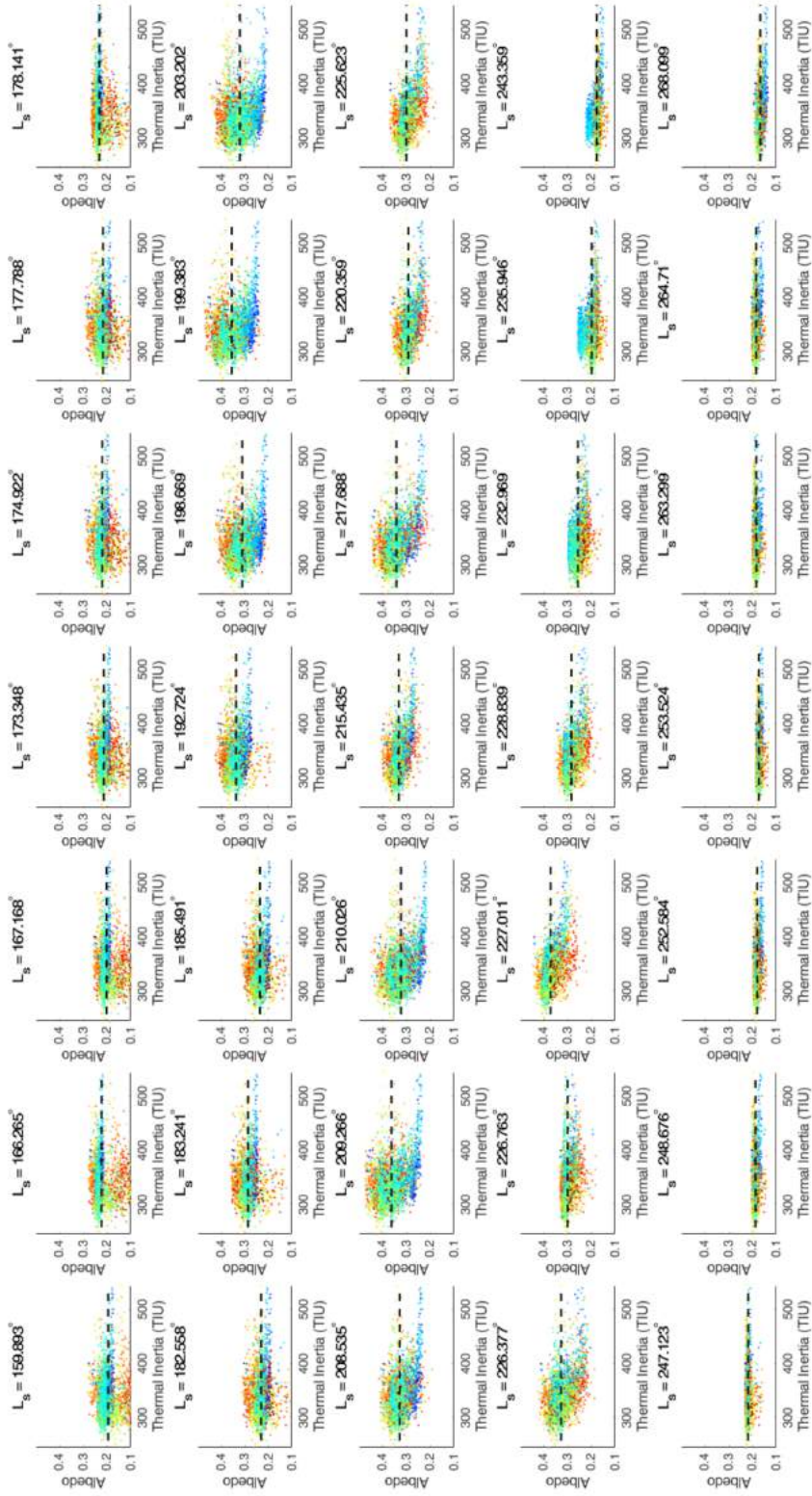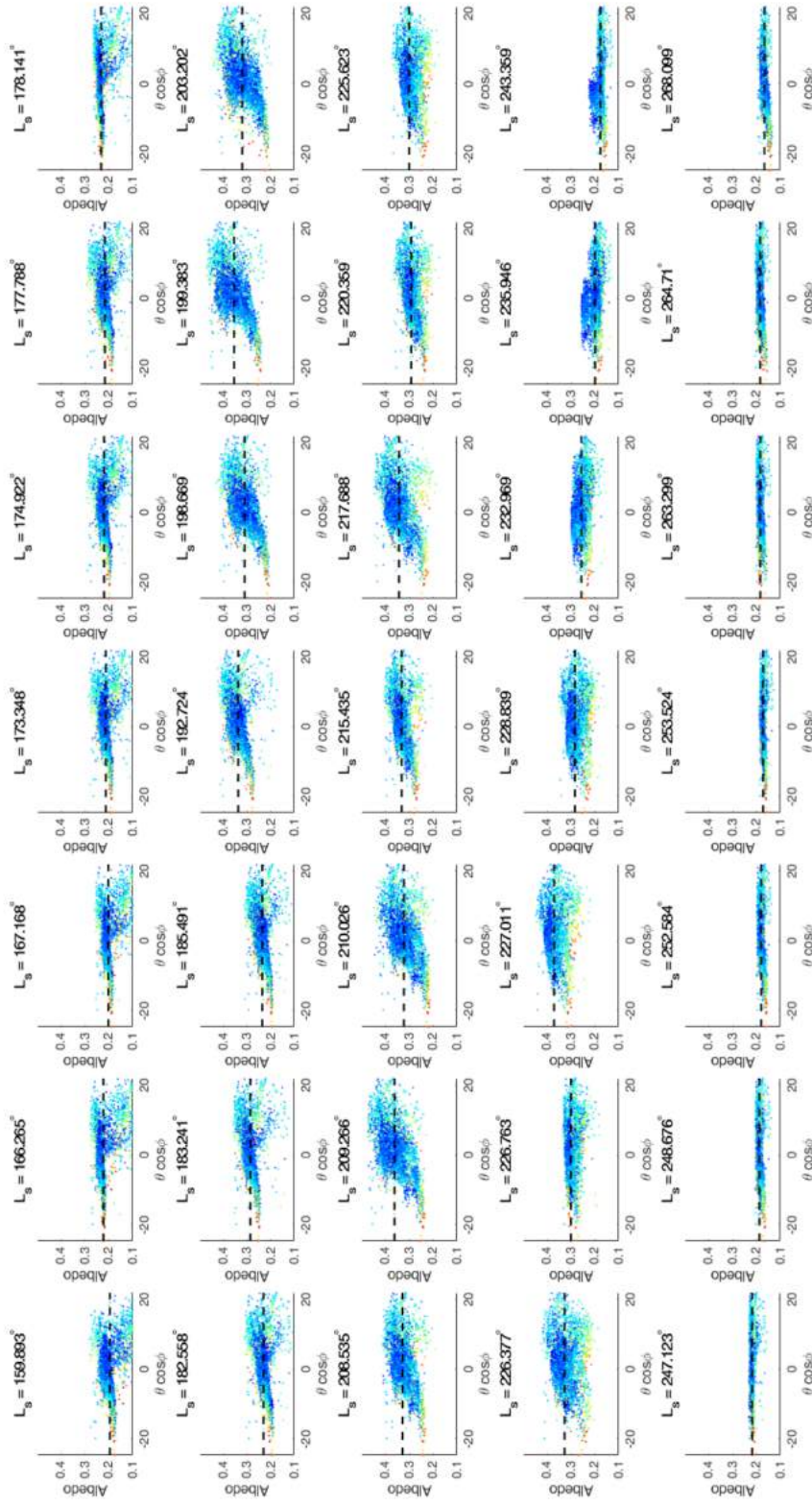
Figure 25. Albedo vs. Aspect Magnitude over Spring

Coloration is thermal inertia for reference, with reds being higher and blues lower. The dashed line is the mean for that L_s.
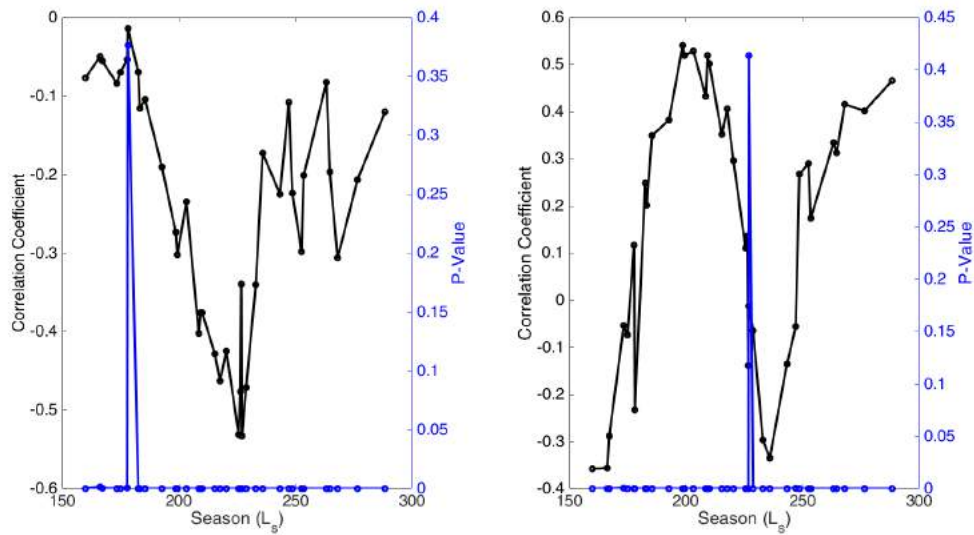
Figure 26. Correlation Coefficients over Springtime Sublimation

(Left) Correlation coefficient and p-value for albedo and thermal inertia. (Right) Correlation coefficient and p-value for albedo and aspect magnitude.

Correlation coefficients between the albedo and thermal inertia are always negative throughout spring. In early spring, the correlations are weak, but significant. After $L_s \approx 178°$ the negative correlation strengthens reaching a minimum at $L_s \approx 227°$. Just before the minimum is an anomalous peak in the correlation coefficient corresponding to the albedo anomaly at $L_s \approx 227°$. After reaching the minimum the correlation weakens until $L_s \approx 236°$. The correlation remains negative for the remainder of spring but oscillates as the season progress into summer.

The albedo and aspect magnitude correlation coefficient is negative at the onset of spring but increases over time. By $L_s \approx 199°$ the correlation coefficient reaches its maximum, earlier than the thermal inertia correlation reaching minimum. The trend reverses direction until $L_s \approx 236°$, where the correlation reaches a minimum. As the season progresses the correlation again increases into summer.

65

3.5   Discussion

There are 5 major points that deserve attention:

- Extremely low albedo on north-facing slopes in early spring.
- Increase of albedo on north-facing slopes ending in a maximum positive correlation between albedo and aspect magnitude at $L_s \approx 199°$.
- Increase of albedo on low-to-moderate thermal inertia units ending in a maximum negative correlation between albedo and thermal inertia at $L_s \approx 227°$.
- Decrease of albedo on north-facing slopes ending in a maximum negative correlation between albedo and aspect magnitude at $L_s \approx 236°$.
- Regional albedo increase followed by decrease over spring.

3.5.1   Extremely Low Albedo on North-facing Slopes in Late Winter

The group of low albedo ice on north-facing slopes is responsible for the relatively strong negative correlation between albedo and aspect magnitude in late winter, but it is difficult to ascertain how CO_2 frost could be this dark. The albedos range between 0.05 and 0.1, which is darker than even the frost-free surface and much darker than one would expect for dust-laden ice. Dust-rich deposits tend to have albedos in the range of 0.20 - 0.40 in HiRISE wavelengths, depending on the dust content in the ice, as well as the grain-size/porosity of the ice (Mount and Titus, 2015). Dust masks the CO_2 spectrum when above 1% concentration, thus if the ROI deposits were dust-laden in late winter, albedos should be on the order of what one would expect for dust. If dust were responsible for the low late winter albedo in the ROI, then the dust would be required to have albedos between 0.05 and 0.1. This is highly

unlikely as the grain-size of dust particles in ice is less than 50 μm (Pollack *et al.*, 1990, 1993). Particles of this size cannot account for such low albedos unless they are sourced from a very specific unit that has intrinsically low albedo (e.g., some black ash deposit). This is highly unlikely, as there is always some amount of dust in the Mars atmosphere and it tends to spread rapidly once airborne (Battalio and Wang, 2019). Also, dust-rich ice deposits would likely be uniform in dust concentration across the region. Therefore, the negative correlation in late winter could only be explained by dust if it were self-cleaned from the ice where directly illuminated. Dust on north-facing slopes likely heats up more rapidly than other slope faces. Thus, dust could burrow into the ice earlier in sublimation, though it is unclear whether this process could initiate so rapidly just after polar night ends. Kieffer (2007) suggests dust could burrow on the order of 2 cm per sol, but for the depths measured from Chapter 2, this rate would imply 40 sols of illumination to clean the ice to the degree needed to observe albedos of these levels in late winter. Conversely, a rate of 16 cm per sol would be required to burrow through the 80 cm of ice estimated from Chapter 2 in roughly 5 days (comparable to annealing timescales). This value is 8 times higher than that estimated by Kieffer (2007) and is thus dust cleaning appears to be insufficient to explain albedos of these magnitudes at this time during sublimation.

Furthermore, these low springtime albedos correlate strongly with frost-free albedos of up to 0.19, but then asymptotically increase (Figure 28). This correlation suggests the underlying albedo is being observed in late winter, but the seasonal ice is forcing the albedo lower, to a critical point where albedo becomes unrelated to the frost-free surface albedo. The most plausible hypothesis for these observations is a finite layer of CO_2 ice with exceedingly large grain size, such that incident light is reflected off the substrate rather than the ice. The absorption of radiation from

being transmitted through the entire slab *twice* (absorption by the slab as light penetrates to the substrate, reflection off the dark substrate, and absorption by the slab as light exits to the atmosphere) would account for the correlated frost-free and frosted surface albedos. The fact that this occurs only on north-facing slopes suggests that illumination factors promote this behavior. The correlation could be explained by more-direct illumination forcing annealing of ice in late winter, though the likelihood of this is low considering CO_2 absorbing energy faster than it can radiate energy fractures and forces effectively smaller grain-sizes (albedo increases). As polar night ends and the sun shines for the first time, it is far more likely that fracturing occurs than annealing, at least initially. This is because the ice will be cold (potentially colder than its own frost-point) and on north-facing slopes will receive near direct-illumination due to the extremely high polar incidence angles in late winter. Annealing of deposits through vapor and grain-boundary diffusion is thought to occur on timescales of days (Eluszkiewicz, 1993; Eluszkiewicz *et al.*, 2005), whereas fracturing could presumably occur immediately upon illumination. Another possibility is the model suggested by Pommerol *et al.* (2011). This involves rapid surficial sublimation and "blow-off" of the top of the seasonal deposit to reveal a more pristine slab underneath. At $L_s = 160°$, polar night would have just ended, so it is plausbile that the first illumination of the year rapidly sublimes the top of the seasonal ice, especially on directly illuminated slopes. This sublimation process would need to occur faster than fracturing of the top layer of ice in order to preserve the low late winter albedo. This model can explain the correlation between albedo and aspect magnitude in late winter. Lastly, no atmospheric correction has been made to the HiRISE albedo, thus the low albedos could be attributed to the presence of aerosols, which have been shown to decrease the surface albedo in the near-infrared (Vincendon *et al.*, 2007). Despite

this, aerosols cannot account for the correlation between surface albedos, nor surface geometry. The surface as $L_s = 160°$ is therefore like a pristine slab deposit that is thicker on some north-facing slopes and thinner on others.

There is a small sub-set of north-facing slopes that do not exhibit the frost-free albedo relationship. Pixels with a frost-free surface albedo of ≈ 0.18 have no correlation to the early spring albedo, even on north-facing slopes. This upturn in the data may suggest the presence of a semi-infinite slab, where grain-sizes are still large, but reflection occurs off the slab ice. This would account for higher albedos because slab ice is intrinsically brighter than regolith at HiRISE wavelengths (Warren *et al.*, 1990; Hansen, 1999). A semi-infinite slab could be obtained through a thicker deposit, dust-doping, fracturing, or porosity. All of these attributes are indistinguishable with only albedo data in a small band width like HiRISE, becuase they effectively cause a reduction in the grain-size, and therefore an increase in albedo. Grain-size/porosity spectral modeling is the only method that would be able to separate these processes quantitatively. There appears to be no other variables correlated with this secondary group, so how this north-facing group differs from the other is unclear.

3.5.2 Increase of Albedo on North-facing Slopes Ending in a Maximum Positive Correlation Between Albedo and Aspect Magnitude at $L_s \approx 199°$

At $L_s \approx 199°$ the albedo is maximally correlated with the aspect magnitude. Figure 28a depicts the stretched HiRISE scene in relative brightness. The north-facing slopes are much brighter than the other ice in the image. The north-facing gullies are especially noteworthy, as are the small scale slopes in the bottom of the pit. I
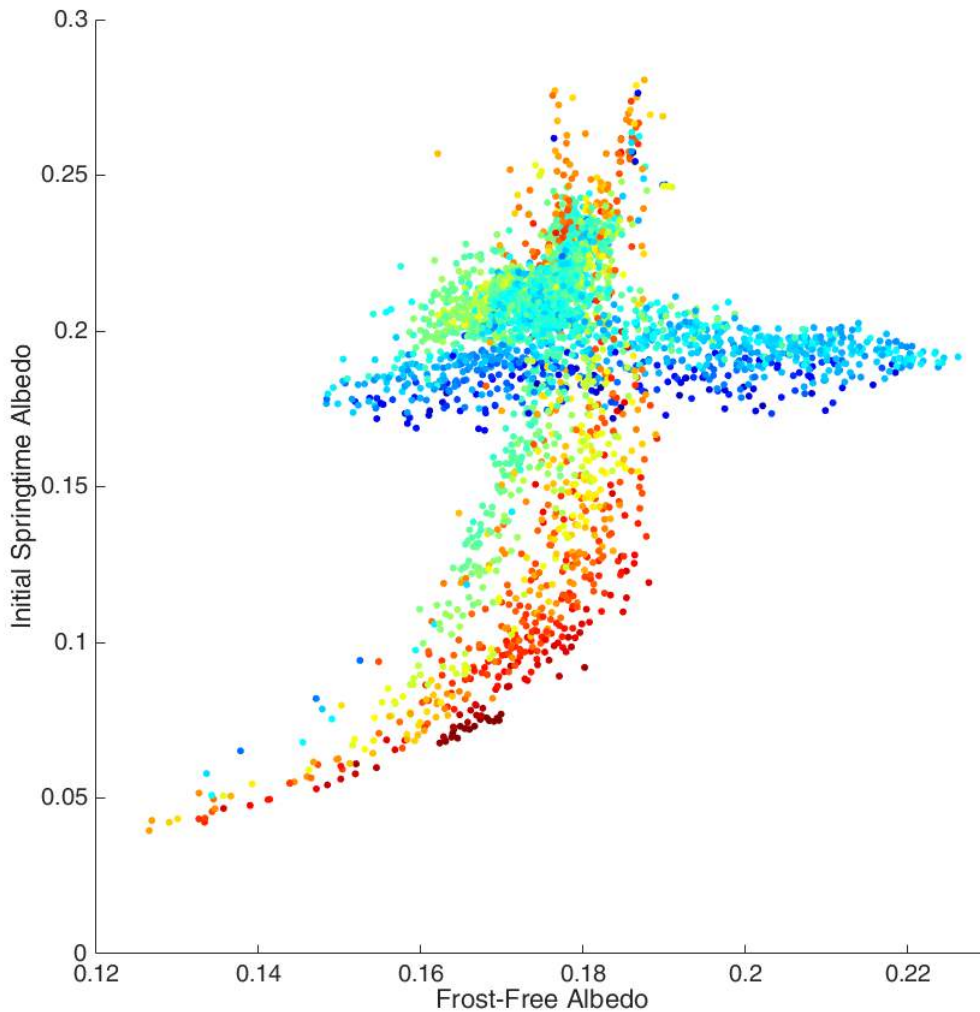
Figure 27. Initial Spring Albedo vs. Frost-Free Albedo

Coloration is the aspect magnitude, with reds being more north-facing and blues south-facing. North-facing slopes with frost-free albedos lower than 0.18 are strongly correlated with intial spring albedos. The initial spring albedos for these are remarkably low. The correlation vanishes at a frost-free albedo of 0.18. A second set of north-facing slopes has much higher initial spring albedos.
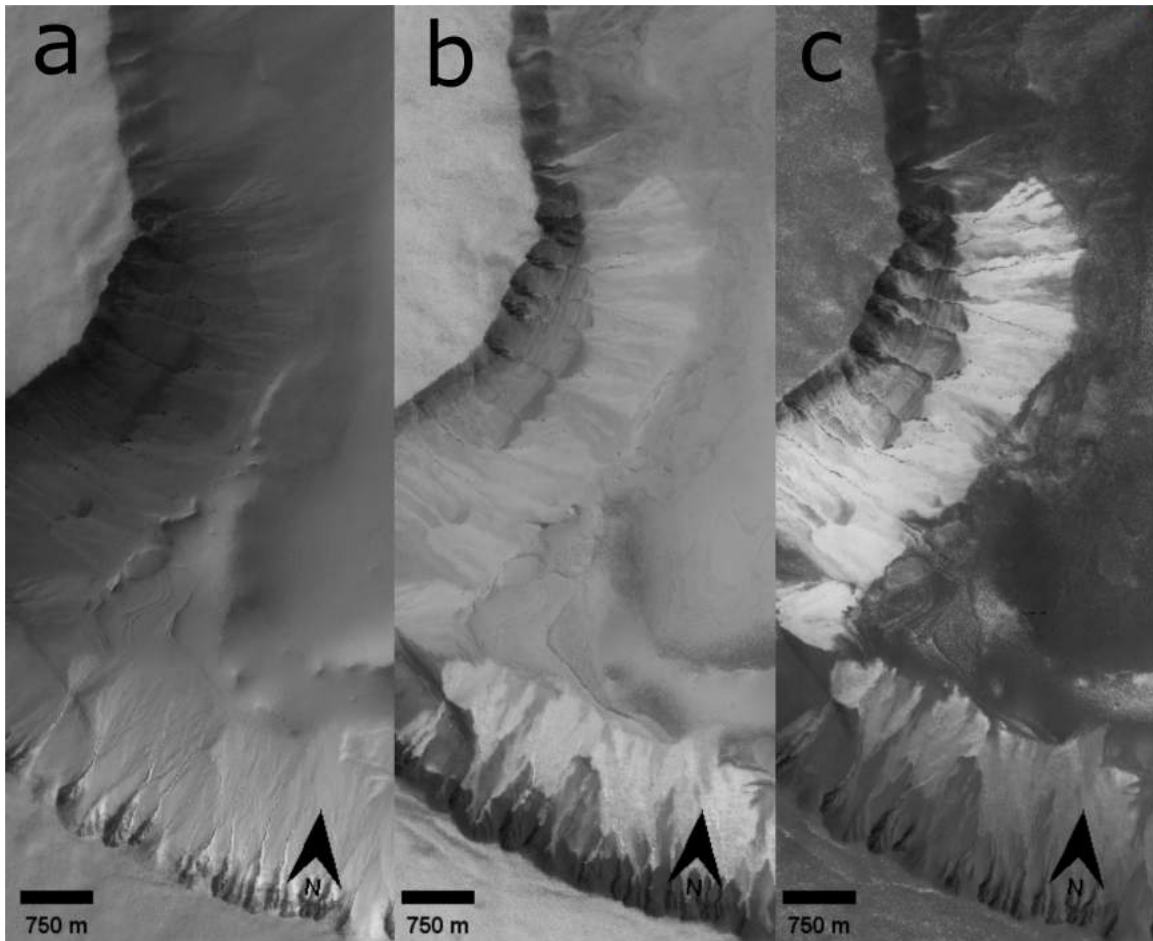
Figure 28. Brightness Images in Seasons of Correlation Inflection

a) $L_s \approx 199°$. North-facing slopes appear to be brighter than their south-facing counterparts. Particularly bright are the gullies on the north-facing scarp. b) $L_s \approx 227°$. The steep scarps and interstitial gully material appears to be at least partially defrosted and dark, while gullies remain bright. c) $L_s \approx 236°$. The seasonal ice has sublimed from most north-facing surfaces, with the exception of the north-facing gullies. South-facing slopes retain bright ice, though patchy in its appearance.

established that initially, the ice in the ROI is likely pristine slab. Thus, there is little chance that the brightening of north-facing slopes is caused by the surficial sublimation and cleansing of surface dust. Also, because the temperatures are uniform at the CO_2 condensation temperature of 150 K, it is unlikely that there would be preferential deposition of fresh CO_2 or H_2O on only the north slopes, therefore it is difficult to explain correlation between albedo and aspect magnitude if caused by cold-trapping of fresh seasonal deposits. However, with the increase of the regional albedo, fresh surface ice deposition cannot outright be dismissed (see below). It is probable that more direct illumination caused by the slope geometry promotes fracturing, as this process would be directly affected by the increased energy input into the surface by sun-facing slopes. No large-scale fracturing, like what Portyankina *et al.* (2012) observed, is observed in this ROI, though micro-fractures in the crystal lattice would reduce the effective grain-size and thereby increase the albedo. Micro-fractures would explain the disappearance of the correlation between ice albedo and frost-free albedo as spring progresses since the fractured ice would scatter or absorb light before it could transmit to the surface.

3.5.3 Increase of Albedo on Low-to-moderate Thermal Inertia Units Ending in a Maximum Negative Correlation Between Albedo and Thermal Inertia at $L_s \approx 227°$

The maximum negative correlation of albedo with thermal inertia occurs at $L_s \approx 227°$. Here, a stark dichotomy forms on the north-facing scarp (Figure 28b). Thermal inertia feature C (refer to Figure 17) has nearly completely defrosted as has the boulder-ridden north-facing scarp. However, what appears to be darker north-

facing slopes, the correlation of albedo with the aspect magnitude is nearly zero at this time. The timing of the appearance of this dichotomy is around the same time as the appearance of the Cryptic and Anti-cryptic regions (Kieffer *et al.*, 2000; Calvin *et al.*, 2017). The albedo of many of the high thermal inertia units are still higher than the frost-free albedo in these areas, suggesting that perhaps they are not completely defrosted. However, the estimated local date of ice disappearance calculated in Chapter 2 and the linear mixing analysis done by Raack *et al.* (2015) indicate that these surfaces should be defrosted. This discrepancy could be merely due to the high degree of error associated with HiRISE albedo or to atmospheric scattering because no attempts were made to remove the atmosphere in the the albedo data here. It is interesting then to note the correlation of albedo with thermal inertia at this time, because the correlation means high thermal inertia units are the first to sublimate in spring. There are two possibilties:

1. Either summer time heating is sufficiently stored by units with thermal inertia above ≈ 400 TIU to inhibit fall and winter deposition, such that ice is thinner and more rapidly sublimated than that on low thermal inertia units,
   or:

2. Absorption of solar radiation through overlying ice during the spring is sufficient to heat the regolith by late spring and keep high thermal inertia units warm through the night. The nighttime warmth could promote solid-state greenhouse effects and help basally sublimate the deposit.

Conversely, the presence of ice on low thermal inertia units at $L_s \approx 227°$ could suggest nighttime deposition as the low thermal inertia units cool rapidly. This is conceptually consistent with recent work of Piqueux *et al.* (2016) on diurnal emplacement of CO_2 at low latitudes and observations of re-condensation during SSPC spring re-

treat by Calvin *et al.* (2017). However, this may be unlikely because the HiRISE images are taken at approximate 4:00 pm local solar time, which means nighttime deposits would need to persist through the entire day.

3.5.4 Decrease of Albedo on North-facing Slopes Ending in a Maximum Negative Correlation Between Albedo and Aspect Magnitude at $L_s \approx 236°$

North-facing slopes experience an inversion in the albedo-aspect magnitude correlation as spring progresses until $L_s \approx 236°$. At this time most terrain has become mostly defrosted, with north-facing slopes are completely bare of ice (Figure 28c), which is the source of the strong negative correlation at this time. That is, north-facing slopes defrost before other slope facings in the ROI. Small scale troughs retain ice at this time. Presumably these retention of ice in these troughs is due to the same topographic effects as on the large scale, though it is difficult to determine and HRSC lacks the resolution to investigate such small scale features.

3.5.5 Regional albedo increase followed by decrease over spring

The increase in the regional albedo over spring is punctuated by peaks and troughs superposed on the general increasing trend. This is consistent with the idea of micro-fracturing to brighten the ice over time. The smaller temporal variations are harder to address. They may be the result of competing annealing processes (see Eluszkiewicz (1993); Eluszkiewicz *et al.* (2005)) sealing fractures and increasing the grain-size. It is also possible HiRISE is observing sudden deposits of fresh CO_2 and/or H_2O, though these would likely deposited as fine-grained frosts, and the albedo would be much

74

higher than observed. Atmospheric effects could also account for the variations witnessed. Interannual variability in this ROI appears to limited, but results from Chapter 2 indicate there are minor variations in Column Mass Abundance. The oscillatory nature of the regional albedo could also be a result of these interannual differences.

3.5.6   Future Work

Generally, these observations support that surface thermal inertia most likely affects the deposition of the seasonal ice during fall and winter. This was proposed by Haberle *et al.* (2004, 2008). Sophisticated, dynamic thermal modeling should be done to better understand how much of an impact the thermal inertia has on deposition. Localized depth estimates in the vein of Cull *et al.* (2010) and Mount and Titus (2015) could be made in late winter or early spring to confirm whether deposition is hindered during fall and winter by looking at depths on high thermal inertia vs. low thermal inertia units. If sublimation is indeed sufficient enough to remove ice from low thermal inertia terrain, thermal modeling of night time deposition should be done. Piqueux *et al.* (2016) have done this for low latitudes using Mars Climate Sounder. Something akin to their method may be adapted for use at high resolution with THEMIS to study diurnal deposition in the polar regions during spring.

In this region, the orientation and geometry of the surface appear to be the primary driver of its sublimation trends throughout spring. Other areas should be investigated in this same manner to see if the trends are similar. The ROI studied here had little evidence of dust within the seasonal ice (no dark spots, dust fans, or bright halos) and so could be indicative of the behavior of other areas with little dust. The exact

development of grain-size over spring requires spectral modeling in the visible-near-infrared (VNIR) of multilayered CO_2 deposits of varying grain size. Of particular interest would be VNIR models using the conceptual design of Eluszkiewicz *et al.* (2005) using CO_2 as the matrix and pores as the spherical "particles." Compact Reconnaissance Imaging Spectrometer for Mars often performs synchronous viewing with HiRISE and could offer excellent temporal coverage for comparison with the high-resolution features HiRISE provides.

Despite having dichotomic behavior at about the same time in spring as the emergence of the Cryptic and Anti-cryptic, this region is likely not a good analogue to Cryptic/Anti-Cryptic behavior. The absence of CO_2 being responsible for the dark areas in this ROI is not similar to Cryptic ice. The prevalence of dust-related phenomena are also a marked difference from this region. The ROI does exhibit an increase in brightness over spring, consistent with Anti-cryptic ice. Perhaps the anti-cryptic region merely has an abundance of north-facing slopes, which fracture during spring and increase the regional brightness as a result. Studies such as this one could be conducted within the anti-cryptic region, provided temporally dense data sets with similar observables are available.

3.6   Conclusion

Having discussed the possible evolutions of the trends observed here, the most probable is as follows: High thermal inertia units are warmed in the summer. During fall and winter deposition, these units retain heat, prohibiting deposition until later in the depositional season. This creates thinner deposits on high thermal inertia units and thicker deposits on low thermal inertia units. Surface deposition domi-

nates and a large-grained slab ice is deposited across the region. Initially in spring, the ice is illuminated and fractures. North-facing slopes receive more incident energy and fracture more than other ice in the region. As sublimation continues, the thin deposits fully sublimate and the high thermal inertia units defrost completely. Sublimation continues with north-facing slopes receiving more incident energy than south-facing slopes. These defrost by late spring, leaving only south-facing slopes and topographic lows with residual ice. The atmosphere and surface continue to warm eventually sublimating the remaining ice.

Chapter 4

THERMAL HYDRAULICS OF CRYOVOLCANIC CONDUITS ON CHARON

4.1 Introduction

The volatile inventories on Kuiper Belt Objects (KBOs) can help us understand the formation of our solar system, as well as the potential for life on these icy worlds (McKinnon *et al.*, 2008). In particular, water ice is ubiquitous across the Kuiper Belt (Grundy *et al.*, 1999). Surprisingly, a crystalline water ice spectral feature at 1.65 μm is likewise present on many medium-sized KBOs, such as Charon (Jewitt and Luu, 2004; Barucci *et al.*, 2008; Cook *et al.*, 2007). The temperatures in the Kuiper Belt are not sufficient to anneal amorphous water ice back to crystalline water ice (Mastrapa and Brown, 2006; Cook *et al.*, 2007) and any crystalline water ice on the surface should be amorphized by ultraviolet and galactic cosmic rays in about 0.03 Myr (Cook *et al.*, 2007).

Ammonia hydrates have been observed on some midsized KBOs by a 2.21 μm spectral feature (Jewitt and Luu, 2004; Cook *et al.*, 2007; Barucci *et al.*, 2008; DeMeo *et al.*, 2015; Cruikshank *et al.*, 2015), most likely ammonia dihydrate (ADH). However, ammonia hydrates are, like crystalline water, spectrally obscured by exposure to ultraviolet and galactic cosmic rays (Strazzulla and Palumbo, 1998) on the order of 1 Myr (Cook *et al.*, 2007). These processes imply that any observations of crystalline water ice or ammonia hydrates indicate geologic activity in the very recent past. An intriguing mechanism for forming crystalline water ice and ammonia hydrates on the surface of these KBOs is cryovolcanism (Jewitt and Luu, 2004; Cook *et al.*, 2007; De-

sch *et al.*, 2009). According to Desch *et al.* (2009), medium-sized KBOs may have had sufficient radiogenic heat to partially differentiate and retain a subsurface liquid water ocean underneath a rock-ice crust. An "antifreeze" (in the case of Charon, ammonia (Hogenboom *et al.*, 1997)) is required for the freezing temperature to be depressed such that liquid remains. This cryomagma then rises to the surface through cracks that self-propagate by exsolution of dissolved gases (Crawford and Stevenson, 1988), over-pressurization due to freezing (Fagents, 2003; Manga and Wang, 2007), and/or positive buoyancy due to mantle clathrates (Lunine and Stevenson, 1985), leaving behind crystalline water ice cryolavas intermixed with ammonia hydrates.

Neveu *et al.* (2015) predicted that conduits on Charon with a radius of ≈ 0.38 m or less would not have sufficient time to reach the surface before completely freezing. However, their prediction is derived from fairly simple theoretical calculations.

Desch *et al.* (2009) modeled the thermal evolution of medium-sized KBOs, accounting for convection and ammonia content. This was prior to the New Horizons flyby of the Pluto system in 2015. Desch and Neveu (2017) revised this model for Charon, taking the implications of the new observations into account (specifically, the impact formation hypothesis (Canup, 2011; Desch, 2015; Desch and Neveu, 2017; Mckinnon *et al.*, 2017)). The 2009 model appears to be inconsistent with Charon itself, because it assumes cold-accretion rather than accretion from an impact generated disk; however the internal structure proposed by the 2009 model proves useful for investigating extant cryovolcanism on other cold-accreted KBOs of medium size (e.g., Quaoar, Orcus) and extinct cryovolcanism on Charon. The discovery of Kubrick Mons and the lobate southern plains of Charon suggest potential past cryovolcanic events (Stern *et al.*, 2015; Moore *et al.*, 2016). Desch and Neveu

(2017) estimated the depth to a now-depleted or frozen source chamber for Kubrick Mons at ≈ 2.5 km.

Here, I create a numerical thermal hydraulic model to test the upper limit radius for a cryovolcanic conduit to completely freeze while flowing on a Charon-like body. I also use this model to determine conduit properties, timescales of eruption, and discharge rates for Kubrick Mons using the estimates made by Desch and Neveu (2017).

4.2   Methods

4.2.1   Conduit Geometry

The conduit is idealized as a two-dimensional cylindrical pipe. The azimuthal direction is neglected, leaving only the vertical and radial components. This pipe stretches from the bottom of the upper mantle to the surface. Due to the symmetry of the conduit, it is only necessary to model half of the pipe. This plane is then divided into cells. The vertical direction is broken into 100 different cells with an extra boundary cell on the top and bottom. The radial direction is a free parameter usually set to 5 cells. This is to increase computational speed (see below) and stability. Because of the large aspect ratio, despite the r-direction having fewer cells than the z-direction, cells in the vertical direction are much larger than cells in the radial direction. The conduit is assumed surrounded by material, following the internal structure for a cold-accreted medium-sized KBO from Desch *et al.* (2009) (Figure 29). This is consistent with the internal structure of Charon modeled by Desch and Neveu (2017) between 1.8 and 2.7 Gyr after the formation of CAIs.
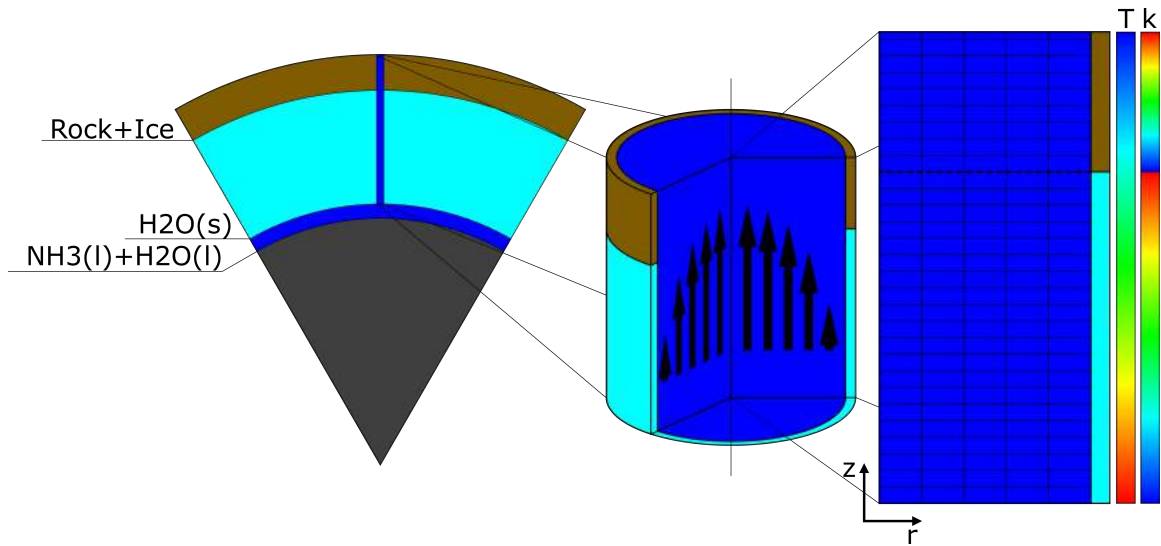
Figure 29. Illustration of Body and Conduit Structure

Interior structure of body (left), conduit geometry (middle), computational grid (right). The canonical simulation is assumed to traverse the entire upper mantle and through an undifferentiated crust. The mantle-crust boundary is indicated on the computational grid with a dotted line. Relative temperature and thermal conductivity of the boundary are shown. Due to the temperature and material dependence, there is a discontinuity at the mantle-crust boundary.

For the canonical simulation a conduit radius of $R = 0.30$ m was chosen, because Neveu *et al.* (2015) estimated that conduits slightly larger than this freeze. This radius provides a unique position where if the fluid freezes the cooling timescales of Neveu *et al.* (2015) are verified and if the material does not freeze, it indicates more processes are at work.

4.2.2   Boundary Conditions

The boundaries of the conduit assume the structure of the end-state calculated by the model of Desch *et al.* (2009). The surface temperature is set to the approximate surface temperature of Charon at 40 K. This is slightly lower than measured through

81

telescopic observations (Cook *et al.*, 2007; Holler *et al.*, 2017), but only affects the thermal conductivity of the boundary material and a 10 K difference makes only a 17% difference in the conductivity (7.3 W·m^{-1}·K^{-1} at 40 K, 6.3 W·m^{-1}·K^{-1} at 50 K). In either case, the surface thermal conductivity is very high and surface temperature is very cold. The base of the conduit is set at 180 K. This temperature is approximately the lower mantle temperature of the Desch *et al.* (2009) model, which is what is used for my canonical model. The outer radial boundary temperatures are a linear interpolation from the base temperature to the surface temperature (Figure 29).

The lower pressure boundary is held constant. The base over-pressure is computed using the approximation of Fagents (2003) from the thermodynamic definition of compressibility,

$$\Delta P = \frac{1}{\beta} \frac{\Delta V}{V} \tag{4.1}$$

assuming the compressibility, β, of liquid water 5×10^{-10} Pa^{-1}, assuming $\approx 55\%$ of the internal source chamber has frozen by volume, with a liquid water density of 1000 kg·m^{-3}, and a water ice density of 936 kg·m^{-3}. This assumes that freezing over-pressurization of the lower mantle is responsible for the upwelling of the fluid, as this is considered the most-likely method of cryomagma delivery to the surface (Desch and Neveu, 2017). The pressure at the inlet of the conduit is calculated by adding the lithostatic pressure at depth ($\rho g h$) to the over-pressure calculated from the equation above. For the canonical simulation with a length of conduit equal to 232 km, this inlet pressure is 200 MPa, with a lithostatic pressure of ≈ 70 MPa and an over-pressure of 130 MPa, regardless of conduit radius. The depth to the Kubrik Mons source chamber was estimated to be 2.3 km (conduit length), with an assumed volume fraction of $\approx 60\%$ of the source chamber frozen, a lithostatic pressure of

≈ 0.65 MPa, and an over-pressure of ≈ 199 MPa. The surface pressure is held constant at 0 Pa, consistent with an airless body.

Thermal conductivity at the boundary is temperature- and material-dependent. These are computed with the equations for pure ice conductivity and rock-ice mixture conductivity approximations of Desch *et al.* (2009) and are used when computing the heat conducted from the fluid out of the system. Any energy conducted into the mantle and crust are assumed to conduct away so that the conduit walls experience no change in energy.

The fluid velocity has a no-slip condition imposed on the wall boundary. The inlet and outlet boundaries have a zero-gradient (Neumann) condition. The boundary at the pipe center is assumed to be symmetric and so has a zero-gradient, as well.

4.2.3   Governing Equations

The model incorporates an explicit, central finite difference system of equations. The flow is forced to be 1-D laminar with 2-D heat diffusion. The fluid is considered "pseudocompressible" in that the density does not depend on the pressure (see below), but $\nabla \cdot \mathbf{v}$ is non-zero. The conservation of mass is derived from the mass continuity equation, then further manipulated through the density equation of state to be in the form of pressure (see §A). The fluid flow is then restricted to vertical flow, only.

$$\frac{\partial P}{\partial t} = -v\frac{\partial P}{\partial z} - \frac{\partial \rho}{\partial P}\bigg)_T^{-1}\left[\frac{\partial \rho}{\partial T}\bigg)_P\left(\frac{\partial T}{\partial t} + v\frac{\partial T}{\partial z}\right) + \rho\frac{\partial v}{\partial z}\right] - S_P \qquad (4.2)$$

The source term S_P is computed to satisfy the Neumann condition on the velocity and Dirichlet condition on the pressure at the conduit outlet. This term is found by setting the change in pressure over time to zero and solving for the source term under
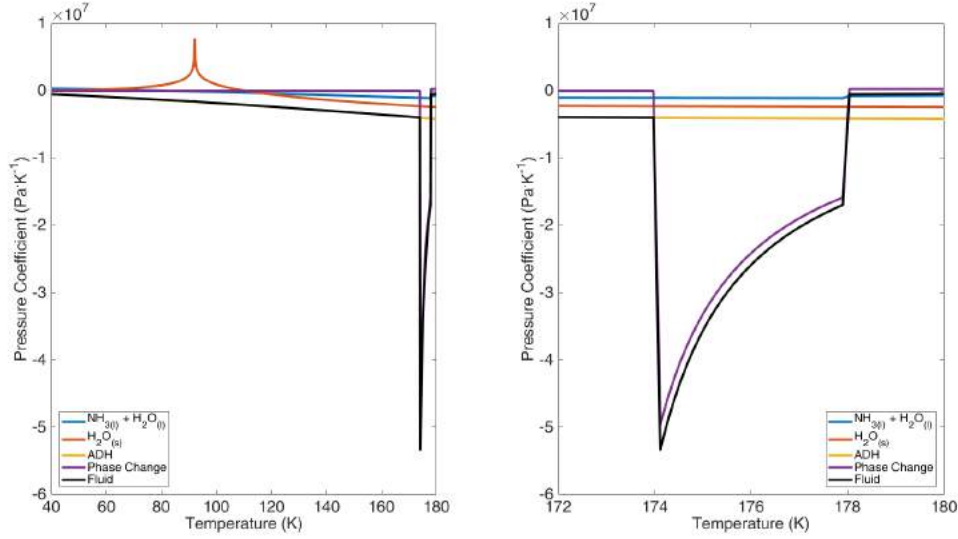
Figure 30. Pressure Coefficients as a Function of Temperature

Pressure coefficients for components and composite fluid calculated by differentiating the density equation of state with respect to pressure and temperature. The "phase change" curve is from propagation of the mass fractions as a function of temperature and is representative of density changes from phase change between chemical species. The right plot is a zoomed in view of the freezing envelope (see below).

zero velocity and steady energy conditions at the boundary (see §A for details). The product of the pressure and temperature derivative terms is the pressure coefficient $\partial P/\partial T)_V$ and graphed in Figure 30.

Conservation of momentum is derived using a generalization of Newton's second law to a fluid volume. Gravity is assumed as the only body force, while the surface forces are due to viscous stresses. The flow is then assumed laminar and restricted to only the vertical direction.

$$\frac{\partial v}{\partial t} = -v\frac{\partial v}{\partial z} - g + \frac{1}{\rho}\left(\frac{\partial \tau_{zz}}{\partial z} + \frac{\partial \tau_{rz}}{\partial r} + \frac{\tau_{rz}}{r}\right) \tag{4.3}$$

The stress tensor, τ, is computed as the geometric mean of the Newtonian stress

tensor and the power law stress of Durham *et al.* (1993) by volume fraction. This is defined by

$$\underline{\underline{\tau}} = \underline{\underline{\sigma}}_l^{g_l} \cdot \underline{\underline{\sigma}}_s^{g_s} - P\underline{\underline{I}} \tag{4.4}$$

where the subscripts l and s denote the liquid and solid phases, respectively. The stress tensor for the liquid phases is defined as newtonian and has the form

$$\underline{\underline{\sigma}}_l = \lambda(\boldsymbol{\nabla} \cdot \mathbf{v})\underline{\underline{I}} + 2\mu\underline{\underline{\dot{\varepsilon}}} \tag{4.5}$$

and the solid components follow the method used by Durham *et al.* (1993) and Tullis *et al.* (1991) to describe a mutli-end-member polyphase aggregate, which is

$$\underline{\underline{\sigma}}_s = C^{-\frac{1}{n}} \underline{\underline{\dot{\varepsilon}}}^{\frac{1}{n}} e^{\frac{G}{nRT}} \tag{4.6}$$

The rate of strain tensor, $\underline{\underline{\dot{\varepsilon}}}$, is defined as

$$\underline{\underline{\dot{\varepsilon}}} = \frac{1}{2}\left[(\boldsymbol{\nabla} \otimes \mathbf{v}) + (\boldsymbol{\nabla} \otimes \mathbf{v})^{\mathrm{T}}\right] \tag{4.7}$$

and C, n, and G are computed directly via the method of Tullis *et al.* (1991) with materials parameters from Durham *et al.* (1993). It should be noted that the root of a tensor generally does not have a unique solution. Also, the rate of strain and stress tensors can be negative, which can result in complex values when computing the power law. Because of these, I do not attempt to evaluate the root tensor, rather compute the root of each individual value within the tensor and take the only the real component. This preserves the sign (direction) of the stress and is consistent with the methodology of Tullis *et al.* (1991), Durham *et al.* (1993), and Kargel *et al.* (1991).

This stress tensor describes a two-end member rheology where at low solids fractions the fluid behaves as a Newtonian fluid, while at high solids fraction it behaves as a two-component power-law aggregate. Generally, a liquid ammonia-water fluid is

non-Newtonian; however near the peritectic it is approximately Newtonian (Kargel *et al.*, 1991), which is near the canonical simulation initial temperature (see below).

The conservation of energy is calculated from the first law of thermodynamics and mechanical energy assuming conduction is the only heat transfer process, except at the conduit outlet, where the fluid radiates to space.

$$\frac{\partial e}{\partial t} = -v\frac{\partial e}{\partial z} + \frac{1}{\rho}\left[k\left(\frac{\partial^2 T}{\partial z^2} + \frac{\partial^2 T}{\partial r^2} + \frac{1}{r}\frac{\partial T}{\partial r}\right) + \frac{\partial k}{\partial z}\frac{\partial T}{\partial z} + \frac{\partial k}{\partial r}\frac{\partial T}{\partial r}\right.$$
$$\left. + \tau_{zz}\frac{\partial v}{\partial z} + \tau_{zr}\frac{\partial v}{\partial r} - \delta_{z0}\frac{\sigma_B T^4}{\Delta z}\right] \tag{4.8}$$

Here, the first term on the right hand side is the energy advection, the terms with thermal conductivities, k, and temperature derivatives are heat conduction terms from Fourier's law, the terms with stress tensor components and velocity gradients are the viscous dissipation, and the last term is the radiative term. δ_{z0} is the Kronecker delta, which is equal to 0 in all cells except is equal to 1 when a cell is located at the surface ($z = 0$). The temperature at the vertical boundary is assumed 0 K, for simplicity. This equation allows forward calculation of the energy. The temperature is then back-calculated with the updated energy every time-step using the energy equation of state (see §4.2.4).

4.2.4   Initial Conditions and Variables

The initial pressure of the fluid is calculated by vertical linear interpolation from the bottom boundary pressure to the surface boundary pressure. It is then allowed to evolve according to equation 4.2.

The initial temperature is set to the base temperature of the conduit. For the canonical simulation this is 180 K. The internal energy is calculated from this with the equation of state from Desch *et al.* (2009) (Figure 31) by computing the energy re-
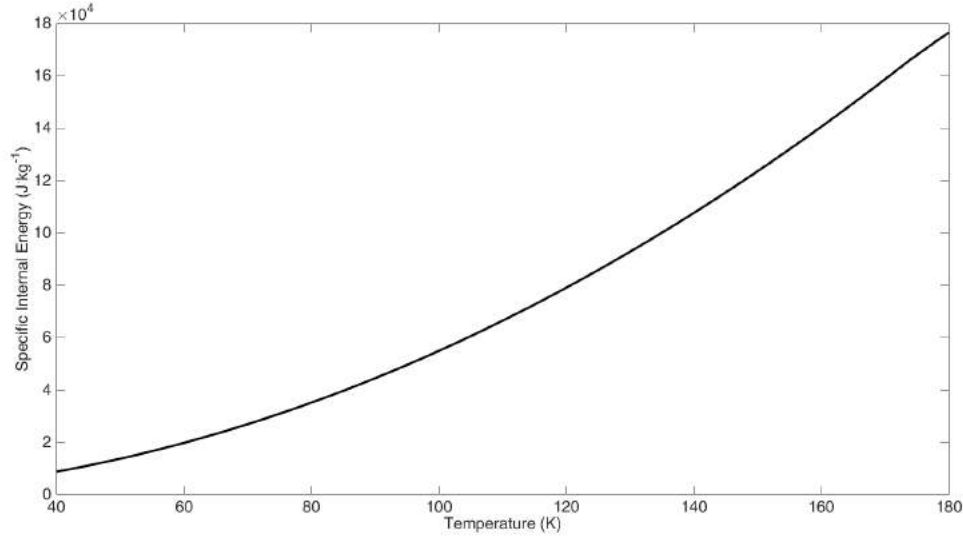
Figure 31. Energy Equation of State as a Function of Temperature

Energy equation of state (equation 4.9) for the canonical simulation derived from Desch *et al.* (2009).

quired to increase the temperature of the fluid to the initial temperature by integrating the specific heat and mass fraction of the components from 0 K to said temperature.

$$e = \sum_x \int_0^T g_x(T)c_p(T)\mathrm{d}T \tag{4.9}$$

Temperature dependent mass fractions are computed by way of lever rule making assumptions about the ammonia mass fraction of the liquidus to acquire an analytical solution of the mass fraction as a function of temperature (Desch *et al.*, 2009). These mass fractions are computed in three separate temperature regimes: Regime 1 - 0 to 174 K, Regime 2 - 174 to 178 K, and Regime 3 - 178 to 271 K. Because the melting point of ammonia dihydrate (ADH) is 176 K, this creates a 4 K freezing envelope around the freezing point where mass fractions are linearly interpolated by temperature, assuming any liquid freezes to ADH at 174 K. The curves for these are displayed in Figure 32.

87
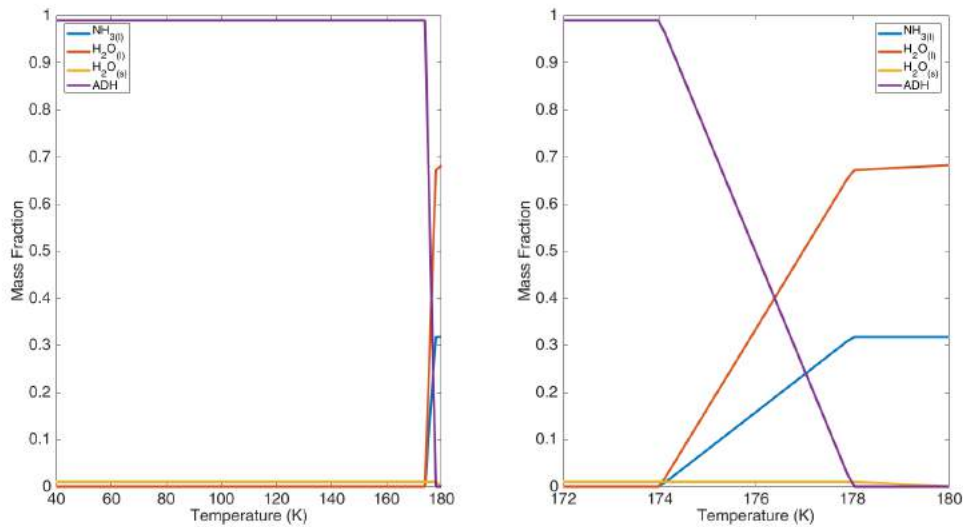
Figure 32. Component Mass Fractions as a Function of Temperature

Mass fractions for each component calculated by lever rule assuming canonical simulation initial conditions. The right plot is a zoomed in view of the freezing envelope.

The specific heat of the solid components is estimated with temperature dependent approximations to the equations of Shulman (2004) and Fortes *et al.* (2003) for H_2O and ADH, respectively (see Desch *et al.* (2009) for details). The specific heat of the liquid components is assumed constant at 4188.5 $J \cdot kg^{-1}$ water and 4700 $J \cdot kg^{-1}$ for ammonia (Figure 33).

The initial mass fraction of water ice in the fluid is unknown. The conceptual model from Desch *et al.* (2009) implies that water ice condenses from the liquid mixture during cooling/heating and differentiates. This condensation drives water ice upward due to buoyancy, creating the pure ice upper mantle. Therefore, the fluid could hypothetically contain up to 100% water ice. Nevertheless, for the canonical
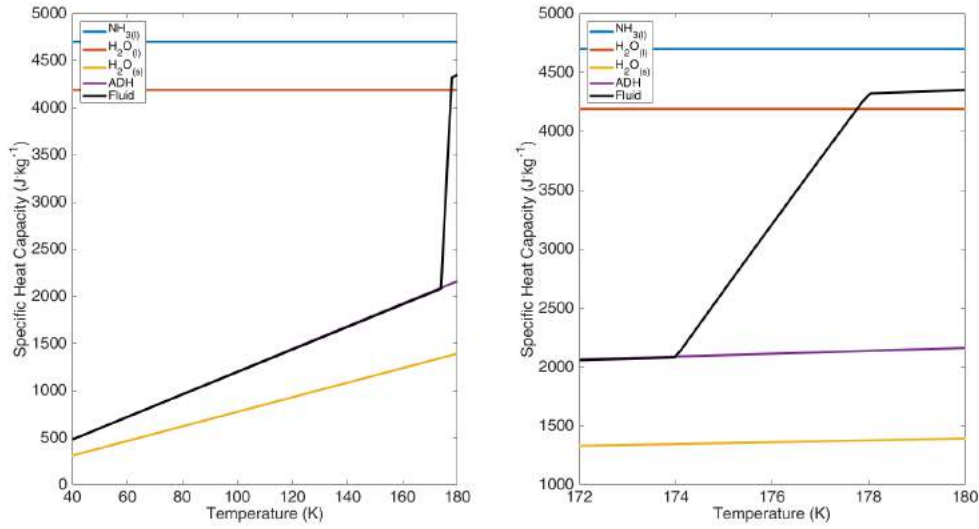
Figure 33. Specific Heat Capacity as a Function of Temperature

Mass specific heats for components and composite fluid used in energy equation of state and stability criterion. The right plot is a zoomed in view of the freezing envelope.

simulation I set this to zero, assuming any differentiated solids adhere to the upper mantle and separate from the fluid.

Velocity is restricted to only z-direction flow. Initial velocity for any simulation is found with the analytical solution for Poiseuille flow

$$v(r) = -\frac{R^2}{4\mu}\left(\frac{\partial P}{\partial z} + \rho g\right)\left(1 - \frac{r^2}{R^2}\right) \tag{4.10}$$

and is allowed to evolve from those values according to equation (4.3).

The effective viscosity here is computed as a temperature-dependent two end-member function and is used for computing the stability criterion. This is described by Kargel *et al.* (1991) as

$$\mu_{eff} = \mu_l^{h_l}\mu_s^{h_s} \tag{4.11}$$

where h_l and h_s are the mole fraction for liquid and solid components, respectively. The viscosity of the liquid, μ_l, is calculated using the empirical relation for an H_2O-

89

NH$_3$ liquid (Kargel *et al.*, 1991). This parameter is input into the stress tensor for the dynamic viscosity. The solid viscosity, μ_s, is calculated using the effective viscosity (σ/ϵ) of the two end-member alloy stress tensor of Tullis *et al.* (1991) with the constants for H$_2$O$_{(s)}$ and ADH from Durham *et al.* (1993). Because the stress tensor is reliant on the rate-of-strain, and therefore the velocity, the code is "spun-up" at time t=0. During spin-up, the stress tensor and velocity are updated and evaluated iteratively using equation (4.3) until a steady-state is reached. The steady-state is defined as when the change in velocity over time is less than or equal to the truncation error for the finite difference of the canonical Poiseuille flow.

Bulk viscosity is necessary due to the "pseudocompressibility" of the fluid (see below). Holmes *et al.* (2011) have argued that this parameter is quite important for the study fluid properties, and that water should not be considered incompressible. To this end, they determined the bulk viscosity to be $\approx 3\mu$ for liquid and solid water independent of the temperature. I adopt this relation for computing the Newtonian stress tensor for the water-ammonia liquid.

The density equation of state is calculated as

$$\frac{1}{\rho} = \frac{\left(g_{H_2O_{(s)}} + g_{NH_{3(l)}}\right)}{\rho_l} + \frac{g_{H_2O_{(s)}}}{\rho_{H_2O_{(s)}}} + \frac{g_{ADH}}{\rho_{ADH}} \tag{4.12}$$

where ρ_l, $\rho_{H_2O_{(s)}}$, and ρ_{ADH} are calculated from the empirical formulations of Croft *et al.* (1988), Feistel and Wagner (2006), and Fortes *et al.* (2003). Both the Croft *et al.* (1988) and Fortes *et al.* (2003) equations of state are of Murnaghan form (Murnaghan, 1944) with a power law thermal expansion coefficient. The Feistel and Wagner (2006) equation of state uses a Gibbs potential function and is exceedingly complex. The pressure is set to 0 for calculating the density, because the fluid is assumed incompressible. However, it is important to have the dependence of the density on the pressure due to the pressure derivative in equation (4.2). This is because the phase
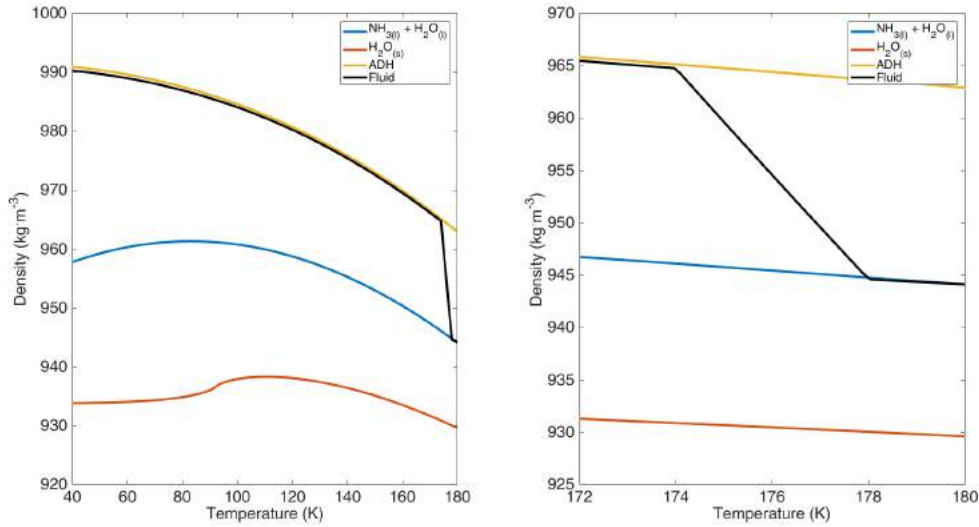
Figure 34. Density Equation of State as a Function of Temperature

Density equation of state for components and composite fluid assuming a pressure of zero. The right plot is a zoomed in view of the freezing envelope.

change affects the pressure, and thus the vertical velocity gradient (i.e., $\nabla \cdot \mathbf{v}$ is generally non-zero). This leads to compression effects despite the density being independent of the pressure. Therefore, the fluid is more "pseudocompressible" rather than genuinely incompressible. The density equation of state is shown in Figure 34.

Thermal conductivity of liquid ammonia-water mixtures at temperatures below ≈ 285 K have not been studied. However, isolated liquid water and ammonia conductivities have been acquired. Liquid water at its freezing temperature has a thermal conductivity of ≈ 5 W·m^{-1}·K^{-1} (with variations depending on the density) (Huber *et al.*, 2012), and liquid ammonia at 199 K has a thermal conductivity of 0.53 W·m^{-1}·K^{-1} (Varlashkin and Thompson, 1963). Liquid water thermal conductivity decreases with decreasing temperature, while liquid ammonia thermal conductivity increases with increasing temperature. It is unclear how the anti-freeze affects water

91
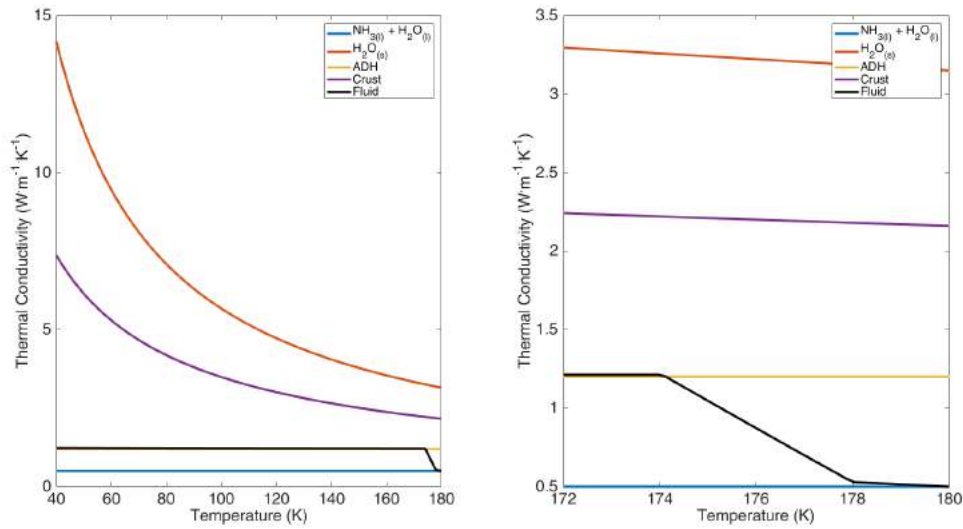
Figure 35. Component Mass Fractions as a Function of Temperature

Mass fractions for each component calculated by lever rule assuming canonical simulation initial conditions. The right plot is a zoomed in view of the freezing envelope.

under the freezing temperature and the opposite dependence on temperature generates a high uncertainty in the thermal conductivity of the mixture at low temperatures. Despite this, the conductivities for both pure substances are similarly low. Therefore, I adopted a constant thermal conductivity for the ammonia-water liquid of 0.5 $W \cdot m^{-1} \cdot K^{-1}$. The thermal conductivity of ADH is taken as a constant 1.2 $W \cdot m^{-1} \cdot K^{-1}$ (Desch *et al.*, 2009; Ruiz, 2003) and the conductivity of water ice as the temperature dependent formulation mentioned in §4.2.2. These are arithmetically averaged by volume fraction to find the composite thermal conductivity of the fluid (Figure 35).

Initial conditions for the canonical simulation and Kubrick Mons are displayed in Table 2.

Table 2. Initial Conditions and Constants for Simulations

Variable	Symbol	Units	Canonical	Kubrick Mons
Length	L	km	232	2.3
Radius	R	m	0.30	0.02
Inlet Pressure	P_{base}	MPa	200	200
Outlet Pressure	P_{surf}	Pa	0	0
Inlet Temperature	T_{base}	K	180	178
Outlet Temperature	T_{surf}	K	40	40
Initial Ammonia Concentration	X_i	-	0.3176	0.3210
Initial Crystal Mass Fraction	X_s	-	0.00	
Latent Heat of Melting of Water	$L_{\text{H}_2\text{O}}$	J·kg^{-1}	3.335×10^5	
Latent Heat of Melting of ADH	L_{NH_3}	J·kg^{-1}	1.319×10^5	
Specific Heat of Liquid Water	$c_{\text{P},\text{H}_2\text{O}_{(l)}}$	J·kg^{-1}	4188.5	
Specific Heat of Liquid Ammonia	$c_{\text{P},\text{NH}_{3(l)}}$	J·kg^{-1}	4700	
Liquid Thermal Conductivity	k_l	W·m^{-1}·K^{-1}	0.5	
ADH Thermal Conductivity	k_{ADH}	W·m^{-1}·K^{-1}	1.2	
Power Law Strain Rate Dependence for Ice	$n_{\text{H}_2\text{O}_{(s)}}$	-	5.60	
Power Law Strain Rate Dependence for ADH	n_{ADH}	-	5.81	
Pre-exponent Strain Rate Coefficient for Ice	$C_{\text{H}_2\text{O}_{(s)}}$	MPa^{-n}	-1.4	
Pre-exponent Strain Rate Coefficient for ADH	C_{ADH}	MPa^{-n}	21.55	
Activation Energy for Ice	$G_{\text{H}_2\text{O}_{(s)}}$	J	4.3×10^4	
Activation Energy for ADH	G_{ADH}	J	1.075×10^5	
Gravitational Acceleration	g	m·s^{-2}	0.3	

4.2.5   Dimensionless Parameters

The mean Reynolds, Prandtl, and Peclet numbers are computed for the fluid. Each is calculated for cells individually, then the mean dimensionless quantity is calculated. The Reynolds number is used to determine if the flow regime is turbulent or laminar. If the Reynolds number is above 2500 the code is designed to terminate. This is calculated with

$$Re = \frac{\rho v D}{\mu_{\text{eff}}} \tag{4.13}$$

where D is the diameter.

The Prandtl number gives insight into the effective viscosity as well as the way momentum is diffused in the system. This is an intrinsic property of the liquid and

93

is computed by

$$Pr = \frac{c_P \mu_{\text{eff}}}{k} \tag{4.14}$$

The Peclet number is utilized to understand whether advection dominates or heat diffusion dominates in the fluid, with numbers exceeding 1 indicating advection dominates, thus conduits are less likely to freeze, while number under 1 suggest heat diffusion is sufficient to transport heat rapidly and freeze the pipe. The Peclet number used here is

$$Pe = \frac{\rho c_P v R^2}{kL} \tag{4.15}$$

where k is the thermal conductivity.

4.2.6 Stability

The model equations follow an explicit scheme, so stability is highly reliant on the timestep. The timestep varies throughout a simulation according to a Courant conditionm, which requires the timestep to be

$$\Delta t = C \left[\left(v + \sqrt{\frac{P}{\rho} + e} \right) \frac{2}{\Delta z} + \frac{k}{\rho c_P} \left(\left[\frac{2}{\Delta z} \right]^2 + \left[\frac{2}{\Delta r} \right]^2 \right) \right]^{-1} \tag{4.16}$$

Arithmetic is done through the entire field, then the minimum timestep is taken to ensure stability. C is a value less than 1 that is used to further ensure stability, usually set to $\frac{1}{2}$.

4.3 Results

4.3.1 Model Validation

I chose three simple cases to test this model, its assumptions, and simplifications. All incorporate a filled pipe with a uniform fluid with initial values of $T = 180$ K, $k = 0.5$ W·m^{-1}·K^{-1}, $X_s = 0$, and boundaries at $R = 0.3$ m, $L = 232$ km, $P_{\text{base}} = 200$ MPa, $P_{\text{surf}} = 0$ Pa, $T_{\text{base}} = 180$ K, $T_{\text{surf}} = 40$ K. The first case was to set the velocity to the Poiseuille profile and to not allow changes in energy. Part way through the simulation, the base pressure was increased by a factor of 1.25. To test the behavior of the mass continuity formulation and whether the pressures were propagating in the fluid predictably. The pressure and velocity fields were then allowed to evolve over time. This was run until the pressure field returned to linear and the velocity entered a steady state (Figure 36).

The simulation ran as expected. The analytical solution to these conditions would be a parabolic Poiseuillean profile, which is the assumed initial condition. No changes occur in the flow velocity or pressure if the conditions are run out indefinitely. The shift in the pressure at the base of the pipe at t = 1000 s ($\approx$17 minutes) has an analytical solution of a Poiseuillean profile as well given it is fully developed. The pressure wave should propagate from the base up to the top of the pipe, with the fastest moving portions of the fluid advecting the pressure quickest. This is the case. The center of the conduit increases in pressure first, followed by each radial column out to the boundary. This pressure increase happens relatively rapidly, consistent with the low compressibility of the liquid. The flow does not reach steady state until
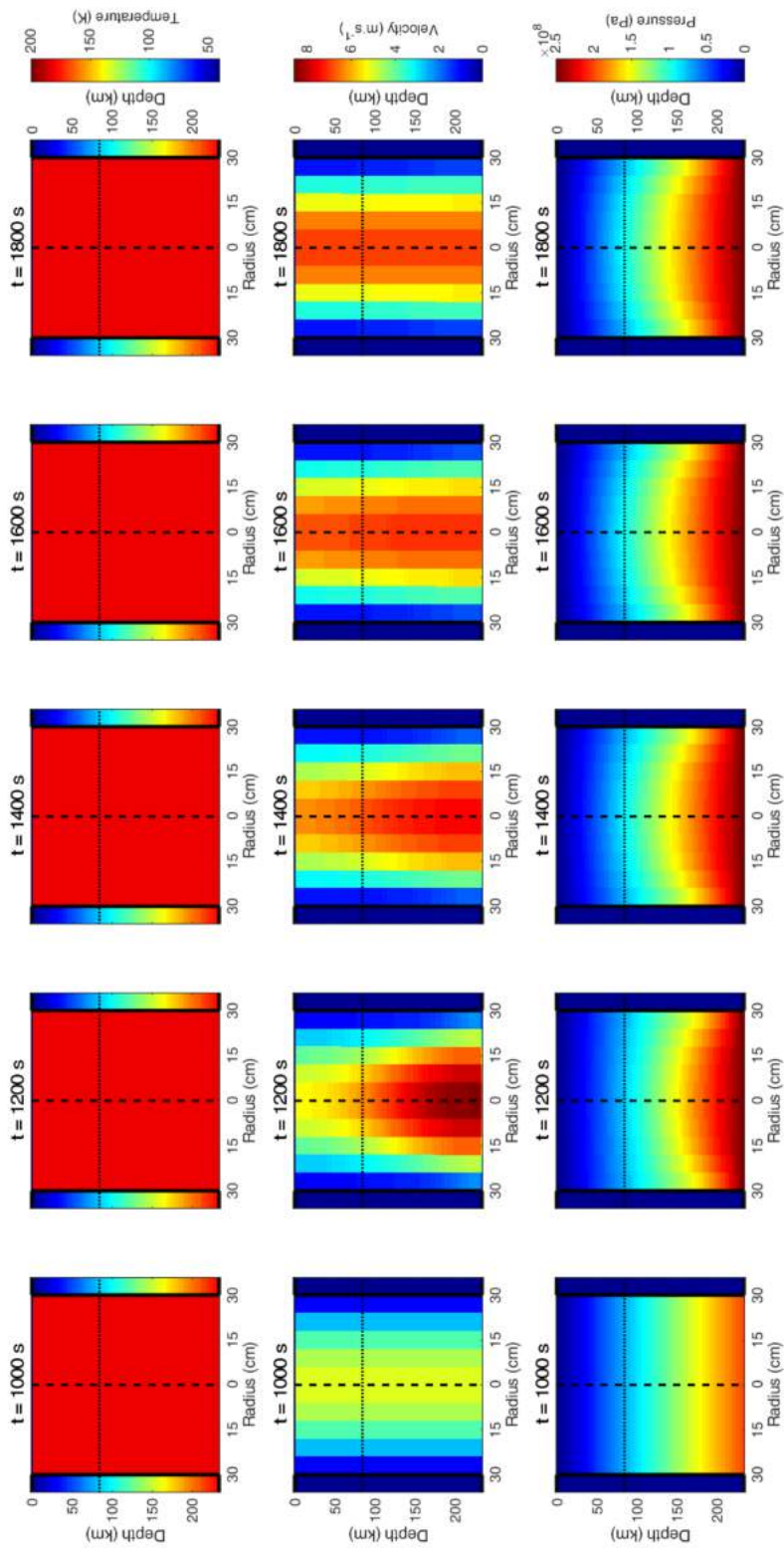
Figure 36. Steady State Conduit with Pressure Increase for Canonical Geometry.

Temperature (top), velocity (middle), and pressure (bottom) of an R = 0.30 m conduit of near-peritectic water-ammonia mixture. The conduit is filled with no change in energy allowed. The initial velocity profile is Poiseuillean with a no-slip radial boundary and Neumann vertical boundaries. At 1000 s, the pressure at the base is increased by a factor of 1.25. The pressure wave propagates quickly through the fluid. The simulation was run out to 10^4s (≈ 2.8 hours), at which time the pressure gradient stabilizes and the flow again acquires a Poiseuille profile.

96

about 10^4 seconds ($\approx$2.8 hours). At that time the velocity profile is equivalent to the analytical solution and is in a steady state.

The second case was a zero-velocity field with a constant conductivity boundary that allowed only the energy to change over time through conduction. This case was run until the field reached thermal equilibrium with the boundaries (Figure 37).

The radial boundaries are in thermal contact with the cold surface walls, thus we should expect cooling from the outside-in, and top-down. That is, the bottom center should be the last to cool and freeze. This is indeed the case, though the timescale for cooling with this set-up is much longer than the timescale to advect the pressure change from the previous simulation. This simulation was run out to $\approx$2 $\times$ 10^5s (2.3 days), with equilibrium being reached at about 1.6×10^5s (1.9 days). The pressure increases at the base of columns that cool and freeze. Normally, one would expect a pressure decrease with freezing. However, due to the surface Dirichlet condition on the pressure, the source term instead anchors the surface pressure to zero, forcing the inlet pressures to increase. This pressure gradient would force motion of the fluid to conserve mass, but the velocity in this case is forced to be zero.

Lastly, I isolated the viscous dissipation term in the energy equation to understand its behavior and whether it was operating as expected. To do this I removed the conductive term in the energy equation and let the velocity, pressure, and energy evolve over time. The viscous dissipation depends on the stress tensor and spatial velocity gradient, the boundaries of the pipe should be expected to heat up the most. This is the case, with an increase in temperature of approximately 1.7×10^{-3} K·s^{-1} for the outermost column of fluid. The increase in temperature reduces the viscosity, which causes the velocity to increase, resulting in a positive feedback loop that further increases the velocity gradient and thus the viscous dissipation. The entire conduit
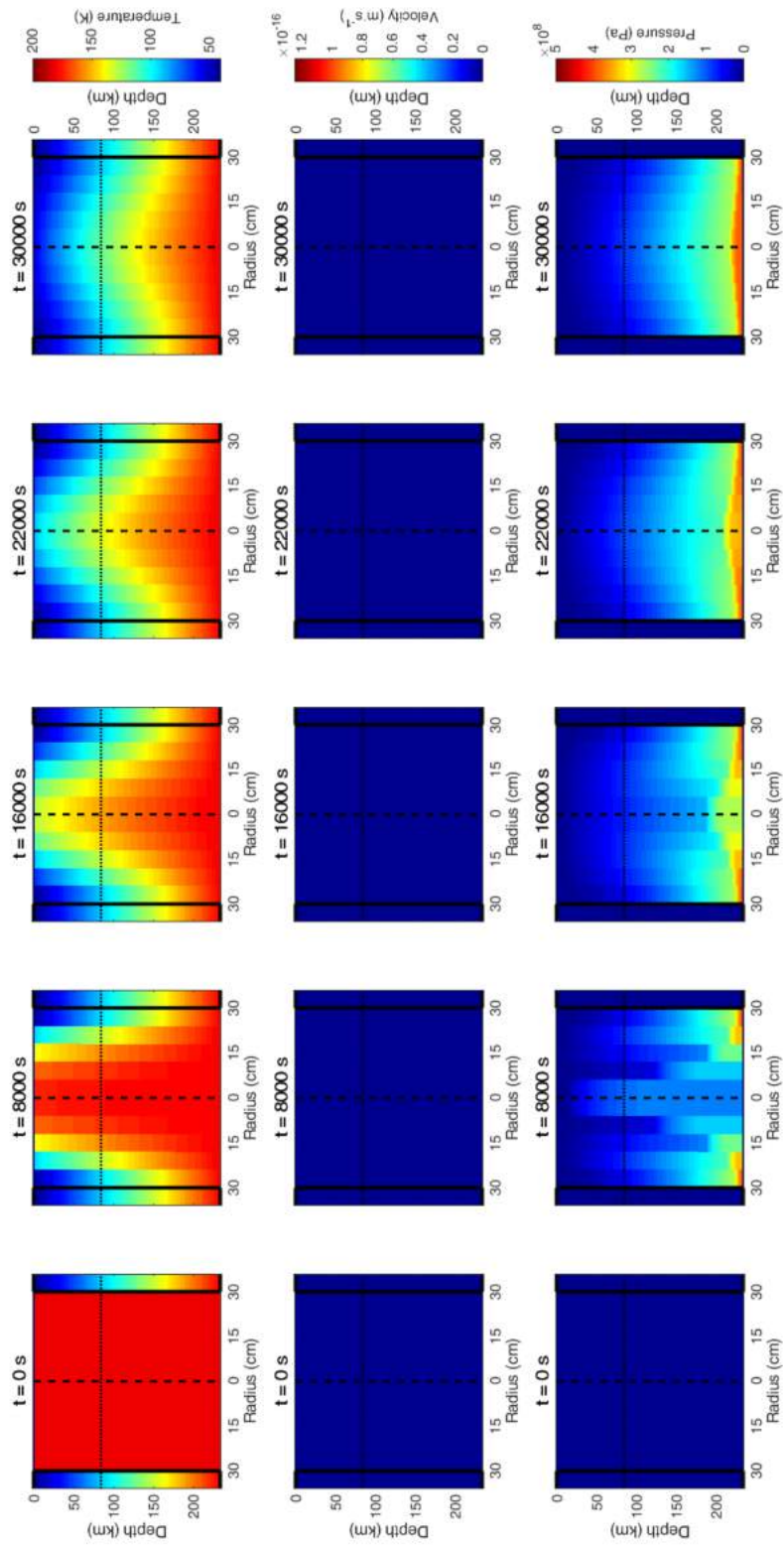
Figure 37. Zero Velocity Conduit with Energy Diffusion by Conduction Only

Temperature (top), velocity (middle), and pressure (bottom) of an R = 0.30 m conduit of near-peritectic water-ammonia mixture. The conduit is filled, with only conduction contributing to heat diffusion. The initial velocity profile and pressure field are set to zero everywhere and the velocity is not allowed to evolve.
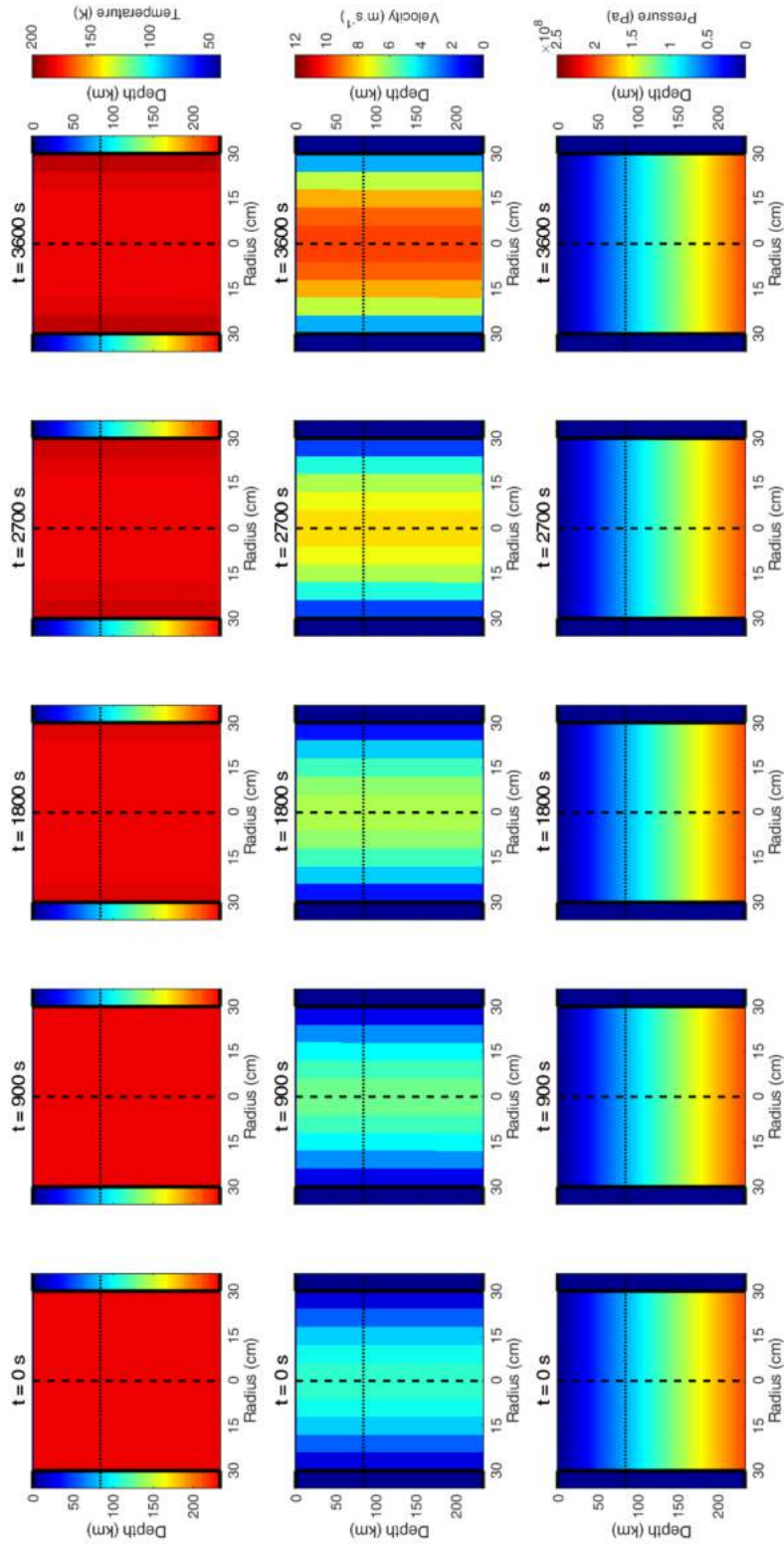
Figure 38. Effects of the Viscous Dissipation

Temperature (top), velocity (middle), and pressure (bottom) of an $R = 0.30$ m conduit of near-peritectic water-ammonia mixture. The energy equation is limited to the viscous dissipation only. The timescale for heating is much faster than for conduction.

increases in velocity, due to the reduced friction experienced from the edge of the pipe. The simulation rapidly reaches turbulent flow regimes at around 3600s (1 hour). The degree of heating due to viscous dissipation is high and likely contributes greatly to keeping the pipe from freezing (see below). Results are indicated in Figure 38.

4.3.2 Canonical Simulation

The results of the canonical simulation are detailed in Figures 39 - 42. Temperatures on the conduit wall decrease immediately after the initiation of the simulation. Freezing occurs for the outer column from the outlet downward along the conduit boundary. The entire outer column reaches temperatures in Regime 2 just before 1000 s ($\approx$ 17 minutes). After this, the decrease in temperature slows to near-steady state. As temperatures decrease in the outer column, the solids fractions increase (Figure 40). The initial freezing event leads to a solids fraction along the wall of up to 0.80, with the highest solids fraction at the outlet. Once the change in temperature stagnates, the rate of solids freezing tapers, as well. The discontinuity in thermal conductivity at the crust-mantle boundary and increase in the thermal conductivity (Figure 40) of the fluid with increased solids has little effect, because the change in temperature of the outer column is so rapid. The decrease in temperature, and increase in solids fraction, increases the effective viscosity dramatically. Because of this, the velocity in the outer two columns reduces to near-zero as a response of the fluid to the temperature reduction. Despite a basal increase in pressure, the viscosity is large enough ($> 10^5$ Pa·s) to prohibit significant flow on the boundary.

The initial freezing event is accompanied by a simultaneous reduction in flow velocity throughout the conduit. The response of the velocity to the initiation of

Figure 39. Canonical Simulation

Temperature (top), velocity (middle), and pressure (bottom) of an R = 0.30 m conduit of near-peritectic water-ammonia mixture. Only the outer column of fluid freezes. Pressures increase where the fluid freezes, but velocities still reduce to near-zero on the boundary. Velocities increase in the interior columns as temperatures increase.

Figure 40. Canonical Simulation (cont)

Density (top), thermal conductivity (middle), and mass fraction of solids (bottom) of an R = 0.30 m conduit of near-peritectic water-ammonia mixture. Only the outer column of fluid freezes. The solids fraction increases along the conduit wall. Where there are solids, the conductivity and density increase.
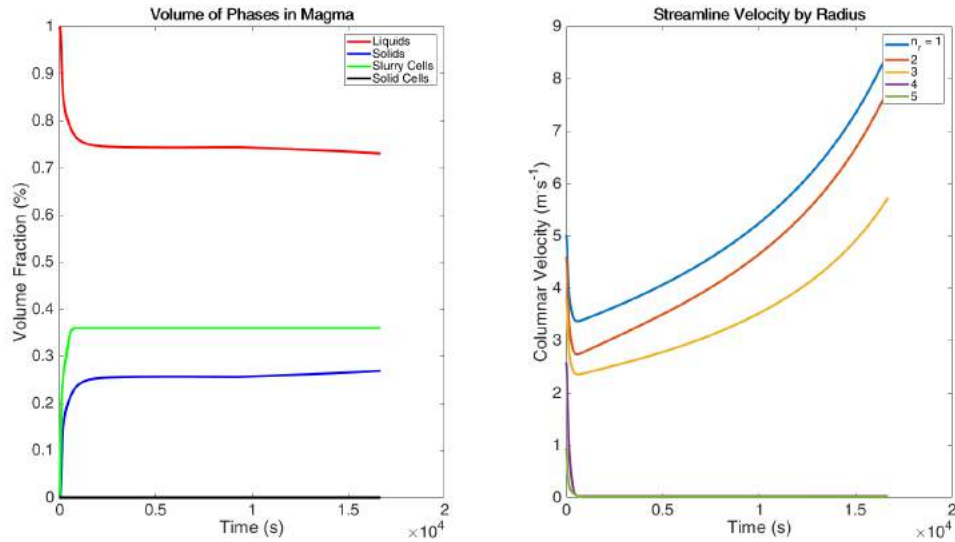
Figure 41. Canonical Simulation (cont)

(Left) Volume fraction of phases within the cryomagma as a whole. The initial freezing event causes about 25% of the magma to solidify, however no single cell reaches complete solidification. The fluid is a slurry anywhere there is solid in the magma. (Right) Density-weighted mean, columnar velocity. The response of the fluid to the freezing event is rapid, after which velocities in the inner three columns rise in a power law fashion.

freezing develops much faster than the entire initial freezing event, with the flow slowing to its minimum average velocity within $\approx$ 600 s (10 minutes) (Figure 41). At this point, the column on the wall has nearly halted, creating a new-no slip boundary for the column at $n_r = 4$. This boundary, combined with the interaction of the fluid in the $n_r = 4$ column with the high viscosity in the outer-most column, reduces the $n_r = 4$ column velocity to near-zero.

The interior of the conduit experiences an *increase* in temperature over time. The reduction in speed of the outer columns increases the stress on the interior columns, because the rate-of-strain tensor, and therefore the stress tensor, are dependent on the gradient of the velocity. The increase in the stress tensor increases the temper-
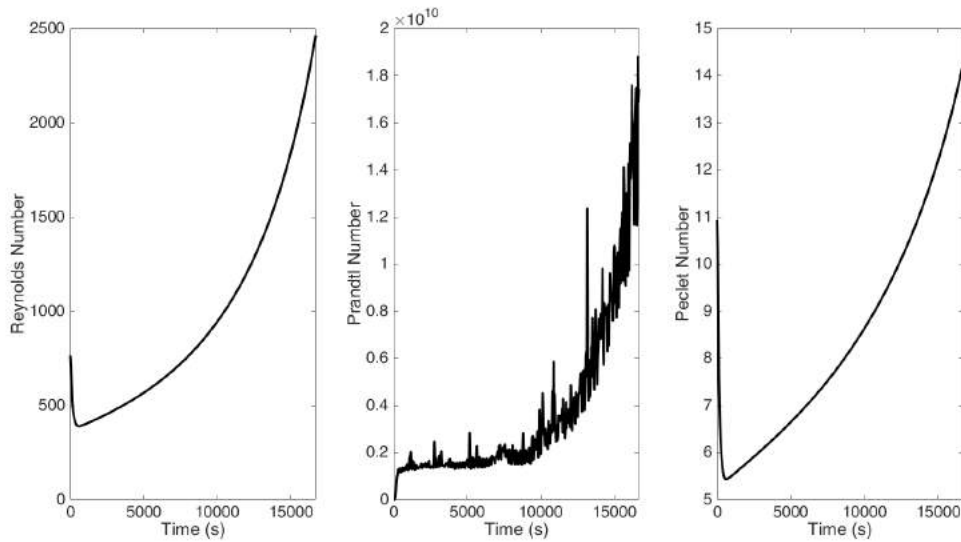
Figure 42. Canonical Simulation (cont)

(Left) Reynolds number, (Middle) Prandtl number, (Right) Peclet number). Reynolds number initially decreases as the flow slows due to the initial freezing event, then increases as velocities in the center of the conduit rise. The simulation is terminated when the Reynolds number suggests turbulent flow. The Prandtl number increases over time, with large spikes in its behavior. This is because the effective viscosity approaches high values as velocities slow causing rapid fluctuations. The Peclet number is much greater than 1 consistent with the viscous dissipation dominating and conduction playing little role.

ature of the fluid, reducing the viscosity. This positive feedback continues to until $t \approx 1.7 \times 10^4$ s (4.6 hours) when the Reynolds number exceeds those suited for laminar flow (Figure 42). The simulation is terminated when the Reynolds number exceeds 2500. This behavior is consistent with the viscous dissipation results from the model validation runs as well as the relatively high Peclet numbers calculated for this system (Figure 42).

The volume of cryomagma that is in the solid phase never exceeds 30% and no individual cell becomes completely crystallized (Figure 41). Over 65% of the cryomagma remains purely liquid, with the remaining fluid being a slurry (defined as

having more than 1% solids by volume). There is a slight upward inflection in the volume of solids that begins just over halfway through the simulation, though the critical Reynolds number is reached (Figure 42), before any significant additions of solids occurs.

4.3.3 Kubrick Mons Simulation

The conduit for the Kubrick Mons simulation has results displayed in Figures 43 - 46. The conduit radius is absurdly small, at $R = 0.02$ m. This is because the base pressure is the same as for the canonical, but the depth to the reservoir is much less leading to a higher pressure gradient. Therefore, laminar flow exists only for very small pipe radii. The initial freezing event is incredibly rapid, with the outer columns at $n_r = 4$ and $n_r = 5$ reaching 0.25 and 0.70 solids fraction, respectively, after $\approx$ 22 s. Thereafter, the temperature on the boundary increases slightly due to viscous dissipation and the solids fraction reduces and remains steady at about 0.22 and 0.60 (Figure 44). Like the canonical, temperatures never reduce below 174 K (Figure 43), so no part of the fluid becomes entirely solid. Viscous dissipation increases the temperature in the center columns of the conduit until about 1000 s ($\approx$ 17 minutes). After this there appears to be a balance between viscous dissipation and conduction.

Pressure in the outer column alternates vertically between low and high values, which is an immediate sign of instability (see below). This can be seen in the alternating low and high values at in the outer column of the fluid, where the viscosity should be sufficient to halt flow (Figure 43). The velocity in the center of the conduit increases as the temperature increases, similar to the canonical. However, the feed-
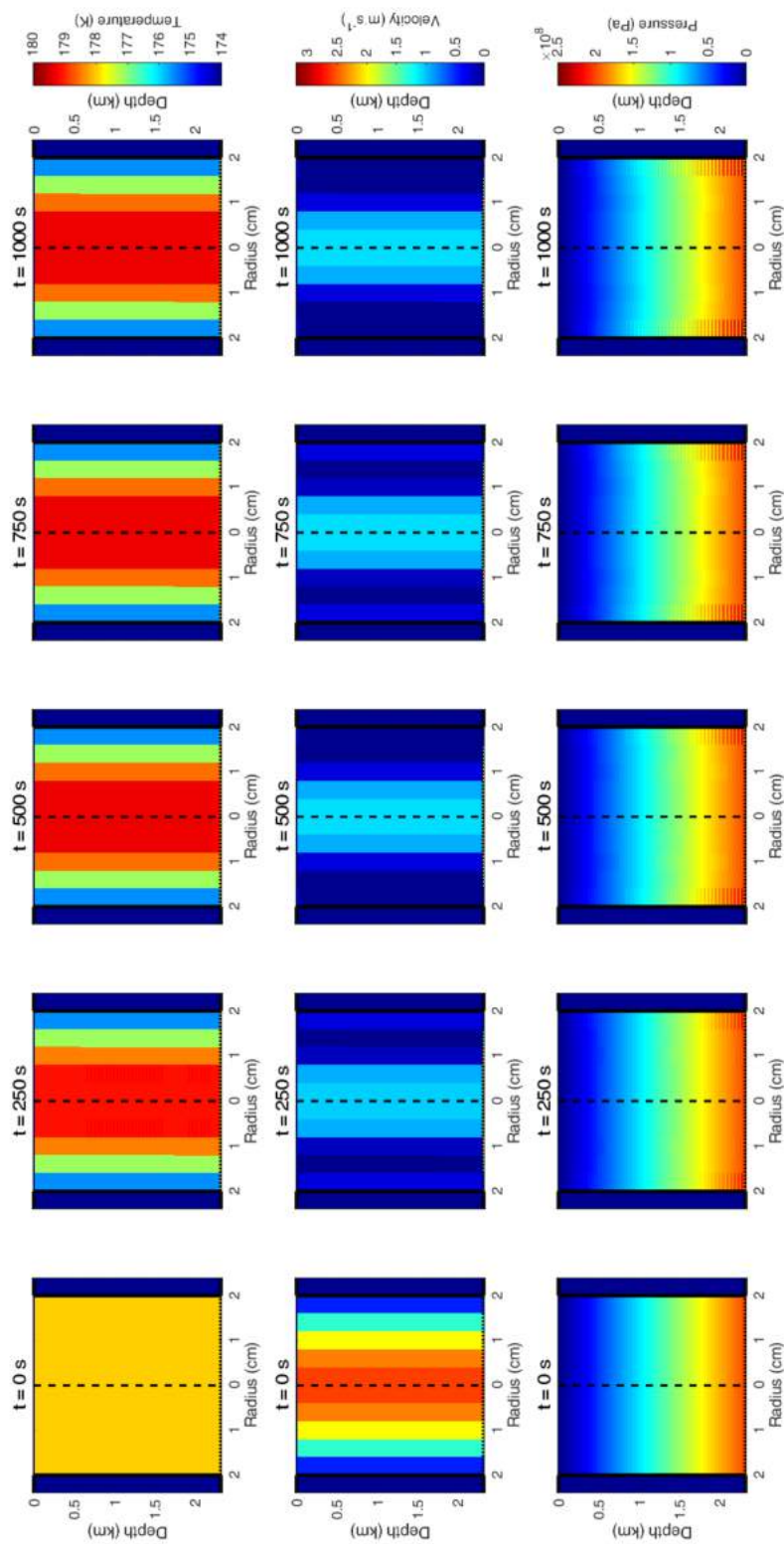
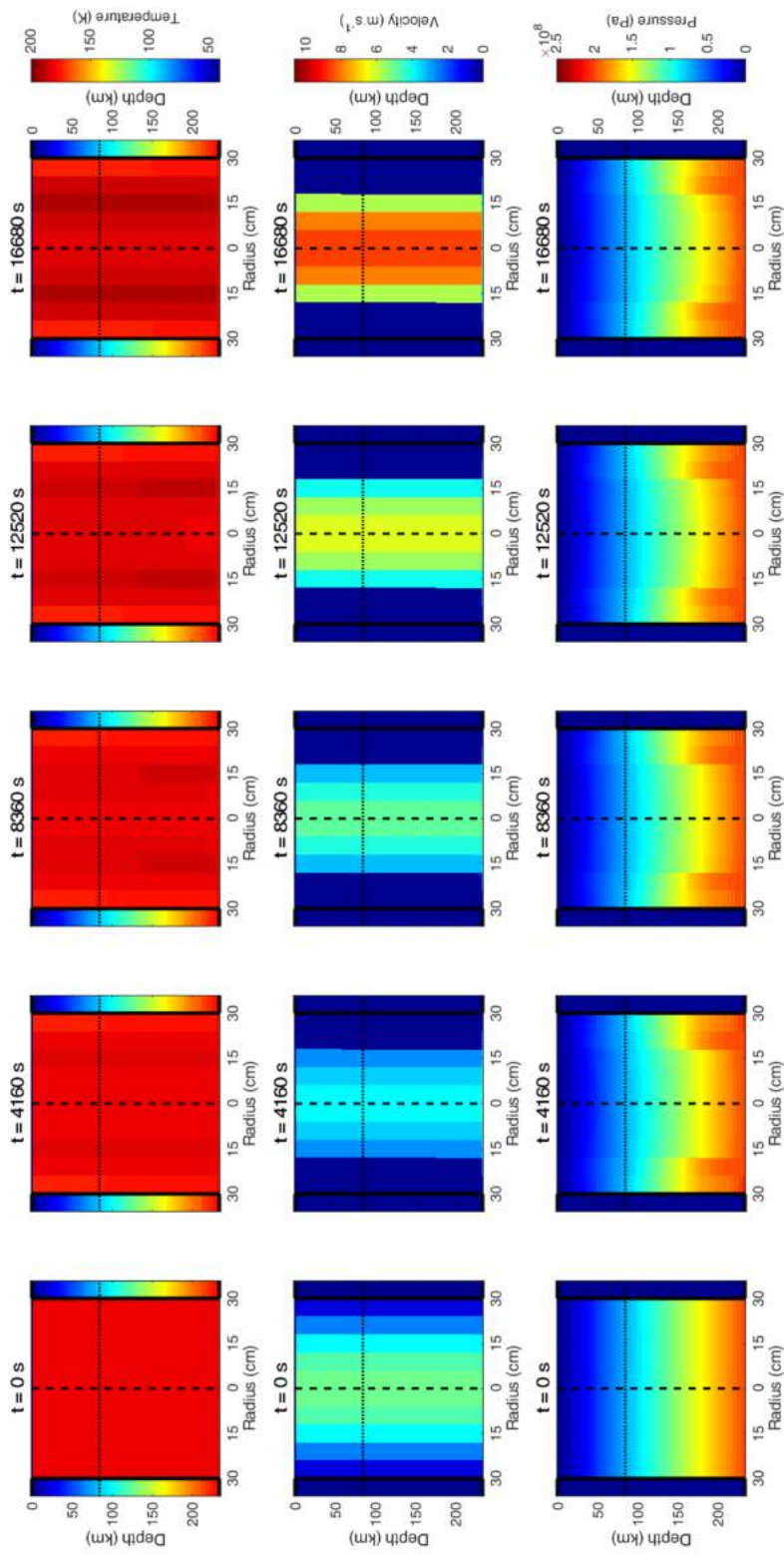Figure 43. Kubrick Mons Simulation

Temperature (top), velocity (middle), and pressure (bottom) of an R = 0.02 m conduit of peritectic water-ammonia mixture. The outer two columns freeze. Pressures increase where the fluid freezes, but velocities still reduce to near-zero on the boundary. Velocities increase in the interior columns as temperatures increase. Steady-state is reached after 1000 s.
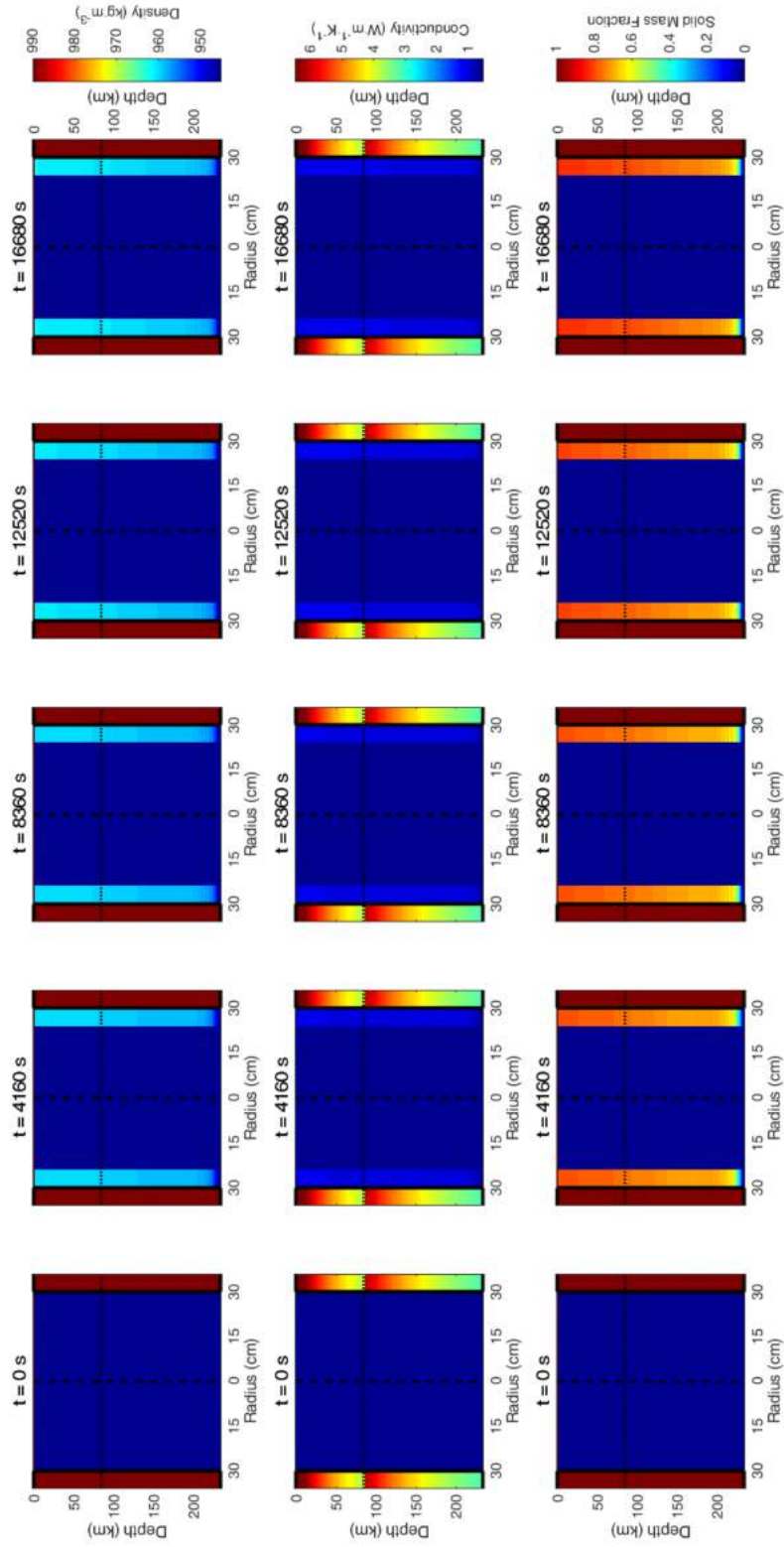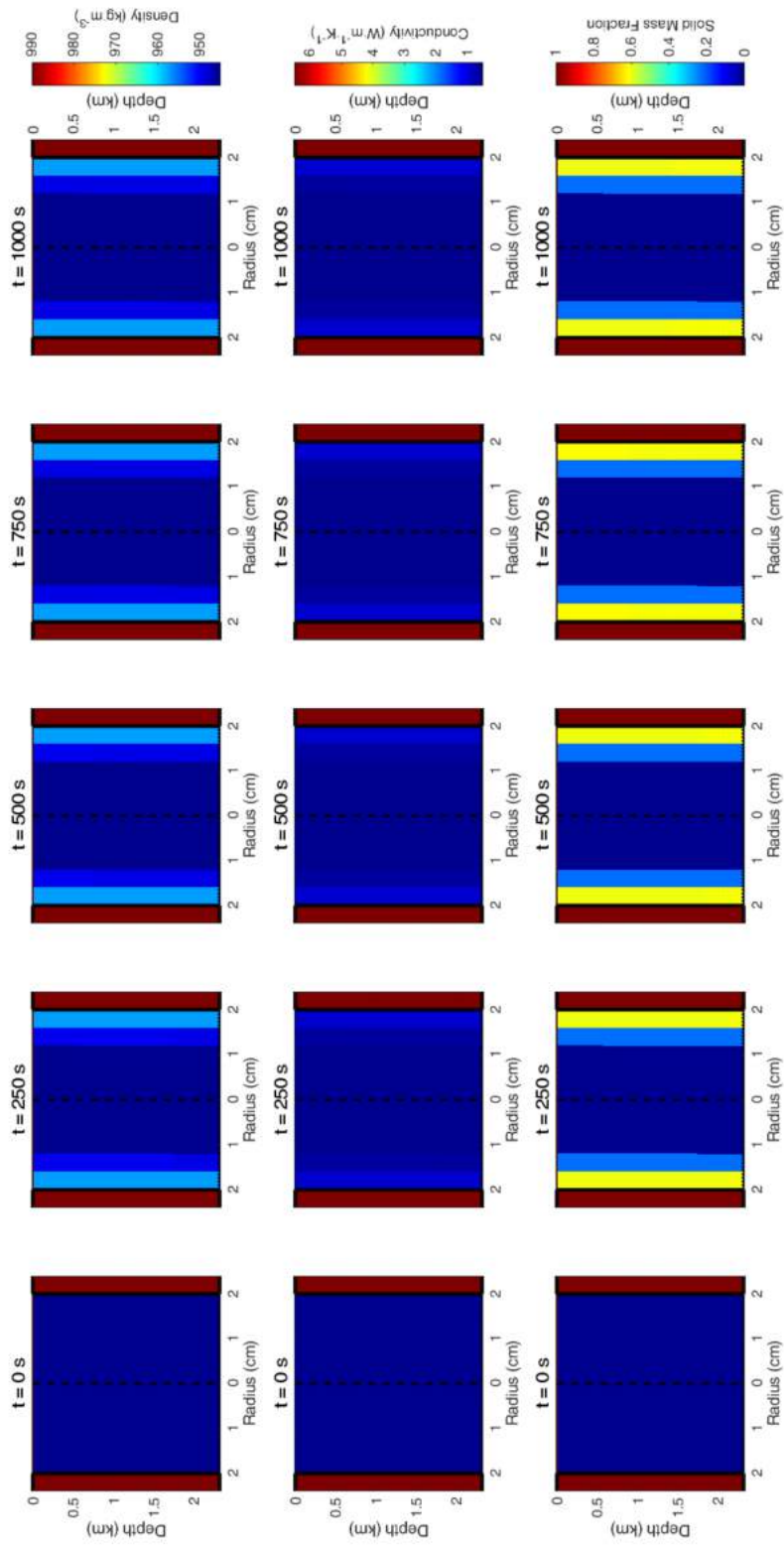
Figure 44. Kubrick Mons Simulation (cont)

Density (top), thermal conductivity (middle), and mass fraction of solids (bottom) of an R = 0.02 m conduit of peritectic water-ammonia mixture. Solids fraction increases in the outer columns and remains constant. Only minor increases in density and conductivity occur where solids freeze out of the liquid.

107
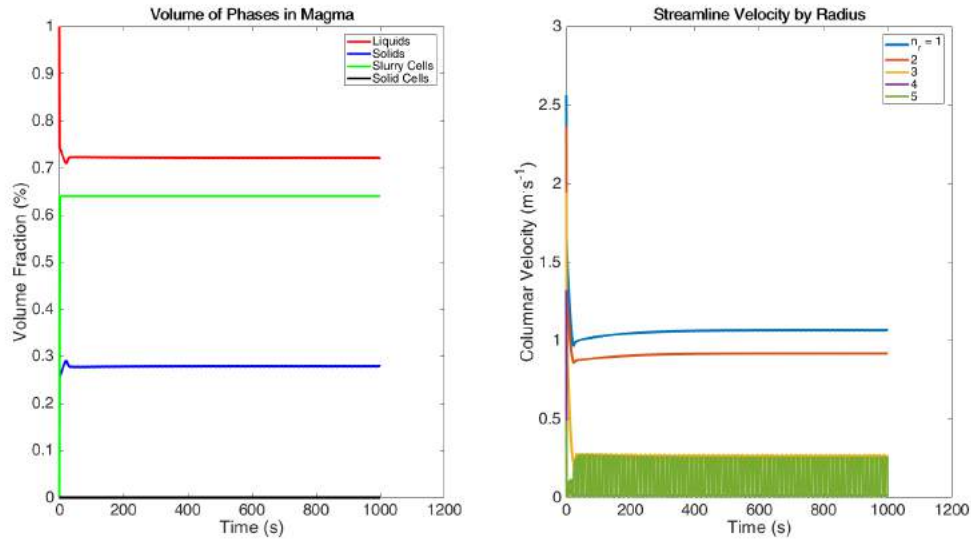
Figure 45. Kubrick Mons Simulation (cont)

(Left) Volume fraction of phases within the cryomagma as a whole. The initial freezing event causes about 30% of the magma to solidify, however no single cell reaches complete solidification. The fluid is a slurry anywhere there is solid in the magma. (Right) Density-weighted mean, columnar velocity. The response of the fluid to the freezing event is rapid, after which velocities in the inner three columns taper off to steady state. The outer column is highly unstable (oscillations) and affects the other columns.

back process witnessed here reaches an approximate steady-state after about 1000 s ($\approx$ 17 minutes).

During the entire simulation instabilities are obvious, especially in the outer columns and to a lesser extent the inner. Velocity on the outer column oscillates between a column-wide ≈ 0.26 and 0 m·s^{-1} and smaller oscilations in column velocity are apparent, as well (Figure 45). The volume of solids in the magma never exceeds 30%, the volume of cells that are slurry accounts for about two-thirds of the magma in the conduit. These percentages change very little after the initial freezing event other than oscillations caused from the boundary instability.
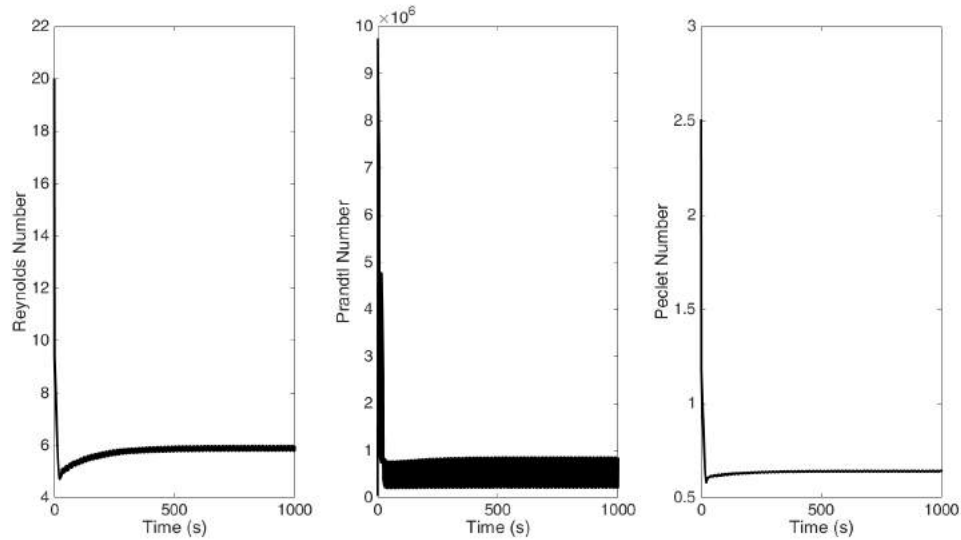
Figure 46. Kubrick Mons Simulation (cont)

(Left) Reynolds number, (Middle) Prandtl number, (Right) Peclet number). All three parameters decrease rapidly with intial freezing of the outer columns, then become steady. Oscillations in the values occur from the instabilities in the fluids on the boundaries. Despite this, on average, the Reynolds number is low. The Peclet number remains at approximate 0.6.

While the Reynolds, Prandtl, and Peclet numbers begin the simulation very high, they immediately reduce with the initial freezing event (Figure 46). We may exclude general turbulent flow as a cause to the instabilities because the Reynolds number is very low. The Peclet number remains well above 1, thus we should expect viscous forces to dominate for this conduit.

4.3.4   Sensitivity Analysis

The least constrained parameters were varied to attempt to find the conditions under which the conduit freezes. These parameters are the radius, thermal conductivity, and initial solids mass fraction. Each parameter was varied independently and

109

applied to the canonical simulation. Radii were changed in steps by 0.05 m, conductivities by 0.5 W·m^{-1}·K^{-1}, and initial solids fraction by 0.05. Peclet numbers were computed for the initial state of the fluid as well as after the intitial freezing event. The reduction in Peclet number can vary by a factor of 2 - 11, due to the decrease in velocity, and increase in thermal conductivity associated with the initial freezing event (see Figures 42 and 46).

The initial freezing event is always halted and viscous dissipation begins heating the fluid down to a radius of $R = 0.20$ m. This complete freezing would not be expected from the initial state of the fluid (Figure 47). However, this is completely consistent with the post-initial-freezing event Peclet number. At this size, the conduit is punctuated by top-down freezing starting from the outer-most column and progressively freezing the interior columns. Surprisingly, the flow is nearly completely impeded when the conduit reaches 100% slurry. In fact, no cell has a mass fraction of solids that exceed about 60%. It takes only an effective viscosity of ≈ 30 Pa·s^{-1} across the entire fluid for the rate of flow to reduce to near zero. This is reached at about 3.5×10^4 s (9.7 hours). There is instability on the wall boundary that forces velocities to increase where there is high mass fraction of solids (see §4.4), similar to that seen in the Kubrick Mons simulation, but to a lesser degree. This forces the interior flow to never reach a zero velocity, but would if the instabilities on the fringes were absent.

Similarly, the conduit remains open to flow, and viscous dissipation dominates until the initial thermal conductivity of the liquid is set to $k = 2.0$ W·m^{-1}·K^{-1}. Again, the Peclet number for the initial state of this simulation is over 1 prior to the initial freezing event, but afterward is completely consistent with heat diffusion dominating
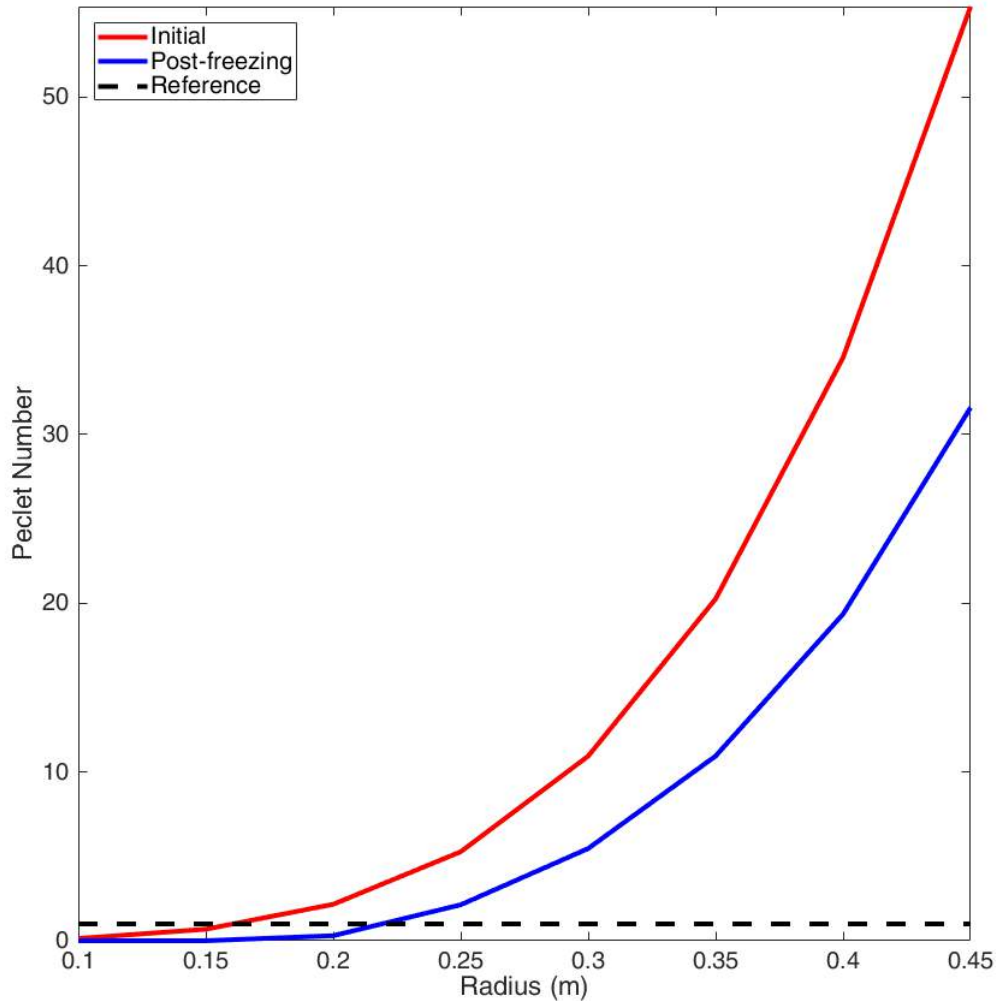
Figure 47. Peclet Number as a Function of Pipe Radius

Based on the initial state (red) Peclet numbers would suggest conduits of larger than 0.15 m remain open. However, examination of the simulations showed that a conduit of the 0.20 m froze to slurry throughout on a short timescale. This is consistent with the Peclet number after the cells on the wall boundary froze (blue). Reference (black) is at Pe=1.
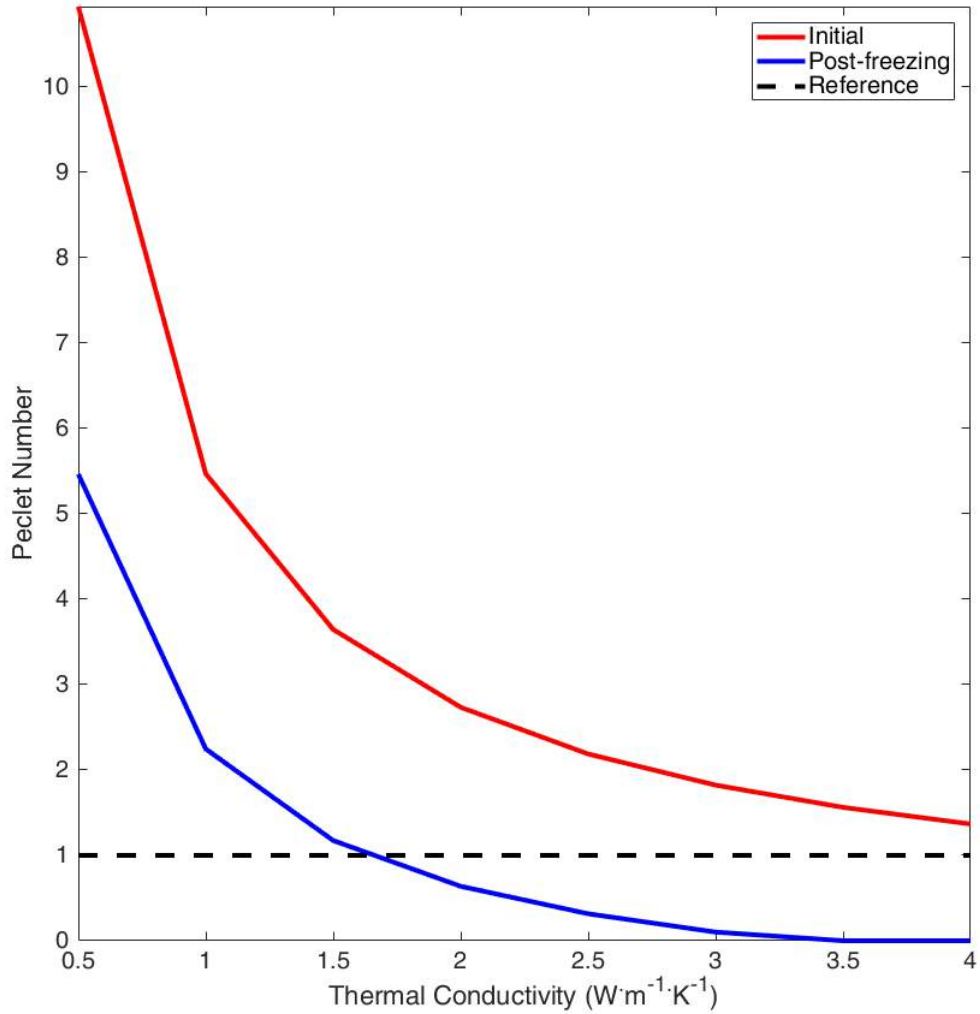
Figure 48. Peclet Number as a Function of Fluid Thermal Conductivity

Initial state Peclet numbers (red) suggest that freezing should not occur for thermal conductivities less than 4 W·m^{-1}·K^{-1}. However, freezing is found to complete stoppage of flow occurs at a thermal conductivity of 2.0 W·m^{-1}·K^{-1}, where the post-initial freezing event Peclet number reduces below 1. Reference (black) is at Pe=1.

(Figure 48). Freezing occurs in a nearly identical manner to the $R = 0.20$ m simulation, with impedance of flow occurring when the fluid has an effective viscosity of about $30\,\mathrm{Pa \cdot s^{-1}}$. The timing flow stoppage is similarly identical, occurring at 3.5×10^4 s (9.7 hours). This simulation likewise has instabilities along the wall boundary that force the center of the conduit to never truly halt.

Introduction of uniform water ice fraction of $X_s = 0.10$ is sufficient to halt flow after, again, 3.5×10^4 s (9.7 hours). The freezing of these is consistent with the post-initial-freezing event Peclet number (Figure 49). Instabilities in this simulation are much larger than the previous, because the higher initial solids fraction increases the conductivity and viscosity, and reduces the initial flow speed, allowing faster freezing on the boundary and increased solids production in the initial freezing event. Once a high degree of solids are introduced instabilities propagate. Viscous dissipation warms the fluid at the boundaries enough to reduce the solids fraction to about 60%, but the instabilities continue to propagate.

4.4   Discussion

4.4.1   Model Limitations

The model appears to be highly sensitive to the radius of the conduit, as freezing occurs at just below the canonical radius and at a radius of $R = 0.45$ m the flow is initially turbulent. The Kubrick Mons simulation is even more sensitive to this, with lower radii becoming more unstable and higher radii rapidly approaching turbulence. This model cannot sufficiently simulate this flow regime, however turbulent dissipa-
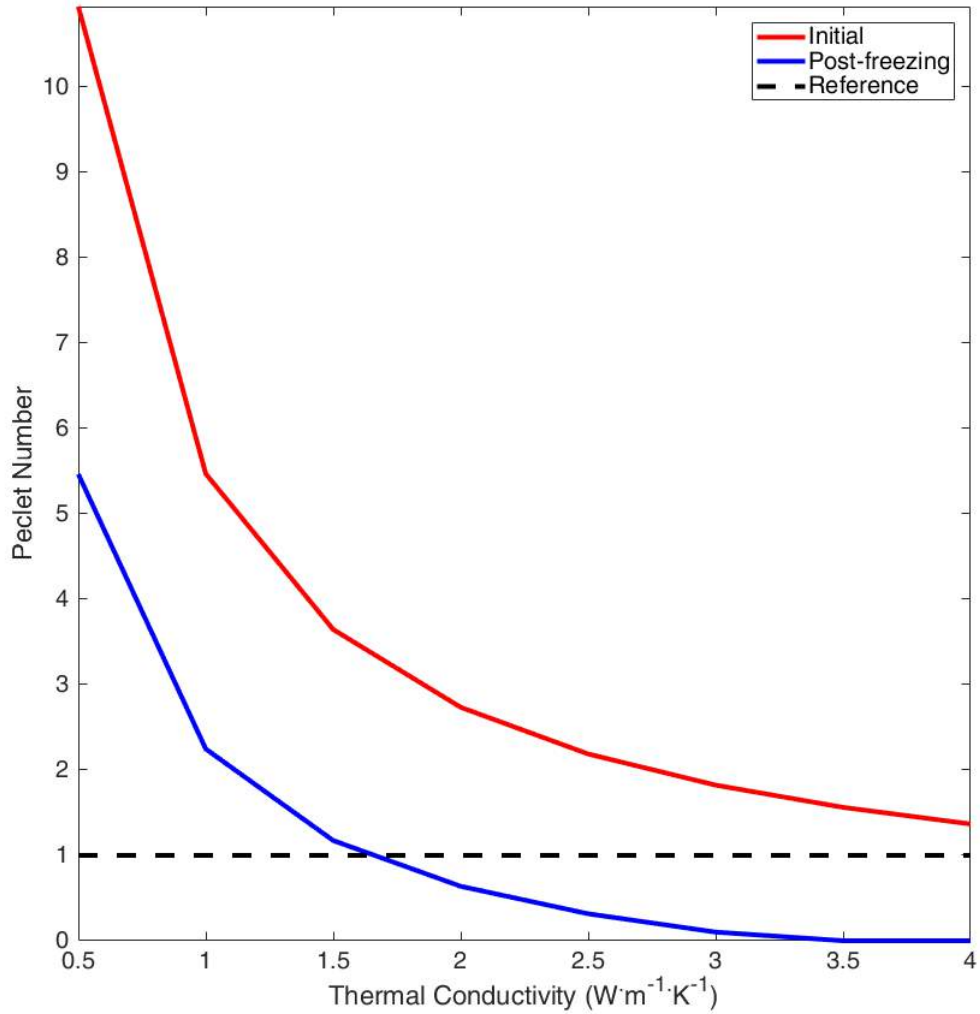
Figure 49. Peclet Number as a Function of Initial Solids Mass Fraction

Heat diffusion dominates according to the initial state Peclet numbers (red) at initial solids mass fraction of greater than 0.10. The post-freezing Peclet number (blue) for this mass fraction is much less than one and consistent with the freezing of the simulation. Reference (black) is at Pe=1.

tion of heat could dramatically increase the effective conductivity of the fluid and cooling could then happen pseudo-spontaneously thereafter.

The canonical model results suggest that the low thermal conductivity and high viscous dissipation are responsible for keeping the conduit open. An increase in the fluid conductivity by a factor of 4 is enough to promote long-term freezing. However, given the low conductivity of liquids at these temperatures, the liquid mixture would require vastly different thermal properties than its constituents to have a substantially high conductivity. This seems unreasonable. Thus, the only method of acquiring conductivities sufficiently high to promote freezing would be to add solids. To obtain a thermal conductivity this high would require the fluid to be about 60% water ice by volume at 180 K. This would make the viscosity far too high to allow for rapid fluid flow.

The oscillations of velocity on the outer-most radial cells is likely due to initiation of secondary flows from freezing that are not representable with the model presented as is. This effect was noted by Costa and Macedonio (2003). This effect only occurs when there are a relatively high amount of solids and the flow approaches zero. This is because the power law stress tensor that represents the solids is inversely proportional to the gradient in the velocity. Thus, when there are low solids the Newtonian portion of the stress tensor still dominates and instabilities are not seen. When the solids fraction is high, the power law component becomes important, but simultaneously brings the flow to low speeds due to the high effective viscosity (needing only about a mass fraction of 10%). This reduces the velocity to near zero in some places, forcing the stress tensor and effective viscosity to approach infinity, producing the instabilities observed. Costa and Macedonio (2003) argue that this is likely not a real effect, rather a consequence of the constraints placed on the flow that produce local

instabilities even at low Reynolds number. The flow in the column at $n_r = 4$ stops once the outer-most column initially freezes and remains stationary. Therefore, it is more likely that the boundary cells sustain a velocity of ≈ 0 m·s^{-1}.

The increase in velocity after the initial freezing event is caused by a positive feedback loop coined "thermal runaway" by Costa and Macedonio (2003). The increase in the divergence in the stress tensor where the fluid experiences high velocity gradients increases the viscous dissipation, which increases the temperature, reduces the viscosity, and increases the velocity. It is not clear if the thermal runaway here is fictitious. The sensitivity analysis on the thermal conductivity suggests that the low liquid conductivity and high viscous dissipation is responsible for thermal runaway. The flow in the interior is consistent, well-behaved, and also, not near the boundary. With a thermal conductivity of $k = 2.0$ W·m^{-1}·K^{-1} the entire conduit begins freezing rapidly, but has apparent instabilities as the mass fraction of solids increases in the slurry. These instabilities make long-term simulations where high solids fractions occur impossible, but cases like these likely freeze completely, because the thermal conductivity increases as solids condense from the melt.

The variation in materials of the boundary, itself, appear to be irrelevant, because the timescale for freezing along the wall is very rapid. For bodies that are chiefly composed of water ice, it seems to only matter that they are cold at the surface. The length of the pipe is similarly irrelevant for understanding whether cryomagmas can ascend to the surface before freezing. The length dictates only the pressure at the base, so longer pipes will generate sustained conduits of larger radii. Using the length and radii for the freezing limit of the canonical and the Kubrick Mons simulations I can estimate a length-to-radius ratio. This appears to follow the relationship of

approximately 7.8×10^{-4} m·km^{-1} for radius per length. So, a 1000 km conduit would still only be 78 cm in radius and have persistent flow!

The rheological model employed here for the two-phase fluid is not conducive to these simulations, resulting in instabilities on the boundaries of certain conduits. Because the velocities in the conduit become close to zero with even a marginal solids mass fraction, it is likely unnecessary to use a stress-dependent rheological model for the solid. A Newtonian stress tensor with a slurry viscosity dependent on the solids mass fraction is likely entirely sufficient for this model and could possibly return more stable results, without any loss of accuracy.

4.4.2   Implications for Kubrick Mons

Due to the unstable nature of this system, it may call the results produced here into question. Nevertheless I shall utilize these results to speculate about Kubrick Mons. These speculations should be taken with healthy skepticism, due to the numerical instability present within the code.

Using the velocity of the inner three columns when the outer column has an average velocity of zero, I compute the discharge rate. This can simply be computed as $Q = \rho A v$ for the mass discharge and $Q = A v$ for the volume discharge, where ρ is the density, A is the cross-sectional area, and v is the velocity. These compute to 2.2×10^{-1} kg·s^{-1} and 2.4×10^{-4} m^3·s^{-1}. These are remarkably low compared to traditional earth eruption styles, consistent with Strombolian effusion rates on Earth.

These rates can be used to estimate the maximum emplacement timescale for the cryovolcano. Taking Kubrick Mons to be a cone with a radius of 17 km and a height between 3 and 4 km, I compute the volume to be between 908 km^3 and

1211 km³. Dividing this value by the volume discharge rate from above and applying some dimensional analysis yields an upper limit formation timescale of 122 – 163 Myr. Desch and Neveu (2017) suggest freezing of a pluton this distance from the surface would occur in 0.5 Myr and discharge would be on the order of 70 kg·s^{-1}. The limitations of the model presented here likely lead to an unrealistic representation of the conduit that fed Kubrick Mons. However, these values bracket the possible timescales and effusion rates for this cryovolcano. If it did form over 150 Myr, re-melting or recharge of the magma chamber feeding the eruption would be necessary. With the sustainability of conduits shown from the canonical simulation, it is not unfeasible to imagine transport of cryomagma from the lower mantle to a chamber near the surface.

4.5 Conclusion

Cryovolcanic conduits on a Charon-like body remain unfrozen down to a radius of $R = 0.20$ m, though these radii, in general, are exceptionally small. It seems unrealistic for conduits on less than the meter scale to persist unimpeded through such hundreds of kilometers of mantle and crust, though I have shown that it is hypothetically possible. Conduits need not be cylindrical, nor perfectly vertical.

Estimates made on the scaling of conduit length-to-radius seem to suggest that it would not be difficult to produce sustainable cryovolcanic conduits to any depth, provided the body has a sufficiently cold surface and overpressured cryomagma. Therefore cryovolcanic features could be expected on all medium-sized KBOs.

The upper limit timescales for the formation of Kubrick Mons are estimated to be 122 - 163 Myr. This is many times longer than the timescale of formation from

Desch and Neveu (2017), assuming a single pluton freezes and discharges entirely through one small conduit. It is unlikely that the conduit of Kubrick Mons was as small as that proposed by the model, but given this steady-state case, could indicate that the source for Kubrick Mons was continually recharged or that multiple conduits were responsible for the emplacement of Kubrick Mons.

Chapter 5

OUTLOOK

The results of Chapters 2 and 3 indicate the need for Mars polar studies at smaller scales. The range of values and detail of behaviors in regions smaller than the footprint of TES, GRS, MONS, and MCS are surprising. While these types of studies offer insight into only very localized, perhaps even unique regions, and require much more labor time to reveal global relationships and trends, they appear absolutely necessary.

The implementation of the excellent suite of instruments on board Mars Odyssey, Mars Reconnaissance Orbiter, and Mars Express has been shown to be integral to characterizing polar ice at these scales. THEMIS and HiRISE continue to operate and thus should provide years of monitoring data conducive to extending the studies done in chapter 2 and 3 to other areas of the polar caps, both north and south.

Provided similar data sets exist, joining CMA results with CRISM calibrated radiance and grain-size modeling could provide more information on the physical states of seasonal ice on the poles during sublimation. Improved THEMIS thermal inertia maps could be utilized to correlate the temporal behaviors. HRSC has nearly mapped the entire surface of Mars, thus in any region of ice being studied, it should be possible to accompany it with a DTM to study seasonal features with the orientation of the surface. HiRISE should continue to be used despite the large error in its albedo because if boulders are present within images, density can be derived revealing even greater detail about these deposits. This is not possible with any other instrument.

Of particular interest are studies of these varieties in the Cryptic region. No

relationships to the behavior of ice to the surface, nor small scale CMA have been successfully done in the Cryptic region. Application of these techniques at small scales within this region may finally shed light onto the reason of its existence.

The instabilities in the model in Chapter 4 suggest that the rheological model employed here is insufficient, and likely unnecessary, to model these types of systems. The model should be simplified now that it has been shown that even moderate viscosities are enough to impede flow for conduits on KBOs. This would likely take the form of a modified Einstein-Roscoe equation to compute the viscosity and an assumed Newtonian stress tensor.

The assumption of laminar flow appears to be inadequate to fully characterize cryovolcanic conduits with ammonia-water liquids, because the viscous dissipation is so large. A fuller range of pipe radii could be explored by implementing steady-state considerations for turbulent flow using, e.g., a Darcy-Weisbach formulation. A study of this variety is necessary to understand the rate of cooling of the fluid under turbulent conditions. If cooling associated with turbulence is high enough to freeze the conduit, then perhaps only cracks that satisfy laminar flow constraints remain open on these bodies. This would imply that any cryovolcanism on medium sized KBOs is fed by fairly small pipes with low effusion rates and long timescales of formation.

Overall, continued study of these dynamic systems will elucidate the processes and impacts of ices on the planetary bodies.

REFERENCES

Aharonson, O., M. T. Zuber, D. E. Smith, G. A. Neumann, W. C. Feldman and T. H. Prettyman, "Depth, distribution, and density of CO_2 deposition on Mars", Journal of Geophysical Research (Planets) **109**, E05004 (2004).

Appéré, T., B. Schmitt, Y. Langevin, S. Douté, A. Pommerol, F. Forget, A. Spiga, B. Gondet and J.-P. Bibring, "Winter and spring evolution of northern seasonal deposits on Mars from OMEGA on Mars Express", Journal of Geophysical Research (Planets) **116**, E05001 (2011).

Barucci, M. A., F. Merlin, A. Guilbert, C. de Bergh, A. Alvarez-Candal, O. Hainaut, A. Doressoundiram, C. Dumas, T. Owen and A. Coradini, "Surface composition and temperature of the tno orcus", Astron. Astrophys. **479**, L13–L16 (2008).

Battalio, M. and H. Wang, "The Aonia-Solis-Valles dust storm track in the southern hemisphere of Mars", Icarus **321**, 367–378 (2019).

Benson, J. L. and P. B. James, "Yearly comparisons of the martian polar caps: 1999 2003 Mars Orbiter Camera observations", Icarus **174**, 513–523 (2005).

Beyer, R. A., F. Nimmo, W. B. Mckinnon, J. M. Moore, R. P. Binzel, J. W. Conrad, A. Cheng, K. Ennico, T. R. Lauer, C. B. Olkin, S. Robbins, P. Schenk, K. Singer, J. R. Spencer, S. A. Stern, H. A. Weaver, L. A. Young and A. M. Zangari, "Charon tectonics", Icarus **287**, 161–174 (2017).

Bibring, J.-P., Y. Langevin, A. Gendrin, B. Gondet, F. Poulet, M. Berthé, A. Soufflot, R. Arvidson, N. Mangold, J. Mustard, P. Drossart, O. M. E. G. A. Team, S. Erard, O. Forni, M. Combes, T. Encrenaz, T. Fouchet, R. Merchiorri, G. Belluci, F. Altieri, V. Formisano, G. Bonello, F. Capaccioni, P. Cerroni, A. Coradini, S. Fonti, V. Kottsov, N. Ignatiev, V. Moroz, D. Titov, L. Zasova, M. Mangold, P. Pinet, S. Douté, B. Schmitt, C. Sotin, E. Hauber, H. Hoffmann, R. Jaumann, U. Keller, T. Duxbury and F. Forget, "Mars Surface Diversity as Revealed by the OMEGA/Mars Express Observations", Science **307**, 1576–1581 (2005).

Bonev, B. P., G. B. Hansen, D. A. Glenar, P. B. James and J. E. Bjorkman, "Albedo models for the residual south polar cap on Mars: Implications for the stability of the cap under near-perihelion global dust storm conditions", Planetary and Space Science **56**, 181–193 (2008).

Bonev, B. P., P. B. James, J. E. Bjorkman and M. J. Wolff, "Regression of the Mountains of Mitchel polar ice after the onset of a global dust storm on Mars", Geophysical Research Letters **29**, 2017 (2002).

Boynton, W. V., W. C. Feldman, I. G. Mitrofanov, L. G. Evans, R. C. Reedy, S. W. Squyres, R. Starr, J. I. Trombka, C. D'Uston, J. R. Arnold, P. A. J. Englert, A. E. Metzger, H. Wänke, J. Brückner, D. M. Drake, C. Shinohara, C. Fellows, D. K. Hamara, K. Harshman, K. Kerry, C. Turner, M. Ward, H. Barthe, K. R. Fuller, S. A. Storms, G. W. Thornton, J. L. Longmire, M. L. Litvak and A. K. Ton'chev, "The Mars Odyssey Gamma-Ray Spectrometer Instrument Suite", Space Science Reviews **110**, 37–83 (2004).

Brown, A. J., W. M. Calvin, P. C. McGuire and S. L. Murchie, "Compact Reconnaissance Imaging Spectrometer for Mars (CRISM) south polar mapping: First Mars year of observations", Journal of Geophysical Research (Planets) **115**, E00D13 (2010).

Brown, A. J., W. M. Calvin and S. L. Murchie, "Compact Reconnaissance Imaging Spectrometer for Mars (CRISM) north polar springtime recession mapping: First 3 Mars years of observations", Journal of Geophysical Research (Planets) **117**, E00J20 (2012).

Brown, A. J., S. Piqueux and T. N. Titus, "Interannual observations and quantification of summertime H_2O ice deposition on the Martian CO_2 ice south polar cap", Earth and Planetary Science Letters **406**, 102–109 (2014).

Calvin, W. M., B. A. Cantor and P. B. James, "Interannual and seasonal changes in the south seasonal polar cap of Mars: Observations from MY 28-31 using MARCI", Icarus **292**, 144–153 (2017).

Calvin, W. M., P. B. James, B. A. Cantor and E. M. Dixon, "Interannual and seasonal changes in the north polar ice deposits of Mars: Observations from MY 29-31 using MARCI", Icarus **251**, 181–190 (2015).

Canup, R. M., "On a Giant Impact Origin of Charon, Nix, and Hydra", The Astronomical Journal **141**, 35 (2011).

Christensen, P. R., J. L. Bandfield, V. E. Hamilton, S. W. Ruff, H. H. Kieffer, T. N. Titus, M. C. Malin, R. V. Morris, M. D. Lane, R. L. Clark, B. M. Jakosky, M. T. Mellon, J. C. Pearl, B. J. Conrath, M. D. Smith, R. T. Clancy, R. O. Kuzmin, T. Roush, G. L. Mehall, N. Gorelick, K. Bender, K. Murray, S. Dason, E. Greene, S. Silverman and M. Greenfield, "Mars Global Surveyor Thermal Emission Spectrometer experiment: Investigation description and surface science results", Journal of Geophysical Research **106**, 23823–23872 (2001).

Christensen, P. R., B. M. Jakosky, H. H. Kieffer, M. C. Malin, H. Y. McSween, Jr., K. Nealson, G. L. Mehall, S. H. Silverman, S. Ferry, M. Caplinger and M. Ravine, "The Thermal Emission Imaging System (THEMIS) for the Mars 2001 Odyssey Mission", Space Science Reviews **110**, 85–130 (2004).

Colaprete, A., J. R. Barnes, R. M. Haberle, J. L. Hollingsworth, H. H. Kieffer and T. N. Titus, "Albedo of the south pole on Mars determined by topographic forcing of atmosphere dynamics", Nature **435**, 184–188 (2005).

Cook, J. C., S. J. Desch, T. L. Roush, C. A. Trujillo and T. R. Geballe, "Near-infrared spectroscopy of charon: Possible evidence for cryovolcanism on kuiper belt objects", Astrophysical Journal **663**, 1406–1419 (2007).

Costa, A. and G. Macedonio, "Viscous heating in fluids with temperature-dependent viscosity: implications for magma flows", Nonlinear Processes in Geophysics **10**, 6, 545–555, URL https://doaj.org/article/f7bc402f7a2b46168d58d3bb203bf8dd (2003).

Crawford, G. D. and D. J. Stevenson, "Gas-driven water volcanism and the resurfacing of europa", Icarus **73**, 1, 66 – 79 (1988).

Croft, S. K., J. I. Lunine and J. Kargel, "Equation of state of ammonia-water liquid - derivation and planetological applications", Icarus **73**, 279–293 (1988).

Cruikshank, D. P., W. M. Grundy, F. E. DeMeo, M. W. Buie, R. P. Binzel, D. E. Jennings, C. B. Olkin, J. W. Parker, D. C. Reuter, J. R. Spencer, S. A. Stern, L. A. Young and H. A. Weaver, "The surface compositions of Pluto and Charon", Icarus **246**, 82–92 (2015).

Cull, S., R. E. Arvidson, M. Mellon, S. Wiseman, R. Clark, T. Titus, R. V. Morris and P. McGuire, "Seasonal H_2O and CO_2 ice cycles at the Mars Phoenix landing site: 1. Prelanding CRISM and HiRISE observations", Journal of Geophysical Research (Planets) **115**, E00D16 (2010).

Dalle Ore, C. M., S. Protopapa, J. C. Cook, W. M. Grundy, D. P. Cruikshank, A. J. Verbiscer, K. Ennico, C. B. Olkin, S. A. Stern, H. A. Weaver, L. A. Young and N. H. S. Team, "Ices on Charon: Distribution of H_2O and NH_3 from New Horizons LEISA observations", Icarus **300**, 21–32 (2018).

DeMeo, F. E., C. Dumas, J. C. Cook, B. Carry, F. Merlin, A. J. Verbiscer and R. P. Binzel, "Spectral variability of Charon's 2.21-μm feature", Icarus **246**, 213–219 (2015).

Desch, S. J., "Density of Charon formed from a disk generated by the impact of partially differentiated bodies", Icarus **246**, 37–47 (2015).

Desch, S. J., J. C. Cook, T. C. Doggett and S. B. Porter, "Thermal evolution of kuiper belt objects, with implications for cryovolcanism", Icarus **202**, 694–714 (2009).

Desch, S. J. and M. Neveu, "Differentiation and cryovolcanism on Charon: A view before and after New Horizons", Icarus **287**, 175–186 (2017).

Dumas, C., R. J. Terrile, R. H. Brown, G. Schneider and B. A. Smith, "Hubble Space Telescope NICMOS Spectroscopy of Charon's Leading and Trailing Hemispheres", The Astronomical Journal **121**, 1163–1170 (2001).

Durham, W. B., S. H. Kirby and L. A. Stern, "Flow of ices in the ammonia-water system", Journal of Geophysical Research **98**, 17667–17682 (1993).

Eluszkiewicz, J., "On the microphysical state of the surface of Triton", Journal of Geophysical Research **96**, 19 (1991).

Eluszkiewicz, J., "On the microphysical state of the Martian seasonal caps", Icarus **103**, 43–48 (1993).

Eluszkiewicz, J., J.-L. Moncet, T. N. Titus and G. B. Hansen, "A microphysically-based approach to modeling emissivity and albedo of the martian seasonal caps", Icarus **174**, 524–534 (2005).

Fagents, S. A., "Considerations for effusive cryovolcanism on europa: The post-galileo perspective", Journal of Geophysical Research: Planets **108**, E12, n/a–n/a, 5139 (2003).

Feistel, R. and W. Wagner, "A New Equation of State for H_2O Ice Ih", Journal of Physical and Chemical Reference Data **35**, 1021–1047 (2006).

Feldman, W. C., T. H. Prettyman, W. V. Boynton, J. R. Murphy, S. Squyres, S. Karunatillake, S. Maurice, R. L. Tokar, G. W. McKinney, D. K. Hamara, N. Kelly and K. Kerry, "CO_2 frost cap thickness on Mars during northern winter and spring", Journal of Geophysical Research (Planets) **108**, 5103 (2003).

Fergason, R. L., P. R. Christensen and H. H. Kieffer, "High-resolution thermal inertia derived from the Thermal Emission Imaging System (THEMIS): Thermal model and applications", Journal of Geophysical Research (Planets) **111**, E12004 (2006).

Fortes, A. D., I. G. Wood, J. P. Brodholt and L. Vočadlo, "The structure, ordering and equation of state of ammonia dihydrate (nh $_3$ 2h $_2$o)", Icarus **162**, 59–73 (2003).

Geissler, P., "Chapter 44 - cryovolcanism in the outer solar system", in "The Encyclopedia of Volcanoes", pp. 763–776 (2015).

Grundy, W., M. Buie, J. Stansberry, J. Spencer and B. Schmitt, "Near-infrared spectra of icy outer solar system surfaces: Remote determination of h2o ice temperatures", Icarus **142**, 2, 536 – 549 (1999).

Grundy, W. M., R. P. Binzel, B. J. Buratti, J. C. Cook, D. P. Cruikshank, C. M. Dalle Ore, A. M. Earle, K. Ennico, C. J. A. Howett, A. W. Lunsford, C. B. Olkin, A. H. Parker, S. Philippe, S. Protopapa, E. Quirico, D. C. Reuter, B. Schmitt, K. N. Singer, A. J.

Verbiscer, R. A. Beyer, M. W. Buie, A. F. Cheng, D. E. Jennings, I. R. Linscott, J. W. Parker, P. M. Schenk, J. R. Spencer, J. A. Stansberry, S. A. Stern, H. B. Throop, C. C. C. Tsang, H. A. Weaver, G. E. Weigle and L. A. Young, "Surface compositions across Pluto and Charon", Science **351**, aad9189 (2016).

Haberle, R. M., F. Forget, A. Colaprete, J. Schaeffer, W. V. Boynton, N. J. Kelly and M. A. Chamberlain, "The effect of ground ice on the Martian seasonal CO_2 cycle", Planetary and Space Science **56**, 251–255 (2008).

Haberle, R. M., B. Mattingly and T. N. Titus, "Reconciling different observations of the CO_2 ice mass loading of the Martian north polar cap", Geophysical Research Letters **31**, L05702 (2004).

Hansen, C. J., S. Byrne, G. Portyankina, M. Bourke, C. Dundas, A. McEwen, M. Mellon, A. Pommerol and N. Thomas, "Observations of the northern seasonal polar cap on Mars: I. Spring sublimation activity and processes", Icarus **225**, 881–897 (2013).

Hansen, C. J., L. Esposito, A. I. F. Stewart, J. Colwell, A. Hendrix, W. Pryor, D. Shemansky and R. West, "Enceladus' Water Vapor Plume", Science **311**, 1422–1425 (2006).

Hansen, C. J., N. Thomas, G. Portyankina, A. McEwen, T. Becker, S. Byrne, K. Herkenhoff, H. Kieffer and M. Mellon, "HiRISE observations of gas sublimation-driven activity in Mars' southern polar regions: I. Erosion of the surface", Icarus **205**, 283–295 (2010).

Hansen, G. B., "Control of the radiative behavior of the Martian polar caps by surface CO_2 ice: Evidence from Mars Global Surveyor measurements", Journal of Geophysical Research **104**, 16471–16486 (1999).

Hansen, G. B., "Ultraviolet to near-infrared absorption spectrum of carbon dioxide ice from 0.174 to 1.8 μm", Journal of Geophysical Research (Planets) **110**, E11003 (2005).

Hayne, P. O., D. A. Paige and N. G. Heavens, "The role of snowfall in forming the seasonal ice caps of Mars: Models and constraints from the Mars Climate Sounder", Icarus **231**, 122–130 (2014).

Hayne, P. O., D. A. Paige, J. T. Schofield, D. M. Kass, A. Kleinböhl, N. G. Heavens and D. J. McCleese, "Carbon dioxide snow clouds on Mars: South polar winter observations by the Mars Climate Sounder", Journal of Geophysical Research (Planets) **117**, E08014 (2012).

Hecht, M. H., "The texture of condensed CO_2 on the martian polar caps", Planetary and Space Science **56**, 246–250 (2008).

Herschel, W., "On the Remarkable Appearances at the Polar Regions of the Planet Mars, the Inclination of Its Axis, the Position of Its Poles, and Its Spheroidical Figure; With a Few Hints Relating to Its Real Diameter and Atmosphere. By William Herschel, Esq. F. R. S.", Philosophical Transactions of the Royal Society of London Series I **74**, 233–273 (1784).

Hogenboom, D. L., J. S. Kargel, G. J. Consolmagno, T. C. Holden, L. Lee and M. Buyyounouski, "The ammonia-water system and the chemical differentiation of icy satellites", Icarus **128**, 171–180 (1997).

Holler, B. J., L. A. Young, M. W. Buie, W. M. Grundy, J. E. Lyke, E. F. Young and H. G. Roe, "Measuring temperature and ammonia hydrate ice on charon in 2015 from keck/osiris spectra", Icarus **284**, 394–406 (2017).

Holmes, M. J., N. G. Parker and M. J. W. Povey, "Temperature dependence of bulk viscosity in water using acoustic spectroscopy", in "Journal of Physics Conference Series", vol. 269 of *Journal of Physics Conference Series*, p. 012011 (2011).

Huber, M. L., R. A. Perkins, D. G. Friend, J. V. Sengers, M. J. Assael, I. N. Metaxa, K. Miyagawa, R. Hellmann and E. Vogel, "New International Formulation for the Thermal Conductivity of H_2O", Journal of Physical and Chemical Reference Data **41**, 3, 033102–033102 (2012).

James, P. B., B. A. Cantor and S. Davis, "Mars Orbiter Camera observations of the Martian south polar cap in 1999-2000", Journal of Geophysical Research **106**, 23635–23652 (2001).

James, P. B., B. A. Cantor, M. C. Malin, K. Edgett, M. H. Carr, G. E. Danielson, A. P. Ingersoll, M. E. Davies, W. K. Hartmann, A. S. McEwen, L. A. Soderblom, P. C. Thomas and J. Veverka, "The 1997 Spring Regression of the Martian South Polar Cap: Mars Orbiter Camera Observations", Icarus **144**, 410–418 (2000).

James, P. B., H. H. Kieffer and D. A. Paige, *The seasonal cycle of carbon dioxide on Mars*, pp. 934–968 (1992).

Jenniskens, P., D. F. Blake and A. Kouchi, "Amorphous Water Ice. a Solar System Material", in "Solar System Ices", edited by B. Schmitt, C. de Bergh and M. Festou, vol. 227 of *Astrophysics and Space Science Library*, p. 139 (1998).

Jewitt, D. C. and J. Luu, "Crystalline water ice on the kuiper belt object (50000) quaoar", Nature **432**, 7018, 731–733 (2004).

Kargel, J., S. Croft, J. Lunine and J. Lewis, "Rheological properties of ammonia-water liquids and crystal-liquid slurries: Planetological applications", Icarus **89**, 1, 93 – 112 (1991).

Kargel, J. S., "Cryovolcanism on the icy satellites", Earth Moon and Planets **67**, 101–113 (1994).

Kelly, N. J., W. V. Boynton, K. Kerry, D. Hamara, D. Janes, R. C. Reedy, K. J. Kim and R. M. Haberle, "Seasonal polar carbon dioxide frost on Mars: CO_2 mass and columnar thickness distribution", Journal of Geophysical Research (Planets) **111**, E03S07 (2006).

Kieffer, H. H., "Cold jets in the Martian polar caps", Journal of Geophysical Research (Planets) **112**, E08005 (2007).

Kieffer, H. H., "Thermal model for analysis of Mars infrared mapping", Journal of Geophysical Research (Planets) **118**, 451–470 (2013).

Kieffer, H. H., P. R. Christensen and T. N. Titus, "CO_2 jets formed by sublimation beneath translucent slab ice in Mars' seasonal south polar ice cap", Nature **442**, 793–796 (2006).

Kieffer, H. H. and T. N. Titus, "TES Mapping of Mars' North Seasonal Cap", Icarus **154**, 162–180 (2001).

Kieffer, H. H., T. N. Titus, K. F. Mullins and P. R. Christensen, "Mars south polar spring and summer behavior observed by TES: Seasonal cap evolution controlled by frost grain size", Joiurnal of Geophysical Research **105**, 9653–9700 (2000).

Kossacki, K. J. and W. J. Markiewicz, "Martian Seasonal CO_2 Ice in Polygonal Troughs in Southern Polar Region: Role of the Distribution of Subsurface H_2O Ice", Icarus **160**, 73–85 (2002).

Langevin, Y., J.-P. Bibring, F. Montmessin, F. Forget, M. Vincendon, S. Douté, F. Poulet and B. Gondet, "Observations of the south seasonal cap of Mars during recession in 2004-2006 by the OMEGA visible/near-infrared imaging spectrometer on board Mars Express", Journal of Geophysical Research (Planets) **112**, E08S12 (2007).

Leighton, R. B. and B. C. Murray, "Behavior of Carbon Dioxide and Other Volatiles on Mars", Science **153**, 136–144 (1966).

Leto, G. and G. A. Baratta, "Ly-alpha photon induced amorphization of Ic water ice at 16 Kelvin. Effects and quantitative comparison with ion irradiation", Astronomy and Astrophysics **397**, 7–13 (2003).

Litvak, M. L., I. G. Mitrofanov, A. S. Kozyrev, A. B. Sanin, V. I. Tretyakov, W. V. Boynton, N. J. Kelly, D. Hamara and R. S. Saunders, "Long-term observations

of southern winters on Mars: Estimations of column thickness, mass, and volume density of the seasonal CO_2 deposit from HEND/Odyssey data", Journal of Geophysical Research (Planets) **112**, E03S13 (2007).

Litvak, M. L., I. G. Mitrofanov, A. S. Kozyrev, A. B. Sanin, V. I. Tret'yakov, W. V. Boynton, C. Shinohara, D. Hamara, S. Saunders and D. M. Drake, "Seasonal Carbon Dioxide Depositions on the Martian Surface as Revealed from Neutron Measurements by the HEND Instrument Onboard the 2001 Mars Odyssey Spacecraft", Solar System Research **38**, 167–177 (2004).

Lopes, R. M. C., K. L. Mitchell, E. R. Stofan, J. I. Lunine, R. Lorenz, F. Paganelli, R. L. Kirk, C. A. Wood, S. D. Wall, L. E. Robshaw, A. D. Fortes, C. D. Neish, J. Radebaugh, E. Reffet, S. J. Ostro, C. Elachi, M. D. Allison, Y. Anderson, R. Boehmer, G. Boubin, P. Callahan, P. Encrenaz, E. Flamini, G. Francescetti, Y. Gim, G. Hamilton, S. Hensley, M. A. Janssen, W. T. K. Johnson, K. Kelleher, D. O. Muhleman, G. Ori, R. Orosei, G. Picardi, F. Posa, L. E. Roth, R. Seu, S. Shaffer, L. A. Soderblom, B. Stiles, S. Vetrella, R. D. West, L. Wye and H. A. Zebker, "Cryovolcanic features on titan's surface as revealed by the cassini titan radar mapper", Icarus **186**, 395–412 (2007).

Lunine, J. I. and D. J. Stevenson, "Thermodynamics of clathrate hydrate at low and high pressures with application to the outer solar system", Astrophys. J. Supp. Series **58**, 493–531 (1985).

Manga, M. and C.-Y. Wang, "Pressurized oceans and the eruption of liquid water on europa and enceladus", Geophysical Research Letters **34**, 7, l07202 (2007).

Mastrapa, R. M. and R. H. Brown, "Ion irradiation of crystalline h2o–ice: Effect on the 1.65-μm band", Icarus **183**, 1, 207 – 214 (2006).

Mccleese, D. J., J. T. Schofield, F. W. Taylor, S. B. Calcutt, M. C. Foote, D. M. Kass, C. B. Leovy, D. A. Paige, P. L. Read and R. W. Zurek, "Mars climate sounder: An investigation of thermal and water vapor structure, dust and condensate distributions in the atmosphere, and energy balance of the polar regions", Journal of Geophysical Research: Planets **112**, E5, n/a–n/a (2007).

McEwen, A. S., E. M. Eliason, J. W. Bergstrom, N. T. Bridges, C. J. Hansen, W. A. Delamere, J. A. Grant, V. C. Gulick, K. E. Herkenhoff, L. Keszthelyi, R. L. Kirk, M. T. Mellon, S. W. Squyres, N. Thomas and C. M. Weitz, "Mars Reconnaissance Orbiter's High Resolution Imaging Science Experiment (HiRISE)", Journal of Geophysical Research (Planets) **112**, E05S02 (2007).

McKinnon, W. B., D. Prialnik, S. A. Stern and A. Coradini, *Structure and Evolution of Kuiper Belt Objects and Dwarf Planets*, pp. 213–241 (2008).

Mckinnon, W. B., S. A. Stern, H. A. Weaver, F. Nimmo, C. J. Bierson, W. M. Grundy, J. C. Cook, D. P. Cruikshank, A. H. Parker, J. M. Moore, J. R. Spencer, L. A. Young, C. B. Olkin and K. Ennico Smith, "Origin of the pluto☐charon system: Constraints from the new horizons flyby", Icarus **287**, C, 2–11 (2017).

Moore, J. M., W. B. McKinnon, J. R. Spencer, A. D. Howard, P. M. Schenk, R. A. Beyer, F. Nimmo, K. N. Singer, O. M. Umurhan, O. L. White, S. A. Stern, K. Ennico, C. B. Olkin, H. A. Weaver, L. A. Young, R. P. Binzel, M. W. Buie, B. J. Buratti, A. F. Cheng, D. P. Cruikshank, W. M. Grundy, I. R. Linscott, H. J. Reitsema, D. C. Reuter, M. R. Showalter, V. J. Bray, C. L. Chavez, C. J. A. Howett, T. R. Lauer, C. M. Lisse, A. H. Parker, S. B. Porter, S. J. Robbins, K. Runyon, T. Stryk, H. B. Throop, C. C. C. Tsang, A. J. Verbiscer, A. M. Zangari, A. L. Chaikin, D. E. Wilhelms, F. Bagenal, G. R. Gladstone, T. Andert, J. Andrews, M. Banks, B. Bauer, J. Bauman, O. S. Barnouin, P. Bedini, K. Beisser, S. Bhaskaran, E. Birath, M. Bird, D. J. Bogan, A. Bowman, M. Brozovic, C. Bryan, M. R. Buckley, S. S. Bushman, A. Calloway, B. Carcich, S. Conard, C. A. Conrad, J. C. Cook, O. S. Custodio, C. M. D. Ore, C. Deboy, Z. J. B. Dischner, P. Dumont, A. M. Earle, H. A. Elliott, J. Ercol, C. M. Ernst, T. Finley, S. H. Flanigan, G. Fountain, M. J. Freeze, T. Greathouse, J. L. Green, Y. Guo, M. Hahn, D. P. Hamilton, S. A. Hamilton, J. Hanley, A. Harch, H. M. Hart, C. B. Hersman, A. Hill, M. E. Hill, D. P. Hinson, M. E. Holdridge, M. Horanyi, C. Jackman, R. A. Jacobson, D. E. Jennings, J. A. Kammer, H. K. Kang, D. E. Kaufmann, P. Kollmann, S. M. Krimigis, D. Kusnierkiewicz, J. E. Lee, K. L. Lindstrom, A. W. Lunsford, V. A. Mallder, N. Martin, D. J. McComas, R. L. McNutt, D. Mehoke, T. Mehoke, E. D. Melin, M. Mutchler, D. Nelson, J. I. Nunez, A. Ocampo, W. M. Owen, M. Paetzold, B. Page, J. W. Parker, F. Pelletier, J. Peterson, N. Pinkine, M. Piquette, S. Protopapa, J. Redfern, J. H. Roberts, G. Rogers, D. Rose, K. D. Retherford, M. G. Ryschkewitsch, E. Schindhelm, B. Sepan, M. Soluri, D. Stanbridge, A. J. Steffl, D. F. Strobel, M. E. Summers, J. R. Szalay, M. Tapley, A. Taylor, H. Taylor, G. L. Tyler, M. H. Versteeg, M. Vincent, R. Webbert, S. Weidner, G. E. Weigle, K. Whittenburg, B. G. Williams, K. Williams, S. Williams, W. W. Woods and E. Zirnstein, "The geology of Pluto and Charon through the eyes of New Horizons", Science **351**, 1284–1293 (2016).

Mount, C. P. and T. N. Titus, "Evolution of Mars' northern polar seasonal CO_2 deposits: Variations in surface brightness and bulk density", Journal of Geophysical Research (Planets) **120**, 1252–1266 (2015).

Murnaghan, F. D., "The Compressibility of Media under Extreme Pressures", Proceedings of the National Academy of Science **30**, 244–247 (1944).

Neugebauer, G., G. Münch, H. Kieffer, S. C. Chase, Jr. and E. Miner, "Mariner 1969 Infrared Radiometer Results: Temperatures and Thermal Properties of the Martian Surface", Astronomical Journal **76**, 719 (1971).

Neveu, M., S. J. Desch, E. L. Shock and C. R. Glein, "Prerequisites for explosive cryovolcanism on dwarf planet-class kuiper belt objects", Icarus **246**, 48–64 (2015).

Paige, D. A. and A. P. Ingersoll, "Annual heat balance of Martian polar caps - Viking observations", Science **228**, 1160–1168 (1985).

Piqueux, S. and P. R. Christensen, "North and south subice gas flow and venting of the seasonal caps of Mars: A major geomorphological agent", Journal of Geophysical Research (Planets) **113**, E06005 (2008).

Piqueux, S., A. Kleinböhl, P. O. Hayne, N. G. Heavens, D. M. Kass, D. J. McCleese, J. T. Schofield and J. H. Shirley, "Discovery of a widespread low-latitude diurnal CO_2 frost cycle on Mars", Journal of Geophysical Research (Planets) **121**, 1174–1189 (2016).

Piqueux, S., A. Kleinböhl, P. O. Hayne, D. M. Kass, J. T. Schofield and D. J. McCleese, "Variability of the martian seasonal CO_2 cap extent over eight Mars Years", Icarus **251**, 164–180 (2015).

Pollack, J. B., R. M. Haberle, J. R. Murphy, J. Schaeffer and H. Lee, "Simulations of the general circulation of the Martian atmosphere. II - Seasonal pressure variations", Journal of Geophysical Research **98**, 3149–3181 (1993).

Pollack, J. B., R. M. Haberle, J. Schaeffer and H. Lee, "Simulations of the general circulation of the Martian atmosphere. I - Polar processes", Journal of Geophysical Research **95**, 1447–1473 (1990).

Pommerol, A., G. Portyankina, N. Thomas, K.-M. Aye, C. J. Hansen, M. Vincendon and Y. Langevin, "Evolution of south seasonal cap during Martian spring: Insights from high-resolution observations by HiRISE and CRISM on Mars Reconnaissance Orbiter", Journal of Geophysical Research (Planets) **116**, E08007 (2011).

Porter, S. B., S. J. Desch and J. C. Cook, "Micrometeorite impact annealing of ice in the outer Solar System", Icarus **208**, 492–498 (2010).

Portyankina, G., W. J. Markiewicz, N. Thomas, C. J. Hansen and M. Milazzo, "HiRISE observations of gas sublimation-driven activity in Mars' southern polar regions: III. Models of processes involving translucent ice", Icarus **205** (2010).

Portyankina, G., A. Pommerol, K.-M. Aye, C. J. Hansen and N. Thomas, "Polygonal cracks in the seasonal semi-translucent CO_2 ice layer in Martian polar areas", Journal of Geophysical Research (Planets) **117**, E02006 (2012).

Prettyman, T. H., W. C. Feldman, M. T. Mellon, G. W. McKinney, W. V. Boynton, S. Karunatillake, D. J. Lawrence, S. Maurice, A. E. Metzger, J. R. Murphy, S. W. Squyres, R. D. Starr and R. L. Tokar, "Composition and structure of the Martian surface at high southern latitudes from neutron spectroscopy", Journal of Geophysical Research (Planets) **109**, E05001 (2004).

Prettyman, T. H., W. C. Feldman and T. N. Titus, "Characterization of Mars' seasonal caps using neutron spectroscopy", Journal of Geophysical Research (Planets) **114**, E08005 (2009).

Putzig, N. E. and M. T. Mellon, "Apparent thermal inertia and the surface heterogeneity of Mars", Icarus **191**, 68–94 (2007).

Raack, J., D. Reiss, T. Appéré, M. Vincendon, O. Ruesch and H. Hiesinger, "Present-day seasonal gully activity in a south polar pit (Sisyphi Cavi) on Mars", Icarus **251**, 226–243 (2015).

Reuter, D., S. Stern, J. Scherrer, D. Jennings, J. Baer, J. Hanley, L. Hardaway, A. Lunsford, S. McMuldroch, J. Moore, C. Olkin, R. Parizek, H. Reitsma, D. Sabatke, J. Spencer, J. Stone, H. Throop, J. Cleve, G. Weigle and L. Young, "Ralph: A visible/infrared imager for the new horizons pluto/kuiper belt mission", Space Science Reviews **140**, 1, 129–154 (2008).

Ruiz, J., "Heat flow and depth to a possible internal ocean on Triton", Icarus **166**, 436–439 (2003).

Shulman, L. M., "The heat capacity of water ice in interstellar or interplanetary conditions", Astronomy and Astrophysics **416**, 187–190 (2004).

Smith, D. E., M. T. Zuber, H. V. Frey, J. B. Garvin, J. W. Head, D. O. Muhleman, G. H. Pettengill, R. J. Phillips, S. C. Solomon, H. J. Zwally, W. B. Banerdt, T. C. Duxbury, M. P. Golombek, F. G. Lemoine, G. A. Neumann, D. D. Rowlands, O. Aharonson, P. G. Ford, A. B. Ivanov, C. L. Johnson, P. J. McGovern, J. B. Abshire, R. S. Afzal and X. Sun, "Mars Orbiter Laser Altimeter: Experiment summary after the first year of global mapping of Mars", Journal of Geophysical Research **106**, 23689–23722 (2001a).

Smith, D. E., M. T. Zuber and G. A. Neumann, "Seasonal Variations of Snow Depth on Mars", Science **294**, 2141–2146 (2001b).

Stern, S. A., F. Bagenal, K. Ennico, G. R. Gladstone, W. M. Grundy, W. B. McKinnon, J. M. Moore, C. B. Olkin, J. R. Spencer, H. A. Weaver, L. A. Young, T. Andert, J. Andrews, M. Banks, B. Bauer, J. Bauman, O. S. Barnouin, P. Bedini, K. Beisser, R. A. Beyer, S. Bhaskaran, R. P. Binzel, E. Birath, M. Bird, D. J. Bogan, A. Bowman, V. J. Bray, M. Brozovic, C. Bryan, M. R. Buckley, M. W. Buie, B. J. Buratti,

S. S. Bushman, A. Calloway, B. Carcich, A. F. Cheng, S. Conard, C. A. Conrad, J. C. Cook, D. P. Cruikshank, O. S. Custodio, C. M. Dalle Ore, C. Deboy, Z. J. B. Dischner, P. Dumont, A. M. Earle, H. A. Elliott, J. Ercol, C. M. Ernst, T. Finley, S. H. Flanigan, G. Fountain, M. J. Freeze, T. Greathouse, J. L. Green, Y. Guo, M. Hahn, D. P. Hamilton, S. A. Hamilton, J. Hanley, A. Harch, H. M. Hart, C. B. Hersman, A. Hill, M. E. Hill, D. P. Hinson, M. E. Holdridge, M. Horanyi, A. D. Howard, C. J. A. Howett, C. Jackman, R. A. Jacobson, D. E. Jennings, J. A. Kammer, H. K. Kang, D. E. Kaufmann, P. Kollmann, S. M. Krimigis, D. Kusnierkiewicz, T. R. Lauer, J. E. Lee, K. L. Lindstrom, I. R. Linscott, C. M. Lisse, A. W. Lunsford, V. A. Mallder, N. Martin, D. J. McComas, R. L. McNutt, D. Mehoke, T. Mehoke, E. D. Melin, M. Mutchler, D. Nelson, F. Nimmo, J. I. Nunez, A. Ocampo, W. M. Owen, M. Paetzold, B. Page, A. H. Parker, J. W. Parker, F. Pelletier, J. Peterson, N. Pinkine, M. Piquette, S. B. Porter, S. Protopapa, J. Redfern, H. J. Reitsema, D. C. Reuter, J. H. Roberts, S. J. Robbins, G. Rogers, D. Rose, K. Runyon, K. D. Retherford, M. G. Ryschkewitsch, P. Schenk, E. Schindhelm, B. Sepan, M. R. Showalter, K. N. Singer, M. Soluri, D. Stanbridge, A. J. Steffl, D. F. Strobel, T. Stryk, M. E. Summers, J. R. Szalay, M. Tapley, A. Taylor, H. Taylor, H. B. Throop, C. C. C. Tsang, G. L. Tyler, O. M. Umurhan, A. J. Verbiscer, M. H. Versteeg, M. Vincent, R. Webbert, S. Weidner, G. E. Weigle, O. L. White, K. Whittenburg, B. G. Williams, K. Williams, S. Williams, W. W. Woods, A. M. Zangari and E. Zirnstein, "The Pluto system: Initial results from its exploration by New Horizons", Science **350**, aad1815 (2015).

Stevenson, D. J., "Volcanism and igneous processes in small icy satellites", Nature **298**, 142–144 (1982).

Strazzulla, G. and M. E. Palumbo, "Evolution of icy surfaces: an experimental approach", Planetary and Space Science **46**, 1339–1348 (1998).

Thomas, N., C. J. Hansen, G. Portyankina and P. S. Russell, "HiRISE observations of gas sublimation-driven activity in Mars' southern polar regions: II. Surficial deposits and their origins", Icarus **205**, 296–310 (2010).

Tillman, J. E., N. C. Johnson, P. Guttorp and D. B. Percival, "The Martian annual atmospheric pressure cycle - Years without great dust storms", Journal of Geophysical Research **98**, 10 (1993).

Titus, T. N., H. H. Kieffer, K. F. Mullins and P. R. Christensen, "TES premapping data: Slab ice and snow flurries in the Martian north polar night", Journal of Geophysical Research **106**, 23181–23196 (2001).

Tullis, T. E., F. G. Horowitz and J. Tullis, "Flow laws of polyphase aggregates from end-member flow laws", Journal of Geophysical Research **96**, 8081–8096 (1991).

Varlashkin, P. G. and J. C. Thompson, "Thermal conductivity of liquid ammonia", Journal of Chemical & Engineering Data **8**, 4, 526–526 (1963).

Vincendon, M., Y. Langevin, F. Poulet, J.-P. Bibring and B. Gondet, "Recovery of surface reflectance spectra and evaluation of the optical depth of aerosols in the near-IR using a Monte Carlo approach: Application to the OMEGA observations of high-latitude regions of Mars", Journal of Geophysical Research (Planets) **112**, E08S13 (2007).

Wagstaff, K. L., T. N. Titus, A. B. Ivanov, R. Castaño and J. L. Bandfield, "Observations of the north polar water ice annulus on Mars using THEMIS and TES", Planetary and Space Science **56**, 256–265 (2008).

Warren, S. G., W. J. Wiscombe and J. F. Firestone, "Spectral albedo and emissivity of CO2 in Martian polar caps - Model results", Journal of Geophysical Research **95**, 14717–14741 (1990).

APPENDIX A

DERIVATION OF GOVERNING EQUATIONS FOR CRYOPIPE

Nomenclature

α Arbitrary Scalar

$\hat{n}$ Unit Normal Vector

λ Bulk Viscosity

$\dot{\underline{\varepsilon}}$ Rate of Strain Tensor

$\underline{\underline{\sigma_x}}$ Stress Tensor of Phase x

$\underline{\underline{\tau}}$ Stress Tensor

$\underline{\underline{B}}$ Arbitrary Tensor

$\underline{\underline{I}}$ Identity Matrix

μ Dynamic (Shear) Viscosity

ρ Density

a   Arbitrary Vector

F   Force Vector

g   Gravity Vector

h   Displacement Vector

p   Momentum Vector

q   Heat Flux Vector

S   Stress Vector

v   Velocity Vector

A Surface Area

C Pre-exponent Strain Rate Coefficient

E Internal Energy

e Mass Specific Internal Energy

G Activation Energy

K Kinetic Energy

k	Thermal Conductivity
n	Power Law Strain Rate Dependence
P	Pressure
Q	Heat
R	Universal Gas Constant
T	Temperature
t	Time
U	Potential Energy
V	Volume
W	Work

A.1 Conservation of Mass

The continuity equation defines the change over time of any intensive property of a material in a time variable volume. For mass (extensive), this is the density (intensive)

$$\frac{\mathrm{d}}{\mathrm{d}t} \int_{V(t)} \rho \, \mathrm{d}V = 0 \tag{A.1}$$

Leibniz's rule defines how the time derivative operates on a fluid volume

$$\frac{\mathrm{d}}{\mathrm{d}t} \int_{V(t)} \alpha \, \mathrm{d}V = \int_{V(t)} \left[\frac{\partial \alpha}{\partial t} + \boldsymbol{\nabla} \cdot (\alpha \mathbf{v}) \right] \mathrm{d}V \tag{A.2}$$

substitute this into the previous equation

$$\int_{V(t)} \left[\frac{\partial \rho}{\partial t} + \boldsymbol{\nabla} \cdot (\rho \mathbf{v}) \right] \mathrm{d}V = 0 \tag{A.3}$$

Stokes' Theorem states that for the volume integral of an integrand to be zero over an arbitrary volume, the integrand, itself, must be zero. Therefore,

$$\frac{\partial \rho}{\partial t} + \boldsymbol{\nabla} \cdot (\rho \mathbf{v}) = 0 \tag{A.4}$$

The equation of state for the density in my model is computed from empirical equations for the 4 components arithmetically averaged by mass fraction. These empirical equations are functions of temperature and pressure,

$$\rho = \rho(T, P) \tag{A.5}$$

Therefore, we can rewrite the derivative as

$$\frac{\partial \rho}{\partial t} = \left. \frac{\partial \rho}{\partial P} \right)_T \frac{\partial P}{\partial t} + \left. \frac{\partial \rho}{\partial T} \right)_P \frac{\partial T}{\partial t} \tag{A.6}$$

Substituting this into equation (A.4), rearranging, and expanding, yields

$$\left. \frac{\partial \rho}{\partial P} \right)_T \frac{\partial P}{\partial t} + \left. \frac{\partial \rho}{\partial T} \right)_P \frac{\partial T}{\partial t} = -\mathbf{v} \cdot \boldsymbol{\nabla} \rho - \rho \boldsymbol{\nabla} \cdot \mathbf{v} \tag{A.7}$$

The identity for the LHS of the equation can be utilized for the density gradient on the RHS as well, giving

$$\boldsymbol{\nabla} \rho = \left. \frac{\partial \rho}{\partial P} \right)_T \boldsymbol{\nabla} P + \left. \frac{\partial \rho}{\partial T} \right)_P \boldsymbol{\nabla} T \tag{A.8}$$

By substituting this into equation (A.7) we arrive at

$$\left. \frac{\partial \rho}{\partial P} \right)_T \frac{\partial P}{\partial t} + \left. \frac{\partial \rho}{\partial T} \right)_P \frac{\partial T}{\partial t} = - \left. \frac{\partial \rho}{\partial P} \right)_T \mathbf{v} \cdot \boldsymbol{\nabla} P - \left. \frac{\partial \rho}{\partial T} \right)_P \mathbf{v} \cdot \boldsymbol{\nabla} T - \rho \boldsymbol{\nabla} \cdot \mathbf{v} \tag{A.9}$$

I rearrange this equation by moving the temperature derivative term to the RHS of the equation and dividing through by the density-pressure derivative

$$\frac{\partial P}{\partial t} = -\mathbf{v} \cdot \boldsymbol{\nabla} P - \left. \frac{\partial \rho}{\partial P} \right)_T^{-1} \left[\left. \frac{\partial \rho}{\partial T} \right)_P \left(\frac{\partial T}{\partial t} + \mathbf{v} \cdot \boldsymbol{\nabla} T \right) + \rho \boldsymbol{\nabla} \cdot \mathbf{v} \right] \tag{A.10}$$

The material derivative is defined as

$$\frac{\mathrm{D}\alpha}{\mathrm{D}t} \equiv \frac{\partial \alpha}{\partial t} + \mathbf{v} \cdot \boldsymbol{\nabla} \alpha$$

$$\frac{\mathrm{D}\mathbf{a}}{\mathrm{D}t} \equiv \frac{\partial \mathbf{a}}{\partial t} + \mathbf{v} \cdot \boldsymbol{\nabla} \mathbf{a} \tag{A.11}$$

Substitute this into equation (A.10) to simplify to

$$\frac{\partial P}{\partial t} = -\mathbf{v} \cdot \boldsymbol{\nabla} P - \left. \frac{\partial \rho}{\partial P} \right)_T^{-1} \left[\left. \frac{\partial \rho}{\partial T} \right)_P \frac{\mathrm{D}T}{\mathrm{D}t} + \rho \boldsymbol{\nabla} \cdot \mathbf{v} \right] \tag{A.12}$$

where $\frac{\partial \rho}{\partial P}_T$ and $\frac{\partial \rho}{\partial T}_P$ are computed from empirical density equations of state for each component (taken from Croft *et al.* (1988), Feistel and Wagner (2006), and Fortes *et al.* (2003)), weighted by mass fraction. This pressure equation, which is the used to track the change in Pressure over time, is a representation of the conservation of mass. The forward computed pressure is then used to compute the density at the next timestep, when compressibility is allowed. Note that the material derivative of the temperature is for the *fluid advection* between cells, NOT the general temperature gradient for the calculation of conduction of cells within thermal contact. The temperature field, its spatial derivatives, and its temporal derivative is found from back calculation of the energy conservation equation (see §A.3).

There are 3 boundary conditions at the top of the conduit that are of concern for the pressure: a Neumann condition for the velocity, and a Direchlet condition for the Pressure, and a Neumann condition for the advected fluid temperature (but not the conductive temperature).

This is

$$\left. \frac{\partial v}{\partial z} \right|_{surf} = 0$$

$$P_{surf} = 0 \tag{A.13}$$

$$\left. \frac{\partial T}{\partial z} \right|_{surf} = 0$$

respectively. For these to be true, all else being equal, the pressure gradient must be constant at the surface.

$$\left. \frac{\partial P}{\partial z} \right|_{surf} = \left. \frac{\partial P}{\partial z} \right|_{surf-\Delta z} = constant \tag{A.14}$$

However, the pressure equation is

$$\frac{\partial P}{\partial t} = -v\frac{\partial P}{\partial z} - \left(\frac{\partial \rho}{\partial P}\right)_T^{-1} \left[\left(\frac{\partial \rho}{\partial T}\right)_P \frac{\mathrm{D}T}{\mathrm{D}t} - \rho\frac{\partial v}{\partial z}\right] \tag{A.15}$$

At the surface this is

$$\left. \frac{\partial P}{\partial t} \right|_{surf} = -v_{surf-\Delta z} \left. \frac{\partial P}{\partial z} \right|_{surf-\Delta z} - \left(\frac{\partial \rho}{\partial P}\right)_{T,surf}^{-1} \left(\frac{\partial \rho}{\partial T}\right)_{P,surf} \left. \frac{\partial T}{\partial t} \right|_{surf-\Delta z} \tag{A.16}$$

Under steady-state energy, the temperature derivative vanishes.

$$\left. \frac{\partial P}{\partial t} \right|_{surf} = -v_{surf-\Delta z} \left. \frac{\partial P}{\partial z} \right|_{surf-\Delta z} \tag{A.17}$$

139

Therefore, the only way to satisfy a constant surface pressure over time of 0 is to force the velocity to 0 or to make the pressure gradient 0. We've already established, though, that the velocity at the surface is equal to the velocity in the first cell under the surface by way of the Neumann condition on velocity, which generally is non-zero. If the velocity is non-zero then there must be a pressure gradient. Therefore the only way to stop the pressure from increasing indefinitely and satisfy the surface boundary condition is to add an additional term to correct the pressure over time. This can be thought of as a '"source term"'.

$$\frac{\partial P}{\partial t} = -v\frac{\partial P}{\partial z} - S_P)_e \tag{A.18}$$

For the surface boundary the change in pressure over time must be 0, this is

$$S_P)_e = -v_{surf}\frac{\partial P}{\partial z}\bigg|_{surf} \tag{A.19}$$

The same argument can be made for a zero-velocity case. The pressure derivative term disappears leaving only the pressure change due to temperature.

$$\frac{\partial P}{\partial t}\bigg|_{surf} = -\frac{\partial \rho}{\partial P}\bigg)_{T,surf}^{-1}\frac{\partial \rho}{\partial T}\bigg)_{P,surf}\frac{\partial T}{\partial t}\bigg|_{surf-\Delta z} \tag{A.20}$$

The change in temperature must then be 0 for the pressure over time to be 0, which is generally not the case. Therefore I must modify the pressure by another '"source term"'.

$$\frac{\partial P}{\partial t} = -\frac{\partial \rho}{\partial P}\bigg)_{T}^{-1}\frac{\partial \rho}{\partial T}\bigg)_{P}\frac{\partial T}{\partial t} - S_P)_{v=0} \tag{A.21}$$

Setting the pressure over time to zero as required at the surface allows for the solution of the zero velocity source term

$$S_P)_{v=0} = -\frac{\partial \rho}{\partial P}\bigg)_{T}^{-1}\frac{\partial \rho}{\partial T}\bigg)_{P}\frac{\partial T}{\partial t} \tag{A.22}$$

Therefore the general pressure equation must be

$$\frac{\partial P}{\partial t} = -v\frac{\partial P}{\partial z} - \frac{\partial \rho}{\partial P}\bigg)_{T}^{-1}\left[\frac{\partial \rho}{\partial T}\bigg)_{P}\frac{\mathrm{D}T}{\mathrm{D}t} + \rho\frac{\partial v}{\partial z}\right] - [S_P)_e + S_P)_{v=0}] \tag{A.23}$$

substitute from above

$$\begin{aligned}\frac{\partial P}{\partial t} = &-v\frac{\partial P}{\partial z} - \frac{\partial \rho}{\partial P}\bigg)_{T}^{-1}\left[\frac{\partial \rho}{\partial T}\bigg)_{P}\frac{\mathrm{D}T}{\mathrm{D}t} + \rho\frac{\partial v}{\partial z}\right]\\ &+ v_{surf-\Delta z}\frac{\partial P}{\partial z}\bigg|_{surf-\Delta z}\\ &+ \frac{\partial \rho}{\partial P}\bigg)_{T,surf}^{-1}\frac{\partial \rho}{\partial T}\bigg)_{P,surf}\frac{\partial T}{\partial t}\bigg|_{surf-\Delta z}\end{aligned} \tag{A.24}$$

A.2 Conservation of Momentum

Newton's second law relates the change in momentum with the sum of the forces

$$\frac{\mathrm{d}\mathbf{p}}{\mathrm{d}t} = \sum_i \mathbf{F}_i \tag{A.25}$$

For a fluid volume this is

$$\frac{\mathrm{d}}{\mathrm{d}t} \int_{V(t)} \rho\mathbf{v}\,\mathrm{d}V = \sum_i \mathbf{F}_i \tag{A.26}$$

Leibniz's rule dictates

$$\int_{V(t)} \left\{ \frac{\partial}{\partial t}(\rho\mathbf{v}) + \boldsymbol{\nabla} \cdot [(\rho\mathbf{v})\mathbf{v}] \right\} \mathrm{d}V = \sum_i \mathbf{F}_i \tag{A.27}$$

Expand using the product rule,

$$\int_{V(t)} \left\{ \rho\frac{\partial \mathbf{v}}{\partial t} + \mathbf{v}\frac{\partial \rho}{\partial t} + \mathbf{v}\boldsymbol{\nabla} \cdot (\rho\mathbf{v}) + (\rho\mathbf{v}) \cdot \boldsymbol{\nabla}\mathbf{v} \right\} \mathrm{d}V = \sum_i \mathbf{F}_i \tag{A.28}$$

rearrange,

$$\int_{V(t)} \left\{ \rho\frac{\partial \mathbf{v}}{\partial t} + \rho(\mathbf{v} \cdot \boldsymbol{\nabla})\mathbf{v} + \mathbf{v}\frac{\partial \rho}{\partial t} + \mathbf{v}\boldsymbol{\nabla} \cdot (\rho\mathbf{v}) \right\} \mathrm{d}V = \sum_i \mathbf{F}_i \tag{A.29}$$

factor,

$$\int_{V(t)} \left\{ \rho\left[\frac{\partial \mathbf{v}}{\partial t} + (\mathbf{v} \cdot \boldsymbol{\nabla})\mathbf{v} \right] + \mathbf{v}\left[\frac{\partial \rho}{\partial t} + \boldsymbol{\nabla} \cdot (\rho\mathbf{v}) \right] \right\} \mathrm{d}V = \sum_i \mathbf{F}_i \tag{A.30}$$

substitute equation (A.3) in for second term on LHS,

$$\int_{V(t)} \left\{ \rho\left[\frac{\partial \mathbf{v}}{\partial t} + (\mathbf{v} \cdot \boldsymbol{\nabla})\mathbf{v} \right] \right\} \mathrm{d}V = \sum_i \mathbf{F}_i \tag{A.31}$$

and substitute in equation (A.11)

$$\int_{V(t)} \rho\frac{\mathrm{D}\mathbf{v}}{\mathrm{D}t}\,\mathrm{d}V = \sum_i \mathbf{F}_i \tag{A.32}$$

141

The sum of the forces is equal to the body forces plus surface forces, in this case, gravity and stress, respectively

$$\sum_i \mathbf{F}_i = \int_{V(t)} \rho \mathbf{g} \, dV + \oint_{A(t)} \mathbf{S} \, dA \tag{A.33}$$

$\mathbf{S}$ is the Stress vector, defined as

$$\mathbf{S} \equiv \hat{n} \cdot \underline{\underline{\tau}} \tag{A.34}$$

Substituting this into the sum of the forces returns

$$\sum_i \mathbf{F}_i = \int_{V(t)} \rho \mathbf{g} \, dV + \oint_{A(t)} \hat{n} \cdot \underline{\underline{\tau}} \, dA \tag{A.35}$$

The Divergence Theorem relates surface integrals to volume integrals.

$$\oint_{A(t)} \mathbf{a} \cdot \hat{n} \, dA = \int_{V(t)} \boldsymbol{\nabla} \cdot \mathbf{a} \, dV$$

$$\oint_{A(t)} \hat{n} \cdot \underline{\underline{B}} \, dA = \int_{V(t)} \boldsymbol{\nabla} \cdot \underline{\underline{B}} \, dV \tag{A.36}$$

Substitute equation (A.36) in

$$\sum_i \mathbf{F}_i = \int_{V(t)} \rho \mathbf{g} \, dV + \int_{V(t)} \boldsymbol{\nabla} \cdot \underline{\underline{\tau}} \, dV \tag{A.37}$$

$$\int_{V(t)} \rho \frac{D\mathbf{v}}{Dt} \, dV = \int_{V(t)} \rho \mathbf{g} \, dV + \int_{V(t)} \boldsymbol{\nabla} \cdot \underline{\underline{\tau}} \, dV \tag{A.38}$$

Utilizing Stokes' theorem (arbitrary volumes) again, I find

$$\rho \frac{D\mathbf{v}}{Dt} = \rho \mathbf{g} + \boldsymbol{\nabla} \cdot \underline{\underline{\tau}} \tag{A.39}$$

Divide through by the density and separate the material derivative and I produce the equation implemented in the model

$$\frac{\partial \mathbf{v}}{\partial t} = -\mathbf{v} \cdot \boldsymbol{\nabla} \mathbf{v} + \mathbf{g} + \frac{1}{\rho} \boldsymbol{\nabla} \cdot \underline{\underline{\tau}} \tag{A.40}$$

This is the conservation of momentum equation employed by the model and is used to compute the change in velocity over time. The stress tensor $\underline{\underline{\tau}}$ is covered in §A.4

A.3 Conservation of Energy

The total energy is

$$E + K = -Q + W + U \tag{A.41}$$

The time derivative of this equation is simply

$$\frac{\mathrm{d}E}{\mathrm{d}t} + \frac{\mathrm{d}K}{\mathrm{d}t} = -\delta Q + \frac{\mathrm{d}W}{\mathrm{d}t} + \frac{\mathrm{d}U}{\mathrm{d}t} \tag{A.42}$$

for a fluid volume these derivatives must be integrated over time variable fluid volumes

$$\frac{\mathrm{d}}{\mathrm{d}t} \int_{V(t)} \rho e \, \mathrm{d}V + \frac{\mathrm{d}}{\mathrm{d}t} \int_{V(t)} \frac{1}{2}\rho v^2 \, \mathrm{d}V = -\oint_{A(t)} \mathbf{q} \cdot \hat{n} \, \mathrm{d}A$$

$$+ \oint_{A(t)} \mathbf{S} \cdot \mathbf{v} \, \mathrm{d}A \tag{A.43}$$

$$+ \frac{\mathrm{d}}{\mathrm{d}t} \int_{V(t)} \rho \mathbf{g} \cdot \mathbf{h} \, \mathrm{d}V$$

Rearranged, this is

$$\frac{\mathrm{d}}{\mathrm{d}t} \int_{V(t)} \left[\rho \left(e + \frac{1}{2}v^2 \right) \right] \mathrm{d}V = -\oint_{A(t)} \mathbf{q} \cdot \hat{n} \, \mathrm{d}A$$

$$+ \oint_{A(t)} \mathbf{S} \cdot \mathbf{v} \, \mathrm{d}A \tag{A.44}$$

$$+ \frac{\mathrm{d}}{\mathrm{d}t} \int_{V(t)} \rho \mathbf{g} \cdot \mathbf{h} \, \mathrm{d}V$$

Let

$$\epsilon = e + \frac{1}{2}v^2 \tag{A.45}$$

and substitute equations (A.34) and (A.45) into equation (A.44)

$$\frac{\mathrm{d}}{\mathrm{d}t} \int_{V(t)} \rho \epsilon \, \mathrm{d}V = -\oint_{A(t)} \mathbf{q} \cdot \hat{n} \, \mathrm{d}A + \oint_{A(t)} \hat{n} \cdot \underline{\underline{\tau}} \cdot \mathbf{v} \, \mathrm{d}A + \frac{\mathrm{d}}{\mathrm{d}t} \int_{V(t)} \rho \mathbf{g} \cdot \mathbf{h} \, \mathrm{d}V \tag{A.46}$$

Leibniz's rule gives

$$\int\limits_{V(t)} \left[\frac{\partial}{\partial t}(\rho\epsilon) + \boldsymbol{\nabla} \cdot (\rho\epsilon\mathbf{v}) \right] \mathrm{d}V = - \oint\limits_{A(t)} \mathbf{q} \cdot \hat{n}\, \mathrm{d}A + \oint\limits_{A(t)} \hat{n} \cdot \underline{\underline{\tau}} \cdot \mathbf{v}\, \mathrm{d}A$$
$$+ \int\limits_{V(t)} \left\{ \frac{\partial}{\partial t}(\rho\mathbf{g} \cdot \mathbf{h}) + \boldsymbol{\nabla} \cdot [(\rho\mathbf{g} \cdot \mathbf{h})\mathbf{v}] \right\} \mathrm{d}V \tag{A.47}$$

Expand and simplify the integrand on the RHS using the Chain rule,

$$\frac{\partial}{\partial t}(\rho\epsilon) + \boldsymbol{\nabla} \cdot (\rho\epsilon\mathbf{v}) = \rho\frac{\partial\epsilon}{\partial t} + \epsilon\frac{\partial\rho}{\partial t} + \epsilon\boldsymbol{\nabla} \cdot (\rho\mathbf{v}) + \rho\mathbf{v} \cdot \boldsymbol{\nabla}\epsilon \tag{A.48}$$

rearrange, and factor

$$\frac{\partial}{\partial t}(\rho\epsilon) + \boldsymbol{\nabla} \cdot (\rho\epsilon\mathbf{v}) = \rho\left[\frac{\partial\epsilon}{\partial t} + (\mathbf{v} \cdot \boldsymbol{\nabla})\epsilon \right] + \epsilon\left[\frac{\partial\rho}{\partial t} + \boldsymbol{\nabla} \cdot (\rho\mathbf{v}) \right] \tag{A.49}$$

The first term on RHS is the material derivative (equation (A.11)) and second term on RHS is zero (equation (A.3))

$$\frac{\partial}{\partial t}(\rho\epsilon) + \boldsymbol{\nabla} \cdot (\rho\epsilon\mathbf{v}) = \rho\frac{\mathrm{D}\epsilon}{\mathrm{D}t} \tag{A.50}$$

Expand and simplify the volume integrand in the third term on the RHS of equation (A.47) by chain rule,

$$\frac{\partial}{\partial t}(\rho\mathbf{g} \cdot \mathbf{h}) + \boldsymbol{\nabla} \cdot [(\rho\mathbf{g} \cdot \mathbf{h})\mathbf{v}] = \rho\frac{\partial}{\partial t}(\mathbf{g} \cdot \mathbf{h}) + (\mathbf{g} \cdot \mathbf{h})\frac{\partial\rho}{\partial t}$$
$$+ \rho\mathbf{v} \cdot \boldsymbol{\nabla}(\mathbf{g} \cdot \mathbf{h}) + (\mathbf{g} \cdot \mathbf{h})\boldsymbol{\nabla} \cdot (\rho\mathbf{v}) \tag{A.51}$$

rearrange, and factor

$$\frac{\partial}{\partial t}(\rho\mathbf{g} \cdot \mathbf{h}) + \boldsymbol{\nabla} \cdot [(\rho\mathbf{g} \cdot \mathbf{h})\mathbf{v}] = \rho\left[\frac{\partial}{\partial t}(\mathbf{g} \cdot \mathbf{h}) + (\mathbf{v} \cdot \boldsymbol{\nabla})(\mathbf{g} \cdot \mathbf{h}) \right]$$
$$+ (\mathbf{g} \cdot \mathbf{h})\left[\frac{\partial\rho}{\partial t} + \boldsymbol{\nabla} \cdot (\rho\mathbf{v}) \right] \tag{A.52}$$

Again, the first term on RHS is the material derivative (equation (A.11)) and second term on RHS is zero (equation (A.3))

$$\frac{\partial}{\partial t}(\rho\mathbf{g} \cdot \mathbf{h}) + \boldsymbol{\nabla} \cdot [(\rho\mathbf{g} \cdot \mathbf{h})\mathbf{v}] = \rho\frac{\mathrm{D}}{\mathrm{D}t}(\mathbf{g} \cdot \mathbf{h}) \tag{A.53}$$

Assuming gravity is constant, I can factor it out of the RHS

$$\frac{\partial}{\partial t}(\rho\mathbf{g} \cdot \mathbf{h}) + \boldsymbol{\nabla} \cdot [(\rho\mathbf{g} \cdot \mathbf{h})\mathbf{v}] = \rho\mathbf{g} \cdot \frac{\mathrm{D}\mathbf{h}}{\mathrm{D}t} \tag{A.54}$$

144

The material derivative of displacement is simply the velocity, so

$$\frac{\partial}{\partial t}(\rho \mathbf{g} \cdot \mathbf{h}) + \boldsymbol{\nabla} \cdot [(\rho \mathbf{g} \cdot \mathbf{h})\mathbf{v}] = \rho \mathbf{g} \cdot \mathbf{v} \tag{A.55}$$

I now substitute equations (A.50) and (A.55) into equation (A.47)

$$\int_{V(t)} \rho \frac{\mathrm{D}\epsilon}{\mathrm{D}t} \, \mathrm{d}V = - \oint_{A(t)} \mathbf{q} \cdot \hat{n} \, \mathrm{d}A + \oint_{A(t)} \hat{n} \cdot \underline{\underline{\tau}} \cdot \mathbf{v} \, \mathrm{d}A + \int_{V(t)} \rho \mathbf{g} \cdot \mathbf{v} \, \mathrm{d}V \tag{A.56}$$

I use the divergence theorem to convert the surface integrals to volume integrals

$$\int_{V(t)} \rho \frac{\mathrm{D}\epsilon}{\mathrm{D}t} \, \mathrm{d}V = - \int_{V(t)} \boldsymbol{\nabla} \cdot \mathbf{q} \, \mathrm{d}V + \int_{V(t)} \boldsymbol{\nabla} \cdot \left(\underline{\underline{\tau}} \cdot \mathbf{v}\right) \mathrm{d}V + \int_{V(t)} \rho \mathbf{g} \cdot \mathbf{v} \, \mathrm{d}V \tag{A.57}$$

and Stokes' theorem to simplify the equation to

$$\rho \frac{\mathrm{D}\epsilon}{\mathrm{D}t} = -\boldsymbol{\nabla} \cdot \mathbf{q} + \boldsymbol{\nabla} \cdot \left(\underline{\underline{\tau}} \cdot \mathbf{v}\right) + \rho \mathbf{g} \cdot \mathbf{v} \tag{A.58}$$

The Tensor chain rule is

$$\begin{aligned}
\boldsymbol{\nabla} \cdot \left(\alpha \underline{\underline{B}}\right) &= \alpha \boldsymbol{\nabla} \cdot \underline{\underline{B}} + \boldsymbol{\nabla}\alpha \cdot \underline{\underline{B}} \\
\boldsymbol{\nabla} \cdot \left(\underline{\underline{B}} \cdot \mathbf{a}\right) &= \left(\boldsymbol{\nabla} \cdot \underline{\underline{B}}\right) \cdot \mathbf{a} + \underline{\underline{B}} \cdot \cdot (\boldsymbol{\nabla} \otimes \mathbf{a})^{\mathrm{T}}
\end{aligned} \tag{A.59}$$

When equation (A.59) is applied to equation (A.58), I get the equation for total energy conservation.

$$\rho \frac{\mathrm{D}\epsilon}{\mathrm{D}t} = -\boldsymbol{\nabla} \cdot \mathbf{q} + \left(\boldsymbol{\nabla} \cdot \underline{\underline{\tau}}\right) \cdot \mathbf{v} + \underline{\underline{\tau}} \cdot \cdot (\boldsymbol{\nabla} \otimes \mathbf{v})^{\mathrm{T}} + \rho \mathbf{g} \cdot \mathbf{v} \tag{A.60}$$

A.3.1 Mechanical Energy

Let mechanical energy be equation (A.39) dotted into the velocity

$$\rho \frac{\mathrm{D}\mathbf{v}}{\mathrm{D}t} \cdot \mathbf{v} = \rho \mathbf{g} \cdot \mathbf{v} + \left(\boldsymbol{\nabla} \cdot \underline{\underline{\tau}}\right) \cdot \mathbf{v} \tag{A.61}$$

and

$$v^2 \equiv \mathbf{v} \cdot \mathbf{v} \tag{A.62}$$

By chain rule

$$\frac{\mathrm{D}v^2}{\mathrm{D}t} = \frac{\mathrm{D}}{\mathrm{D}t}(\mathbf{v} \cdot \mathbf{v}) = \mathbf{v} \cdot \frac{\mathrm{D}\mathbf{v}}{\mathrm{D}t} + \mathbf{v} \cdot \frac{\mathrm{D}\mathbf{v}}{\mathrm{D}t} = 2\mathbf{v} \cdot \frac{\mathrm{D}\mathbf{v}}{\mathrm{D}t} \tag{A.63}$$

Therefore

$$\frac{D\mathbf{v}}{Dt} \cdot \mathbf{v} = \frac{1}{2}\frac{Dv^2}{Dt} \tag{A.64}$$

Substitute equation (A.64) into equation (A.61) to arrive at the equation for mechanical energy conservation.

$$\rho\frac{1}{2}\frac{Dv^2}{Dt} = \rho\mathbf{g} \cdot \mathbf{v} + \left(\boldsymbol{\nabla} \cdot \underline{\underline{\tau}}\right) \cdot \mathbf{v} \tag{A.65}$$

A.3.2 Thermal Energy

Subtract equation (A.65) from equation (A.60)

$$\begin{aligned}\rho\frac{D\epsilon}{Dt} - \rho\frac{1}{2}\frac{Dv^2}{Dt} = &-\boldsymbol{\nabla} \cdot \mathbf{q} + \left(\boldsymbol{\nabla} \cdot \underline{\underline{\tau}}\right) \cdot \mathbf{v} + \underline{\underline{\tau}} \boldsymbol{:}(\boldsymbol{\nabla} \otimes \mathbf{v})^{\mathrm{T}} + \rho\mathbf{g} \cdot \mathbf{v} \\ &- \rho\mathbf{g} \cdot \mathbf{v} - \left(\boldsymbol{\nabla} \cdot \underline{\underline{\tau}}\right) \cdot \mathbf{v}\end{aligned} \tag{A.66}$$

I simplify this by eliminating like-terms.

$$\rho\left[\frac{D\epsilon}{Dt} - \frac{1}{2}\frac{Dv^2}{Dt}\right] = -\boldsymbol{\nabla} \cdot \mathbf{q} + \underline{\underline{\tau}} \boldsymbol{:}(\boldsymbol{\nabla} \otimes \mathbf{v})^{\mathrm{T}} \tag{A.67}$$

Recall equation (A.45) and substitute into equation (A.67)

$$\rho\left[\frac{D}{Dt}\left(e + \frac{1}{2}v^2\right) - \frac{1}{2}\frac{Dv^2}{Dt}\right] = -\boldsymbol{\nabla} \cdot \mathbf{q} + \underline{\underline{\tau}} \boldsymbol{:}(\boldsymbol{\nabla} \otimes \mathbf{v})^{\mathrm{T}} \tag{A.68}$$

distribute

$$\rho\left[\frac{De}{Dt} + \frac{1}{2}\frac{Dv^2}{Dt} - \frac{1}{2}\frac{Dv^2}{Dt}\right] = -\boldsymbol{\nabla} \cdot \mathbf{q} + \underline{\underline{\tau}} \boldsymbol{:}(\boldsymbol{\nabla} \otimes \mathbf{v})^{\mathrm{T}} \tag{A.69}$$

I have finally arrived at the equation for thermal energy

$$\rho\frac{De}{Dt} = -\boldsymbol{\nabla} \cdot \mathbf{q} + \underline{\underline{\tau}} \boldsymbol{:}(\boldsymbol{\nabla} \otimes \mathbf{v})^{\mathrm{T}} \tag{A.70}$$

Expand the material derivative on the LHS and move the spatial derivative over to get

$$\frac{\partial e}{\partial t} = -\mathbf{v} \cdot \boldsymbol{\nabla}e - \frac{1}{\rho}\left[\boldsymbol{\nabla} \cdot \mathbf{q} - \underline{\underline{\tau}} \boldsymbol{:}(\boldsymbol{\nabla} \otimes \mathbf{v})^{\mathrm{T}}\right] \tag{A.71}$$

This is the energy conservation equation implemented in the model. This computes the change in internal energy of each cell over time. The heat flux vector, $\mathbf{q}$, and the stress tensor, $\underline{\underline{\tau}}$, are discussed in §A.4.

A.4   Constitutive Equations

There are two constitutive equations I need to fully characterize the conservation equations, one for the stress tensor and another for the heat flux vector.

A.4.1   The Stress Tensor

Generally, a single constitutive law is adopted to describe the stress imparted onto a fluid. However, our fluid contains both liquid and solid components, of which, the solids are non-newtonian. I propose an end-member approach to computing the stress tensor, where the liquid components are newtonian and the solid components follow a power law. This is defined by

$$\underline{\underline{\tau}} = \underline{\underline{\sigma}}_l^{g_l} \cdot \underline{\underline{\sigma}}_s^{g_s} - P\underline{\underline{I}} \tag{A.72}$$

where the subscripts l and s denote the liquid and solid phases, respectively. The stress tensor for the liquid phases is defined as newtonian and has the form

$$\underline{\underline{\sigma}}_l = \lambda(\boldsymbol{\nabla} \cdot \mathbf{v})\underline{\underline{I}} + 2\mu\underline{\dot{\underline{\varepsilon}}} \tag{A.73}$$

and the solid components follow the method used by Durham *et al.* (1993) and Tullis *et al.* (1991) to describe a mutli-end-member polyphase aggregate, which is

$$\underline{\underline{\sigma}}_s = C^{-\frac{1}{n}}\underline{\dot{\underline{\varepsilon}}}^{\frac{1}{n}}e^{\frac{G}{nRT}} \tag{A.74}$$

The rate of strain tensor, $\underline{\dot{\underline{\varepsilon}}}$, is defined as

$$\underline{\dot{\underline{\varepsilon}}} = \frac{1}{2}\Big[(\boldsymbol{\nabla} \otimes \mathbf{v}) + (\boldsymbol{\nabla} \otimes \mathbf{v})^{\mathrm{T}}\Big] \tag{A.75}$$

and C, n, and G are computed directly via the method of Tullis *et al.* (1991) with materials parameters from Durham *et al.* (1993). It should be noted that the root of a tensor generally does not have a unique solution. Also, the rate of strain and stress tensors can be negative, which can result in complex values when computing the power law. Because of these, I do not attempt to evaluate the root tensor, rather compute the root of each individual value within the tensor and take the only the real component. This preserves the sign (direction) of the stress and is consistent with the methodology of Tullis *et al.* (1991), Durham *et al.* (1993), and Kargel *et al.* (1991).

A.4.2   Stress Tensor Validation

To test the validity of this methodology, I computed the effective viscosity of the multiphase fluid under steady state conditions and compare that to the slurry viscosity estimated by Kargel *et al.* (1991) from a modified Einstein-Roscoe formulation

147

fit to laboratory measured viscosity values. A limitation to this equation is that it becomes complex after an asymptote at a solids crystal fraction of ≈ 0.27. There, it reaches a maximum, and the real values *decrease* as the solids crystal fraction increases. This is inconsistent with the rheology of the solid components, so is unreliable at high solids crystal fractions. My model requires that crystal fractions reach up to 1.0, so I compute the effective solid dynamic viscosity from the stress tensor by using the maximum stress therein.

$$\mu_{s,eff} = \frac{\sigma_{s,max}}{\dot{\varepsilon}_{max}} \tag{A.76}$$

$$\mu_{s,eff} = C^{-1}\sigma_{s,max}^{1-n}e^{\frac{G}{RT}} \tag{A.77}$$

The effective solid viscosity is then geometrically averaged by mole fraction with the liquid dynamic viscosity as detailed by Kargel *et al.* (1991).

$$\mu_{eff} = \mu^{h_l}\mu_{s,eff}^{h_s} \tag{A.78}$$

This is done by setting the initial solids crystal fraction to a value, the initial velocity to the Poiseuille profile at the true liquid viscosity, then using equation (A.40) to iterate on the velocity, while updating the stress tensor, until it reaches a steady state ($\frac{\partial v}{\partial t} = 0$). If the model for the stress tensor is accurate, the effective viscosity and the slurry viscosity should be comparable up to ≈ 0.27.

Figures A.4.2 and A.4.2 illustrate the viscosities and corresponding velocities at 180K as a function of crystal content. The solids are assumed to be $H_2O_{(s)}$ and use the power law stress tensor in the absence of $ADH_{(s)}$. The effective viscosity is typically higher than the empirical slurry viscosity at low crystal contents by a factor of 1.5 - 2.5. However, as noted above, the slurry viscosity increases rapidly as it approaches the asymptote at approximately 0.27 crystal mass fraction, whereas the effective viscosty remains continuous. It does not reach slurry viscosity values until a crystal content of approximately 0.40. Thus, the stress tensor model employed here likely underestimates the velocity of the flow while crystal contents are low. At crystal contents around the asymptote, my stress tensor will likely overestimate the velocities. Despite this, the error is likely of little concern because the velocities are very near zero. At high crystal contents, the stress tensor more accurately models the solids than the viscosity model given by Kargel *et al.* (1991).
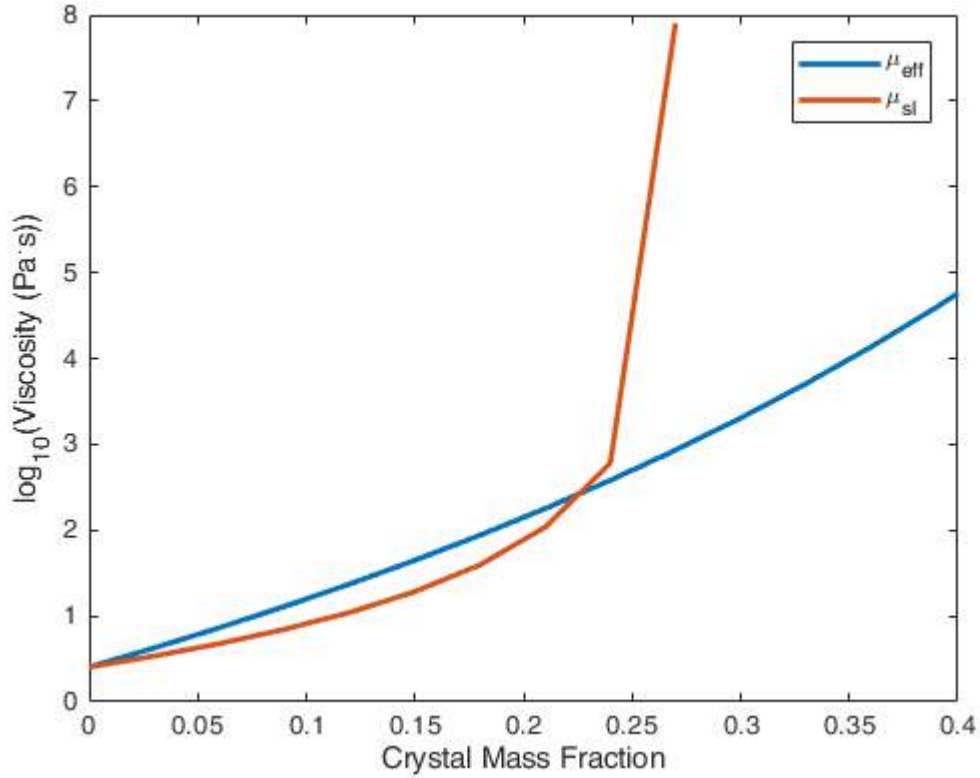
Figure 50. Effective and slurry viscosity as a function of crystal content at 180 K

Values are computed after spin-up of the velocity field from an initial Pouiseuille profile at the viscosity of the liquid until the flow field converges on a steady state at the effective viscosity. The effective viscosity differs from the slurry viscosity by a factor of up to ≈2.5 before a crystal content of ≈0.25, after which the viscosities diverge.

A.4.3 The Heat Flux Vector

The primary method of heat transfer within the fluid is assumed to be conduction, due both to the density and pressure state of the fluid. Therefore, Fourier's Law is chosen as the constitutive equation for heat flux. This is

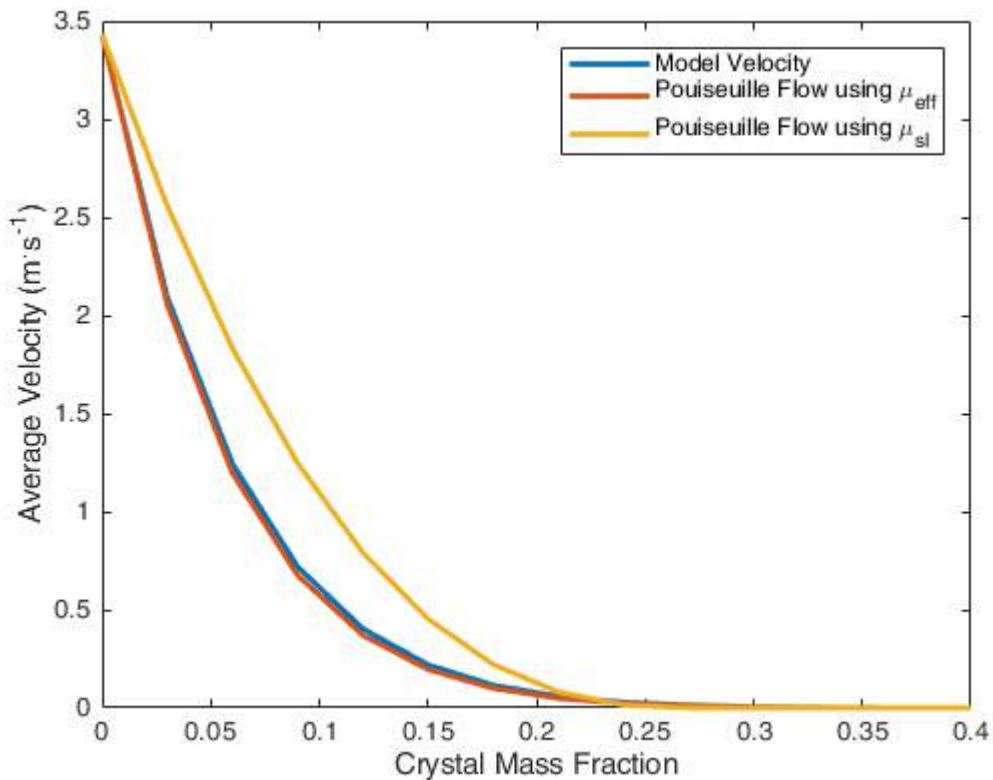$$\mathbf{q} = -k\boldsymbol{\nabla}T \tag{A.79}$$

Figure 51. Model velocity and Analytically computed velocities as a function of crystal content

I have a high degree of confidence that the values are being computed as intended because the Poiseuille velocity computed with effective viscosity is nearly identical to the spin-up velocity of the flow. On average, the slurry velocity is a factor of ≈2 higher than the effective viscosity, however the velocities are essentially zero at high crystal fraction. Therefore, the drastic difference in viscosity at these values should be inconsiquential.

In my model, the thermal conductivity, k is NOT constant, varying over space as a function of temperature. Thus, by chain rule the divergence of the heat flux vector is

$$\boldsymbol{\nabla} \cdot \mathbf{q} = \boldsymbol{\nabla} \cdot (-k\boldsymbol{\nabla}T) = -k\boldsymbol{\nabla} \cdot \boldsymbol{\nabla}T - \boldsymbol{\nabla}k \cdot \boldsymbol{\nabla}T \tag{A.80}$$

which can be simplified to

$$\boldsymbol{\nabla} \cdot \mathbf{q} = -k\nabla^2 T - \boldsymbol{\nabla}k \cdot \boldsymbol{\nabla}T \tag{A.81}$$

In two-dimensional, cylindrical coordinates,

$$k\nabla^2 T = k\left(\frac{\partial^2 T}{\partial z^2} + \frac{\partial^2 T}{\partial r^2} + \frac{1}{r}\frac{\partial T}{\partial r}\right) \tag{A.82}$$

$$\boldsymbol{\nabla}k \cdot \boldsymbol{\nabla}T = \frac{\partial k}{\partial z}\frac{\partial T}{\partial z} + \frac{\partial k}{\partial r}\frac{\partial T}{\partial r} \tag{A.83}$$

$$\boldsymbol{\nabla} \cdot \mathbf{q} = -k\left(\frac{\partial^2 T}{\partial z^2} + \frac{\partial^2 T}{\partial r^2} + \frac{1}{r}\frac{\partial T}{\partial r}\right) - \frac{\partial k}{\partial z}\frac{\partial T}{\partial z} - \frac{\partial k}{\partial r}\frac{\partial T}{\partial r} \tag{A.84}$$

In the special case of the last vertical cell in the conduit, the fluid is allowed to radiate to space. To model this, an additional term is added to the divergence

$$\boldsymbol{\nabla} \cdot \mathbf{q}|_{surf} = \boldsymbol{\nabla} \cdot \mathbf{q} + \frac{1}{\Delta z}\sigma_B T^4 \tag{A.85}$$

Thereby providing additional cooling to the top-most cells in the conduit.

A.5   Finite Differences

Finite differencing is a common technique in numerical modeling, especially in computational fluid dynamics. This technique is derived from the Taylor series approximation. There are three approaches, forward, backward, and center-point. I will cover them here. The first derivative using forward-point finite differencing is

$$f(\alpha + \Delta\alpha) \approx f(\alpha) + \frac{\Delta\alpha}{1!}\frac{\partial f}{\partial \alpha}\bigg|_\alpha \tag{A.86}$$

where α can be either r or z. The first derivative for backward-point finite differencing is

$$f(\alpha - \Delta\alpha) \approx f(\alpha) + \frac{-\Delta\alpha}{1!}\frac{\partial f}{\partial \alpha}\bigg|_\alpha \tag{A.87}$$

. Center-point finite differencing is calculated by differencing the forward and backward approximations

$$f(\alpha + \Delta\alpha) - f(\alpha - \Delta\alpha) \approx 2\Delta\alpha\frac{\partial f}{\partial \alpha}\bigg|_\alpha \tag{A.88}$$

solve for the derivative term

$$\frac{\partial f}{\partial \alpha}\bigg|_\alpha \approx \frac{f(\alpha + \Delta\alpha) - f(\alpha - \Delta\alpha)}{2\Delta\alpha} \tag{A.89}$$

This form is the most accurate and is used in this model. All derivatives in the model equations can be substituted with the center-point finite difference shown here.

The second derivative is found in a similar fashion

$$f(\alpha + \Delta\alpha) \approx f(\alpha) + \frac{\Delta\alpha}{1!}\frac{\partial f}{\partial \alpha}\bigg|_\alpha + \frac{(\Delta\alpha)^2}{2!}\frac{\partial^2 f}{\partial \alpha^2}\bigg|_\alpha \tag{A.90}$$

$$f(\alpha - \Delta\alpha) \approx f(\alpha) + \frac{-\Delta\alpha}{1!}\frac{\partial f}{\partial \alpha}\bigg|_\alpha + \frac{(-\Delta\alpha)^2}{2!}\frac{\partial^2 f}{\partial \alpha^2}\bigg|_\alpha \tag{A.91}$$

now I add the forward and backward approximations, arriving at

$$f(\alpha + \Delta\alpha) + f(\alpha - \Delta\alpha) \approx 2f(\alpha) + 2\frac{(\Delta\alpha)^2}{2}\frac{\partial^2 f}{\partial \alpha^2}\bigg|_\alpha \tag{A.92}$$

solve for the second derivative

$$\frac{\partial^2 f}{\partial \alpha^2}\bigg|_\alpha \approx \frac{f(\alpha + \Delta\alpha) - 2f(\alpha) + f(\alpha - \Delta\alpha)}{(\Delta\alpha^2)} \tag{A.93}$$

A.5.1 Boundaries

The boundaries of the conduit require special cases of the finite difference approximations to satisfy the boundary conditions. This is because variables are calculated at the center of each cell, but the boundaries occur on the edge of cells. This means that the last forward finite difference component and the first backward finite difference component of the center finite difference uses only $\frac{1}{2}\Delta\alpha$ grid spacing (as opposed to $\Delta\alpha$ at non-boundary cells), depending on the boundary. I will derive the special cases for each type of boundary type generally.

To reduce the error term associated with the Taylor series approximation, the first derivative is solved for using the Taylor series expansion to the second order. This was done because I found that the error on the Taylor series approximation to the first order for the first derivative was insufficient to accurately estimate Pouiselle flow when the fluid was in a steady state and in thermal equilibrium. As such, the forward finite difference for the upper radial and vertical boundaries is

$$
\begin{aligned}
f\left(\alpha + \frac{1}{2}\Delta\alpha\right) &\approx f(\alpha) + \frac{\frac{1}{2}\Delta\alpha}{1!}\left.\frac{\partial f}{\partial\alpha}\right|_\alpha + \frac{\left(\frac{1}{2}\Delta\alpha\right)^2}{2!}\left.\frac{\partial^2 f}{\partial\alpha^2}\right|_\alpha \\
&\approx f(\alpha) + \frac{\Delta\alpha}{2}\left.\frac{\partial f}{\partial\alpha}\right|_\alpha + \frac{(\Delta\alpha)^2}{8}\left.\frac{\partial^2 f}{\partial\alpha^2}\right|_\alpha
\end{aligned}
\tag{A.94}
$$

The backward difference is the same as equation (A.91). The center-point finite difference is then found by multiplying equation (A.91) by $-\frac{1}{4}$ and summing it with equation (A.94) to force the second order term to vanish. This yields

$$
f\left(\alpha + \frac{1}{2}\Delta\alpha\right) - \frac{1}{4}f(\alpha - \Delta\alpha) \approx \frac{3}{4}f(\alpha) + \frac{3}{4}\Delta\alpha\left.\frac{\partial f}{\partial\alpha}\right|_\alpha
\tag{A.95}
$$

solve this for the first derivative to arrive at

$$
\left.\frac{\partial f}{\partial\alpha}\right|_\alpha \approx \frac{4f\left(\alpha + \frac{1}{2}\Delta\alpha\right) - 3f(\alpha) - f(\alpha - \Delta\alpha)}{3\Delta\alpha}
\tag{A.96}
$$

The second derivative is found similarly. Using the same equations as the first derivative, but multiply equation (A.91) by $\frac{1}{2}$ and add it to equation (A.94), such that the first derivative in the approximation vanishes.

$$f\left(\alpha + \frac{1}{2}\Delta\alpha\right) + \frac{1}{2}f(\alpha - \Delta\alpha) \approx \frac{3}{2}f(\alpha) + \frac{3}{8}(\Delta\alpha)^2 \frac{\partial^2 f}{\partial\alpha^2}\bigg|_\alpha \tag{A.97}$$

solve for the second derivative to get

$$\frac{\partial^2 f}{\partial\alpha^2}\bigg|_\alpha \approx \frac{8f\left(\alpha + \frac{1}{2}\Delta\alpha\right) - 12f(\alpha) + 4f(\alpha - \Delta\alpha)}{3(\Delta\alpha)^2} \tag{A.98}$$

The lower vertical boundary is calculated similarly, but the boundary occurs on the backward difference

$$\begin{aligned} f\left(\alpha - \frac{1}{2}\Delta\alpha\right) &\approx f(\alpha) + \frac{-\frac{1}{2}\Delta\alpha}{1!}\frac{\partial f}{\partial\alpha}\bigg|_\alpha + \frac{\left(-\frac{1}{2}\Delta\alpha\right)^2}{2!}\frac{\partial^2 f}{\partial\alpha^2}\bigg|_\alpha \\ &\approx f(\alpha) - \frac{\Delta\alpha}{2}\frac{\partial f}{\partial\alpha}\bigg|_\alpha + \frac{(\Delta\alpha)^2}{8}\frac{\partial^2 f}{\partial\alpha^2}\bigg|_\alpha \end{aligned} \tag{A.99}$$

I can then manipulate equation (A.90) to solve for the first and second derivative in the same manner as the upper boundaries.

$$\frac{\partial f}{\partial\alpha}\bigg|_\alpha \approx \frac{f(\alpha + \Delta\alpha) + 3f(\alpha) - 4f(\alpha - \Delta\alpha)}{3\Delta\alpha} \tag{A.100}$$

$$\frac{\partial^2 f}{\partial\alpha^2}\bigg|_\alpha \approx \frac{4f(\alpha + \Delta\alpha) - 12f(\alpha) + 8f\left(\alpha - \frac{1}{2}\Delta\alpha\right)}{3(\Delta\alpha)^2} \tag{A.101}$$

The inner radial boundary is computed using symmetry arguments. As such, this boundary is not computed at the edge of the inner radial cell, but rather at the center of the *negative* radial cells. Due to the symmetry of the conduit about the vertical axis, any negative radial cell is equal to its positive counterpart. Therefore, the finite difference is merely the backward finite difference at the inner radial boundary.

Table 3. Boundary values for selected variables

These are used for estimating finite differences in the advecting fluid and are substituted into the finite difference equations above for the respective boundary. Dashes indicate that no derivatives of that variable are taken with respect to the boundary within the model.

| Variable | Boundary | | | |
	$z = 0$	$z = -L$	$r = R$	$r = -\frac{1}{2}\Delta r$
v	$v_{z-\frac{1}{2}\Delta z}$	$v_{z+\frac{1}{2}\Delta z}$	0	$v_{\frac{1}{2}\Delta r}$
P	P_{surf}	P_{base}	-	-
T	$T_{z-\frac{1}{2}\Delta z}$	T_{base}	-	-
e	$e_{z-\frac{1}{2}\Delta z}$	e_{base}	-	-
τ	τ_z	τ_z	$\tau_{r-\frac{1}{2}\Delta r}$	$\tau_{\frac{1}{2}\Delta r}$